

Final Report

Smart Power Turbine

Final Technical Report

Reporting Period Start Date 07/12/01

Reporting Period End Date 09/30/03

Submitted for General Electric by:

Nirm V. Nirmalan*

GE Global Research Center

Building K1, Room ES108

1Research Circle

Niskayuna. NY 12309

Phone: 518-387-5610

FAX: 518-387-7592

E-mail: nirmalan@crd.ge.co,

***Contributing authors listed in Acknowledgments**

Date Report was issued: November 2003

Name and address of submitting organization:

GE Global Research Center

Building K1, Room ES108

1Research Circle

Niskayuna. NY 12309

Sandia National Laboratories

1515 Eubank Boulevard S.E.

Albuquerque, NM 78123

DOE Cooperative Agreement No. DE-FC26-01NT41021

Final Report

This report was prepared as an account of work sponsored by an agency of the United States Government. Neither the United States Government nor any agency thereof, nor any of their employees, makes any warranty, express or implied, or assumes any legal liability or responsibility for the accuracy, completeness, or usefulness of any information, apparatus, product, or process disclosed, or represents that its use would not infringe privately owned rights. Reference herein to any specific commercial product, process, or service by trade name, trademark, manufacturer, or otherwise does not necessarily constitute or imply its endorsement, recommendation, or favoring by the United States Government or any agency thereof. The views and opinions of authors expressed herein do not necessarily state or reflect those of the United States Government or any agency thereof

Final Report

ABSTRACT

Gas turbines are the choice technology for high-performance power generation and are employed in both simple and combined cycle configurations around the world. The Smart Power Turbine (SPT) program has developed new technologies that are needed to further extend the performance and economic attractiveness of gas turbines for power generation. Today's power generation gas turbines control firing temperatures indirectly, by measuring the exhaust gas temperature and then mathematically calculating the peak combustor temperatures. But temperatures in the turbine hot gas path vary a great deal, making it difficult to control firing temperatures precisely enough to achieve optimal performance. Similarly, there is no current way to assess deterioration of turbine hot-gas-path components without shutting down the turbine. Consequently, maintenance and component replacements are often scheduled according to conservative design practices based on historical fleet-averaged data. Since fuel heating values vary with the prevalent natural gas fuel, the inability to measure heating value directly, with sufficient accuracy and timeliness, can lead to maintenance and operational decisions that are less than optimal. GE Global Research Center, under this Smart Power Turbine program, has developed a suite of novel sensors that would measure combustor flame temperature, online fuel lower heating value (LHV), and hot-gas-path component life directly.

The feasibility of using the ratio of the integrated intensities of portions of the OH emission band to determine the specific average temperature of a premixed methane or natural-gas-fueled combustion flame was demonstrated. The temperature determined is the temperature of the plasma included in the field of view of the sensor. Two sensor types were investigated: the first used a low-resolution fiber optic spectrometer; the second was a SiC dual photodiode chip. Both methods worked. Sensitivity to flame temperature changes was remarkably high, that is a 1-2.5% change in ratio for an 11.1°C (20°F) change in temperature at flame temperatures between 1482.2°C (2700°F) and 1760°C (3200°F). Sensor ratio calibration was performed using flame temperatures determined by calculations using the amount of unburned oxygen in the exhaust and by the fuel/air ratio of the combustible gas mixture. The agreement between the results of these two methods was excellent. The sensor methods characterized are simple and viable. Experiments are underway to validate the GE Flame Temperature Sensor as a practical tool for use with multiburner gas turbine combustors.

The lower heating value (LHV) Fuel Quality Sensor consists of a catalytic film deposited on the surface of a microhotplate. This micromachined design has low heat capacity and thermal conductivity, making it ideal for heating catalysts placed on its surface. Several methods of catalyst deposition were investigated, including micropen deposition and other proprietary methods, which permit precise and repeatable placement of the materials. The use of catalysts on the LHV sensor expands the limits of flammability (LoF) of combustion fuels as compared with conventional flames; an unoptimized LoF of 1-32% for natural gas (NG) in air was demonstrated with the microcombustor, whereas conventionally 4 to 16% is observed. The primary goal of this work was to measure the LHV of NG fuels. The secondary goal was to determine the relative quantities of the various components of NG mixes. This determination was made successfully by using an array of different catalysts operating at different temperatures. The combustion parameters for methane were shown to be dependent on whether Pt or Pd catalysts were used. In this project, significant effort was expended on making the LHV platform more robust by the addition of high-temperature stable materials, such as tantalum, and the use of passivation overcoats to protect the resistive heater/sensor materials from degradation in the combustion environment. Modeling and simulation were used to predict improved sensor designs.

Final Report

The Coating Life Odometer task demonstrated the technical feasibility of a “smart” thermal barrier coating (TBC) that indicates its service condition during turbine operation. The smart TBC was based on a state-of-the-art 8 wt% yttria-stabilized-zirconia (8YSZ), dense-vertically-cracked (DVC) TBC that was chemically “tagged” by doping it with small amounts of a rare earth element. The taggant element is not commonly found in the gas turbine exhaust, and it causes the TBC to fluoresce with ultraviolet illumination. Those two properties enable two levels of coating odometry:

1. Exhaust spall detection: The presence of the taggant material in the turbine exhaust enables on-line detection of a coating spall during turbine operation.
2. Fluorescent spall location: The enhanced contrast of the fluorescent TBC produces high definition of spall locations on turbine components during in-situ inspection without part removal.

A design for six sigma (DFSS)—a quality methodology based on the principles of predictive, statistical design—was used to establish the optimal amount of taggant material that would enable highly sensitive coating health monitoring without compromising TBC thermal and mechanical properties. Three taggant elements doped into 8YSZ at 1 wt% level were identified as feasible for the exhaust spall detection and fluorescent spall location functions. One of these taggants was studied in detail; its inclusion in the TBC had minimal effect on the TBC properties over the relatively wide compositional range between 0.5 and 5 wt%.

The firing temperature of a gas turbine determines its power output and fuel consumption; it also affects the extent of wear on the turbine parts, thereby dictating the length of maintenance intervals. The objective of the Adaptive Control System was to determine the firing temperature of a gas turbine that maximizes the operational profit generated from sales of electricity minus fuel cost, gas turbine parts cost, and other fixed costs while satisfying operational and environmental constraints. The natural formulation of this problem is both nonlinear and non-convex, which makes any real-time optimization application impossible. Preliminary models were acquired and assembled onto a common platform in a modular fashion for the optimizer algorithm. New inputs from the Flame Temperature Sensor, the Fuel Quality Sensor, and the Coating Life Odometer will play an important role in increasing the accuracy of models that are used by the Adaptive Control System/Optimizer. The original optimization problem was transformed into an alternative optimization formulation that has a convex objective function and linear constraints. A novel algorithm was formulated to reach the execution speed requirements of a supervisory control system; execution speeds were demonstrated in a one-minute time frame. Depending on the types of constraints the power plants are subject to, gas turbine life can be lengthened while production constraints are met and profit maximized. The robustness of the algorithm to uncertainties in electricity prices was also investigated. Using historical data of electricity price variations and distribution-fitting techniques, variability in electricity prices on the algorithm was validated. A sensitivity analysis using Monte Carlo simulations showed very encouraging results. This analysis shows that, by incorporating a weekly update of electricity prices to the model, the profitability predictions obtain near perfect results. Robustness of the optimization with respect to changing electricity prices is established by receding horizon application of optimization with continuous updates on models and a weekly update of electricity price information.

Final Report

TABLE OF CONTENTS

GENERAL INTRODUCTION.....	1
EXECUTIVE SUMMARY	2
1 FLAME TEMPERATURE SENSOR.....	5
1.1 INTRODUCTION	5
1.2 INNOVATIVE APPROACH TO FLAME TEMPERATURE SENSING	5
1.3 OBJECTIVE	6
1.4 APPROACH	7
1.4.1 GaN, AlGaN Photodiodes.....	7
1.4.2 Integral Multiple Layer Dielectric Filters on SiC Photodiodes	9
1.4.2.1 Characterization of Multiple Layer Dielectric Filters.....	9
1.4.3 The SiC Dual Diode.....	13
1.4.3.1 Dual Diode Design Considerations	13
1.4.3.2 Dual Diode Test Results (FTS01) and Fault Verification Experiments.....	19
1.4.3.2.1 Optical Test Results.....	19
1.4.3.2.2 Electrical Test Results	22
1.4.3.2.3 Isolation Tests.....	23
1.4.3.2.4 Reverse Leakage Current Tests	23
1.4.3.2.5 Parasitic NPN Bipolar Transistor Tests.....	24
1.4.3.3 Discussion of FTS01 Dual Diode Tests.....	29
1.4.4 The Fiber Optic Spectrometer.....	29
1.5 THE COMBUSTION PROCESS AND CONCEPT UNIQUENESS	29
1.6 EXPERIMENTAL	31
1.6.1 The Atmospheric Rig with LM6000 Premixing Flame Holder.....	31
1.6.1.1 Calibration of Revised Atmospheric LM6000 Premixed Combustor Flame	32
1.6.2 Combustor Experiments and Results.....	34
1.6.2.1 Combustor Test Results and Dual Diode Simulations Using Spectrometer Data	34
1.6.2.2 Spectrometer Data	36
1.7 DISCUSSION OF RESULTS.....	40
1.7.1 Sensor Calibration.....	40
1.8 DISTRIBUTED CONTROL SYSTEM FACTORS.....	41
1.9 CONCLUSIONS.....	41
1.10 REFERENCES	42

Final Report

2 FUEL QUALITY SENSOR	43
2.1 INTRODUCTION	43
2.2 DEVICE DEVELOPMENT	43
2.2.1 Lower Heating Value Sensor Production	44
2.2.1.1 Microhotplate Design	44
2.2.1.2 Microhotplate Fabrication	45
2.2.1.3 Design Modifications.....	45
2.2.1.4 Microhotplate Design Iterations	46
2.2.2 Modeling.....	47
2.2.3 Catalysts.....	49
2.2.3.1 Catalyst Preparation.....	49
2.2.3.2 Catalyst Deposition.....	49
2.3 EXPERIMENTAL	50
2.3.1 Apparatus.....	50
2.3.1.1 Test Fixtures	50
2.3.1.2 Control Circuits	51
2.3.1.3 Gas Delivery and Data Acquisition System	53
2.3.1.4 Testing Protocols	55
2.4 RESULTS AND DISCUSSION	55
2.4.1 Delta Plots.....	55
2.4.1.1 Diverse Combustion Behavior.....	56
2.4.2 Speciation.....	57
2.4.3 Expanded Limits of Flammability and Combustion Efficiency	57
2.4.4 Calibration Curves for NG at Constant Flow	59
2.4.5 Validation and Combustion Modeling.....	60
2.5 CONCLUSION.....	63
2.6 REFERENCES	64
3 COATING LIFE ODOMETER.....	66
3.1 INTRODUCTION	66
3.1.1 Condition-Based Maintenance.....	66
3.1.2 Coating Odometer Design	67
3.2 EXPERIMENTAL	70
3.2.1 Coating Health Monitoring.....	70

Final Report

3.2.1.1 Exhaust Detection Test	70
3.2.1.2 Fluorescent Spall Test	72
3.2.2 TBC Properties	73
3.2.2.1 Light Microscopy	73
3.2.2.2 Tensile Adhesion Strength	73
3.2.2.3 In-Plane Elastic Modulus	73
3.2.2.4 FCT Life	74
3.2.2.5 Phase Stability	74
3.2.2.6 JETS Testing	74
3.2.2.7 Erosion Testing	74
3.2.2.8 Thermal Conductivity	75
3.3 RESULTS	75
3.3.1 Taggant Identification	75
3.3.2 Composition Optimization	77
3.3.2.1 Microstructure	78
3.3.2.2 Tensile Adhesion Strength	79
3.3.2.3 In-Plane Elastic Modulus	81
3.3.2.4 FCT Life	81
3.3.2.5 Phase Stability	81
3.3.2.6 JETS testing	83
3.3.2.7 Erosion testing	83
3.3.2.8 Thermal conductivity	84
3.3.3 TBC Performance	85
3.4 DISCUSSION	85
3.5 CONCLUSIONS	86
3.6 REFERENCES	86
4 ADAPTIVE CONTROL SYSTEM	88
4.1 INTRODUCTION	88
4.2 MODEL AND PROBLEM FORMULATION	89
4.2.1 Gas Turbine Models	89
4.2.2 Problem Formulation	90
4.2.2.1 Natural Formulation of the Optimization Problem	91
4.2.2.1.1 Formulation-1 : For a user-specified maintenance interval	91

Final Report

4.2.2.1.2 Formulation-2 : For determining the optimal maintenance interval.....	91
4.2.2.2 Application of Real-Time Optimization for Process Control.....	92
4.2.2.3 Model Predictive Control	92
4.3 ANALYSIS.....	94
4.3.1 The Optimizing Algorithm	94
4.3.1.1 Input-Output Relationship of the Algorithm	94
4.3.2 Robustness Analysis	94
4.3.3 Computational Studies.....	100
4.4 ANALYSIS.....	100
4.4.1 Optimization Formulations Applied to Combined Cycle Power Plant Operation.....	100
4.4.1.1 Case Studies.....	101
4.5 CONCLUSIONS.....	102
4.6 REFERENCES	103
GENERAL CONCLUSIONS AND FUTURE PLANS.....	104
ACKNOWLEDGMENTS	106
ACRONYMS AND ABBREVIATIONS.....	107

Final Report

LIST OF TABLES

Table 1-1. Dual Diode Test Plan.....	18
Table 1-2. Isolation Tests between Unfiltered (U) and Filtered (F) Diodes	23
Table 1-3. Reverse Leakage Current for Unfiltered (U) and Filtered (F) Diodes.....	24
Table 1-4. Transistor Gain Measurements for Several Packaged Dual Photodiodes.....	27
Table 2-1. Composition of Natural Gas Standards	54
Table 2-2. Catalytic versus Conventional Limits of Flammability	58
Table 2-3. Combustion Efficiencies.....	58
Table 2-4. Repeatability of 303100-U Combustion Signal.....	60
Table 2-5. GC Analysis of Natural Gas Standard	63
Table 3-1. Description of the 4 Taggant-A -doped 8YSZ Coating Sets Evaluated and the Methods of Powder Synthesis.....	78
Table 3-2. Density and Thermal Conductivity of 2 Baseline 8YSZ TBCs and 2 Taggant-A -doped 8YSZ TBCs. Thermal conductivity measured at 2 temperatures and under 2 gas atmospheres.	85
Table 4-1. Robustness Analysis Results	99

Final Report

LIST OF FIGURES

Figure 1-1. Schematic diagram of the flame temperature sensor. The sensor housing will contain two amplifiers. Data collection, including the A/D converters, will be done outside the test cell.....	6
Figure 1-2. Transmission characteristics of GaN and Al _x Ga _{1-x} N compounds with various amounts of Al, from x=0 to x=0.48, compared with a multiple dielectric filter, all on sapphire substrates.....	8
Figure 1-3. GaN p-i-n photodiode spectral responsivity (Sandvik et al. 2000).....	9
Figure 1-4. Optical models of transmission characteristics using the ordinary (n _o) and extraordinary (n _e) indices of refraction for SiC (left) and a SiC model (with 6000 Å SiO ₂) and sapphire (right).....	10
Figure 1-5. Multiple dielectric filter transmission as a function of incident angle.....	10
Figure 1-6. Multiple dielectric filter transmission as a function of temperature.....	11
Figure 1-7. Transmission comparison between the measured dielectric stack (AELP 316) and the theoretical calculation of transmission for the same filter.....	11
Figure 1-8. Filter evaluation before and after annealing.....	12
Figure 1-9. Filter transmission characteristics before and after annealing. At left, the filter uniformity, and at right, the range at each wavelength.....	13
Figure 1-10. Top view of the FTS01 dual diode layout showing both filtered and unfiltered zones.....	14
Figure 1-11. Optical beam intensity profile in relative units from edge to edge illuminating the present 1 mm ² SiC chip in production sensor. This distribution has a Gaussian profile, with a standard deviation of 135 microns.....	15
Figure 1-12. Basic chip design considerations. The interdigitated design should provide tolerance for the Gaussian illumination pattern and misalignment of the chip.....	15
Figure 1-13. The effect of beam misalignment in multi-fingered SiC photodiodes.....	16
Figure 1-14. An optical cross talk simulation.....	17
Figure 1-15. Cross section zone of the SiC dual diode showing the filtered and unfiltered fingers and a Mo stripe in the mesa trenches that is required to optically isolate adjacent fingers..	17
Figure 1-16. Top view of the dual diode.....	18
Figure 1-17. 1-mm ² dual diodes with different finger widths and pitches.....	19
Figure 1-18. Standard SiC photodiode fabricated by GE for Reuter Stokes flame detectors.....	19
Figure 1-19. Spectral responsivity of various dual diodes.....	20
Figure 1-20. Most of the chip at the left is covered with epoxy, with the center circle over the active area. At the right is an uncovered chip, shown for comparison.....	21
Figure 1-21. Normalized photoresponse of PD65, before and after the application of epoxy in areas over the curf.....	21

Final Report

Figure 1-22. Normalized photoresponse of a photodiode with fingers, PD61, that is completely covered by a filter before and after the application of epoxy in areas over the curf.	22
Figure 1-23. Isolation test configuration. For this test, the anode (A) is floating and a voltage is applied between the unfiltered cathode (CU) and the filtered cathode (CF).	23
Figure 1-24. Reverse leakage current test configuration where measurement is made between the anode (A) and either cathode (CF or CU) with the third terminal floating.	24
Figure 1-25. Parasitic NPN bipolar transistor test where the anode serves as the base, either the unfiltered cathode or the filtered cathode serves as the emitter, and the third terminal serves as the collector.	25
Figure 1-26. Electron diffusion length versus electron lifetime for 6H-SiC, p-type epitaxial layer, $N_a=1e16 \text{ cm}^{-3}$, $\mu_n=300 \text{ cm}^2/\text{Vsec}$	25
Figure 1-27. Configuration used to measure bipolar transistor gain.	26
Figure 1-28. Gummel plot of a packaged dual photodiode, dark conditions. The base current is shown on the left vertical axis, the collector current on the right vertical axis, and the base voltage is shown by the horizontal axis on the bottom.	26
Figure 1-29. Gummel plot of a packaged dual photodiode showing significant conductance between cathode fingers. The base current is shown on the left vertical axis, the collector current on the right vertical axis, and the base voltage is shown by the horizontal axis on the bottom.	28
Figure 1-30. Leakage current of individual filtered and unfiltered diodes (dark conditions). The current is shown on the vertical axis, and the voltage is shown on the horizontal axis on the bottom.	28
Figure 1-31. Data showing signal distribution at 3160°F flame temperature caused by flame emission fluctuations, and standard deviation of filtered and unfiltered signals versus temperature.	31
Figure 1-32. Flame temperature variation through the flame near the exhaust end of the quartz liner.	32
Figure 1-33. Distributed emissions probe.	33
Figure 1-34. Comparison of flame temperatures determined by the oxygen emission probe and combustible gas flows.	34
Figure 1-35. Simulated ratios using spectrometer data for the four 1.5 mm chips. At left, the as-simulated values (no gain), and at right, those values multiplied by 3.	35
Figure 1-36. Comparison of simulated and measured ratios of PD26.	35
Figure 1-37. Experimental apparatus for flame temperature measurements using either an optical fiber optic spectrometer or dual SiC photodiode sensor.	36
Figure 1-38. Spectral intensity versus position of the flame. The integrated intensity for the range of 180 to 870 nm (left) and the line intensity at 310 nm (right) show relatively good agreement.	37
Figure 1-39. R(T) spectrometer data using a ratio of the OH band intensity as specified.	37

Final Report

Figure 1-40. Spectrometer R(T) prediction interval and confidence interval.....	38
Figure 1-41. R(T) data obtained using the first generation Dual Diode Sensor.	39
Figure 1-42. Mod 1 Dual Diode Sensor R(T) predication interval and confidence interval.	39
Figure 2-1. Schematic of a microhotplate cross section.	44
Figure 2-2. Top view of a microhotplate.	44
Figure 2-3. Image of Hot 7 design.	46
Figure 2-4. Front and back view of the 10-element array.....	47
Figure 2-5. Infrared microscope image of a microhotplate.	47
Figure 2-6. ANSYS model of microhotplate.	48
Figure 2-8. Printed Pt catalyst pad.	50
Figure 2-9. Combustion fixture.....	51
Figure 2-10. Schematic of the constant resistance control circuit.	52
Figure 2-11. Buffered control circuit.	53
Figure 2-12. Schematic of test setup.....	54
Figure 2-13. LHV sensor response.	56
Figure 2-14. Delta plot.	56
Figure 2-15. Contour plots of catalyst combustion behavior.....	57
Figure 2-16. Combustion varying by catalyst spot size.	59
Figure 2-17. Combustion of different NG standards.	60
Figure 2-18. Micropenned Pt catalyst in a u-tube reactor.....	61
Figure 2-19. Comparison of u-tube and LHV sensor data.....	61
Figure 2-20. Pt and Pd catalyst comparison in u-tube.	62
Figure 2-21. Chromatogram of natural gas.....	63
Figure 3-1. Schematic cross section of the smart TBC concept. The TBC is made of 2 layers. The outer layer is the standard TBC composition. The inner layer (colored orange in the image) has a rare earth taggant element incorporated in the TBC.....	67
Figure 3-2. Schematic drawing of the exhaust taggant detection concept. The taggant element in the layer of TBC near the bondcoat is liberated into the exhaust stream by a failure of the TBC. Detection of the taggant in the particulate collector gives an on-line indication of coating loss.....	68
Figure 3-3. Smart TBC coupon with fluorescent TBC layer under a standard TBC layer.....	69
Figure 3-4. Two coupons with smart TBCs, illuminated by a) white light and b) ultraviolet light. The upper coupon is as-fabricated and the lower coupon has 2 areas with the taggant layer exposed through erosion.	69

Final Report

Figure 3-5. Combustion rig test for exhaust taggant detection feasibility with a combustor section in which powder was introduced into a combustion flame through the powder inlet and the exhaust was sampled into the filter apparatus through a port downstream.....	70
Figure 3-6. Plot of amount of taggant detected in the exhaust filter versus the amount of taggant powder released into the combustor for 2 taggant compounds, Taggant-A (blue diamonds) and Taggant-B (red squares).....	72
Figure 3-7. Image of fluorescence intensity of TBC coupons with a compositional range of Taggant-A in 8YSZ of between 20 wt% to 0.5 wt%, as indicated in the image below each coupon.....	73
Figure 3-8. Images of standard 8YSZ TBC (Y) and 8YSZ TBCs doped with rare earth elements (Taggants A, B, and C) under illumination using 254 nm (1.0×10^{-5} in) ultraviolet light. ..	76
Figure 3-9. ANOVA of tensile adhesion strengths of 8YSZ TBCs doped with 3 different rare earth elements compared with the baseline TBC with no taggants. Baseline data was taken for samples fabricated during the same coating campaign.	76
Figure 3-10. ANOVA for FCT cycles to failure for TBCs with 3 different taggant materials compared with baseline 8YSZ.....	77
Figure 3-11. Cross-sectional microstructures of TBCs sprayed with: a) Norton AG1 8YSZ, b) Muscle Shoals 8YSZ, c) Treibacher 1.0 Taggant-A -8YSZ, and d) Treibacher 5.0 Taggant-A -8YSZ powders.....	79
Figure 3-12. Tensile adhesion strength versus wt% of Taggant-A in 8YSZ for 3 powder coating runs.....	80
Figure 3-13. One-way ANOVA for tensile adhesion strength as a function of wt% of Taggant-A in 8YSZ. No statistically significant difference was observed.	80
Figure 3-14. Bend modulus versus wt% Taggant-A for 2 powder coating runs. All samples had a low modulus with no effect of Taggant-A composition.	81
Figure 3-15. Furnace cycle life versus wt% Taggant-A for 3 powder coating runs. Given the scatter in lives of the baseline 8YSZ, there is no effect of Taggant-A between 0.5-10 wt%.	82
Figure 3-16. Monoclinic and cubic phase contents of TBCs as a function of % Taggant-A after a heat treatment of 1000 hours at 1400°C (2552 °F).....	83
Figure 3-17. Mass loss rate during erosion test for the 4 optimization TBCs after JETS test exposure. TBCs with Taggant-A had a higher mass loss rate and lower erosion resistance than the 8YSZ TBCs.....	84
Figure 4-1. Schematic of Model Predictive Control methodology.....	93
Figure 4-2. Input-output relationship of the proposed optimizer.....	94
Figure 4-3. Best distribution fit to historical electricity prices during 1997-1999	96
Figure 4-4. Application of growing uncertainty in electricity prices in Monte Carlo simulations.	97
Figure 4-6. Profit distribution with base-load profile.	98

Final Report

Figure 4-7. Overview of a Combined Cycle plant with one gas turbine, a steam turbine, and a heat recovery steam generator.	100
Figure 4-8. Simple Cycle operation principle.....	101
Figure 4-9. Combined Cycle operation principle.....	102

Final Report

GENERAL INTRODUCTION

Gas turbines are the choice technology for high-performance power generation and are employed in both simple and combined cycle configurations around the world. The Smart Power Turbine (SPT) program has developed new technologies that are needed to further extend the performance and economic attractiveness of gas turbines for power generation. Today's power generation gas turbines control firing temperatures indirectly, by measuring the exhaust gas temperature and then mathematically calculating the peak combustor temperatures. But temperatures in the turbine hot gas path vary a great deal, making it difficult to control firing temperatures precisely enough to achieve optimal performance. Similarly, there is no current way to assess deterioration of turbine hot-gas-path components without shutting down the turbine. Consequently, maintenance and component replacements are often scheduled on conservative design practices based on historical fleet-averaged data. Fuel heating values vary with the prevalent natural gas fuel, and the inability to directly measure heating value with sufficient accuracy and timeliness can lead to sub-optimal maintenance and operational decisions. GE Global Research Center, under this Smart Power Turbine program, has developed a suite of novel sensors that would measure combustor flame temperature, online fuel lower heating value (LHV), and hot-gas-path component life directly. These sensors and controls would be applicable to both new and existing turbines. By enabling turbines to operate much closer to their design limits, it may be possible to significantly increase the incremental/marginal capacity of gas turbine systems, which would mean cost savings for the power industry and more electric power for the nation's consumers.

This report presents the development and demonstration of the following technologies for integration into a real-time Smart Power Turbine:

- Flame Temperature Sensor – A wavelength-selective photodiode system provides accurate flame temperature, resulting in higher turbine efficiency and more accurate estimation of NO_x. This sensor can be used in a closed loop control to help optimize turbine performance. It also contributes to residual life estimation for combustor liner and turbine section parts. The development and the demonstration of the flame temperature sensor are described in detail in Section 1.
- Fuel Quality Sensor system – A Lower Heating Value (LHV) sensor is used to establish the heat content of the fuel which, in conjunction with the flame sensor, will enable more accurate determination of efficiency, and will also support monitoring of combustor and turbine performance. The development and demonstration of the LHV fuel quality sensor are described in detail in Section 2.
- Coating Life Odometer - Taggant can be used to identify loss of environmental coatings from the combustor liner and other hot-gas-path parts; taggant will also detect incipient failures of these parts. The development and demonstration of the taggant for the coating odometer under this task are described in detail in Section 3.
- Adaptive Control System – This system is capable of translating these sensor inputs and other data into optimal control, life extension, and condition-based maintenance strategies. The development and demonstration of adaptive control system are described in detail in Section 4.

Final Report

EXECUTIVE SUMMARY

Power turbine design and industry practices are conservative. They are driven by a lack of precise information about machine operating conditions and about remaining life. Technological gaps limit the information available from the turbine to fully optimize its design and operation in terms of efficiency, life-cycle cost, and emissions output. Performance is affected by a number of variables, many of which cannot at present be monitored appropriately because there are no sensors that can (1) perform in near real-time and (2) reliably survive the combustion environment. One of these variables is fuel quality, which is measured intermittently offline (practices vary), generally by the fuel suppliers. Another is temperatures in the hot gas path, which are not known precisely. Data on fuel quality and hot gas path temperature are both critical for detailed performance evaluation. Current design practices for scheduled maintenance intervals are based upon a worst-case parts life assumption of minus 4 sigma (standard deviations) from mean fleet life. Thus, by definition, more than 99% of maintenance outages are taken to service largely healthy equipment! Current control system algorithms and maintenance schedules are based on fixed (as designed and installed) assumptions. Low-fidelity modeling of the combustion process is the result of a lack of advanced sensor data and the simple deterministic approach of today's controls systems. As can be seen, current gas turbine operations are non-optimal in many ways. Smarter machines and operations could achieve tremendous payback in future gas turbine operations. The Smart Power Turbine has addressed these issues by developing a suite of novel sensors that would measure combustor flame temperature, measure online fuel lower heating value (LHV), and measure hot-gas-path component life directly, and a control algorithm capable of translating these sensor inputs and other variables into optimal control, life extension, and condition-based maintenance strategies.

Under the Flame Temperature Sensor development task, the feasibility of using the ratio of the integrated intensities of portions of the OH emission band to determine the specific average temperature of a premixed methane or natural-gas-fueled combustion flame was demonstrated. The temperature determined is the temperature of the plasma included in the field of view of the sensor. Two sensor types were investigated: the first used a low-resolution fiber optic spectrometer; the second was a SiC dual photodiode chip. Both methods worked. Sensitivity to flame temperature changes was remarkably high, that is, a 1 to 2.5% change in ratio for an 11.1°C (20°F) change in temperature at flame temperatures between 1482.2°C (2700°F) and 1760°C (3200°F). Sensor ratio calibration was done using flame temperatures determined by calculations using the amount of unburned oxygen in the exhaust and by the fuel/air ratio of the combustible gas mixture. The agreement between these two methods was excellent. The sensor methods characterized are simple and viable

The lower heating value (LHV) Fuel Quality Sensor consists of a catalytic film deposited on the surface of a microhotplate. This micromachined design has low heat capacity and thermal conductivity, making it ideal for heating catalysts placed on its surface. High-temperature stable supported catalytic materials provide a natural surface-based method for flame ignition and stabilization. Several methods of catalyst deposition were investigated, including micropen deposition and other proprietary methods, which permit precise and repeatable placement of the materials. The use of catalysts on the LHV sensor expands the limits of flammability (LoF) of combustion fuels as compared with conventional flames; an unoptimized LoF of 1 to 32% for natural gas (NG) in air was demonstrated with the microcombustor, whereas conventionally 4 to

Final Report

16% is observed. The LoF for hydrogen, methane, propane and ethane are likewise expanded. The primary goal of this work was to measure the LHV of NG fuels. Of secondary interest was the determination of the relative quantities of the various components of NG mixes. As part of this effort, it was demonstrated that by using an array of different catalysts operating at different temperatures, the relative amounts of components of the mixture could be determined. This technique is based on the fact that, depending on catalyst type and temperature, the various components of NG (e.g., methane, ethane, propane, and butane) have different combustion behavior. The combustion parameters for methane were shown to be dependent on whether Pt or Pd catalysts were used. To make a commercial LHV sensor system, several key elements are needed: a robust sensor, packaging, flow control and temperature control circuitry (for both the packaging and the sensor itself). In this project, significant effort was expended on making the LHV platform more robust, including the addition of high-temperature stable materials, such as tantalum, and the use of passivation overcoats to protect the resistive heater/sensor materials from degradation in the combustion environment. Modeling and simulation were used to predict improved sensor designs. Overall, this project has been successful in demonstrating the viability of this approach to LHV measurement and has shown what steps are necessary to bring this sensor to commercialization.

The Coating Life Odometer task demonstrated the technical feasibility of a “smart” thermal barrier coating (TBC) that indicates its service condition during turbine operation. The smart TBC was based on a state-of-the-art 8 wt% yttria-stabilized-zirconia (8YSZ), dense-vertically-cracked (DVC) TBC that was chemically “tagged” by doping it with small amounts of a rare earth element. The taggant element is not commonly found in the gas turbine exhaust, and it causes the TBC to fluoresce with ultraviolet illumination. Those two properties enable two levels of coating odometry:

3. Exhaust spall detection: The presence of the taggant material in the turbine exhaust enables on-line detection of a coating spall during turbine operation.
4. Fluorescent spall location: The enhanced contrast of the fluorescent TBC produces high definition of spall locations on turbine components during in-situ inspection without part removal.

A design for six sigma (DFSS)—a quality methodology based on the principles of predictive, statistical design—was used to establish the optimal amount of taggant material that would produce a high sensitivity of coating health monitoring without compromising TBC thermal and mechanical properties. Three taggant elements doped into 8YSZ at 1 wt% level were identified as feasible for the exhaust spall detection and fluorescent spall location functions. One of these taggants was studied in detail; its inclusion in the TBC had minimal effect on the TBC properties over the relatively wide compositional range between 0.5-5 wt%.

The technical team addressed the problem of optimally running a gas turbine to maximize the operational performance (profit generated) for a power utility faced with fluctuating energy prices and changing operating conditions. Adjusting the firing temperature of a gas turbine varies its power output and fuel consumption. The firing temperature also affects the extent of wear and tear on the turbine parts, thereby dictating the length of maintenance intervals. The objective of the Adaptive Control System (Supervisory Control/Optimizer) is to determine the firing temperature of a gas turbine that maximizes the operational profit generated from sales of electricity minus fuel cost, gas turbine parts cost, and other fixed costs while satisfying

Final Report

operational and environmental constraints. The natural formulation of this problem is both nonlinear and non-convex, which makes any real-time optimization application impossible. However real-time optimization is key to the success of model-based optimization technology, since real-time model updates, either by sensor information or user input, enable optimization of the power plant to current plant and market conditions. Thus optimization speed and accuracy are key features in this task.

Preliminary models were acquired and assembled onto a common platform in a modular fashion for the optimizer algorithm. New sensor inputs also play an important role in increasing the accuracy of models that are used by the optimizer. The original optimization problem was transformed into an alternative optimization formulation that has a convex objective function and linear constraints. A novel algorithm was formulated to solve this new problem of meeting the execution speed goals required of a supervisory control system. Execution speeds were demonstrated in a one-minute time frame. Optimization results have shown that using a supervisory control system in a power plant can achieve significant theoretical benefits in power plant operation. Depending on the types of constraints the power plants are subject to, gas turbine life can be lengthened while production constraints are met and profit maximized. The team also investigated the robustness of the algorithm to uncertainties in electricity prices and tested it by simulations. Theoretical analysis on electricity price distributions were investigated and validated with distribution-fitting techniques using historical data. Using the outcome of this study, a sensitivity analysis was done using Monte Carlo simulations, and very encouraging results were obtained. The analysis shows that, by incorporating a weekly update of electricity prices to the model, the profitability predictions obtain near perfect results. Robustness of the optimization with respect to changing electricity prices is established by receding horizon application of optimization with continuous updates on models and a weekly update of electricity price information.

Final Report

1 FLAME TEMPERATURE SENSOR

1.1 INTRODUCTION

Previous publications describing the properties of the SiC photodiode have reported that a SiC photodiode is ideal for flame monitoring (Brown, Downey et al. 1991; 1998). That is because the SiC photodiode responsivity curve overlaps the intense OH emission band in the UV between 305 and 340 nm. The SiC photodiode is an ideal candidate for a UV sensor because of its high sensitivity and extremely low dark current, which allows for the use of high gain amplifiers without producing offset voltages.¹ These advantages have been used to produce SiC flame detectors for gas turbine control systems that can track flame intensity over a wide range of operating conditions: flame on/off, mode switching, load or power level from startup to full-load, and flame dynamics using the AC component of the signal. These detectors cannot, however, be used to determine the combustion flame temperature.

The OH emission band is produced by the combustion process using hydrocarbon fuels and air. The presence of N in the air produces NO_x. Tight control of the combustion process is desirable to maintain low NO_x and the maximum possible combustion efficiency. The OH band has the highest intensity in the UV region and is essentially isolated from all the other emission bands produced by the combustion process. Other bands such as the CO band at 220 nm and the CN and CH bands at 390 nm and 430 nm are either much weaker or outside the responsivity envelope of the SiC photodiode.

For many years scientists have attempted to arrive at a good method of determining the temperature of a combustion flame by optical methods. Emission spectra were used in many of these studies, and ratios of peak intensities were calculated. Some examples are ratios of the OH and CO₂ or OH and CH band peak intensities (Brown and Henkes 1991) or OH (309 nm) and OH (307 nm) line intensities (Vaidza et al. 1982), or a series of line intensities using high-resolution spectrometers (Dean 1994). These methods were impractical or they resulted in low sensitivity to change in flame temperature. Another approach, which is more complex, is the absorption method, which uses rapid tuning laser wavelength modulation to determine the change in individual spectral line shapes (Rea 1991). This approach requires a sender (tunable laser) and receiver (photodiode) at the appropriate wavelength. The purpose of the work reported here was to find out whether the emission characteristics of the OH band could be used to determine combustion flame temperature.

1.2 INNOVATIVE APPROACH TO FLAME TEMPERATURE SENSING

Optical emission intensity is not a direct indication of flame temperature. It can, however, be used to track output power levels as fuel levels change and firing modes are altered. Increases in fuel/air ratio increase emission intensity because more molecules are emitting photons. Because of the heat release occurring during combustion and because of internal radiant plasma gas heating, the flame temperature does increase, but emission intensity cannot be used as a direct indication of temperature because of the so-called fuel factor. The fuel factor is the name given

¹The dark current of a good 1 x 1 mm² SiC photodiode at 0.5 and 5 volts reverse bias is only 4 fA (0.4 pA/cm²) and 44 fA (4 pA/cm²), respectively.

Final Report

to the various combustion phenomena that result in a change in light output intensity but do not cause a corresponding change in flame temperature; for example, a change in combustion volume, a change in the number of flames present, or a reduction in transparency in the optical path of measurement. In order to derive a relationship between emission intensity and temperature, the fuel factor has to be canceled out by taking a ratio of two intensities.

The new concept described here is based on the change in shape of the OH emission band centered at 309 nm. This band is common to all hydrocarbon combustion processes and has been studied extensively by spectrometric methods for many years. Those studies concluded that the intensity of the emission lines in the long-wavelength region of the band increases more rapidly with increases in temperature than those in the short-wavelength region (Rea 1991). A ratio can therefore be obtained by splitting the band into at least two groups of emission lines. An inherent advantage of the ratio method is that the effect of coatings on the sensor window that reduce the window's transparency is also cancelled. It is assumed that there is still sufficient signal and that the coating acts like a neutral density filter over the wavelength region of the OH band.

1.3 OBJECTIVE

The purpose of this effort was to determine whether the new concept could achieve a sensitivity and accuracy of $\pm 20^\circ\text{F}$ for a premixed combustion flame over a range of flame temperatures between about 2600 and 3000°F. This immediate goal was established to enable control of the combustion process in GE Power Systems dry low NO_x (DLN) gas turbines so as to ensure minimum NO_x emissions and optimum efficiency. The long-term goal is to combine the capabilities of the present SiC flame temperature detector with the ability to measure flame temperature (Figure 1-1).

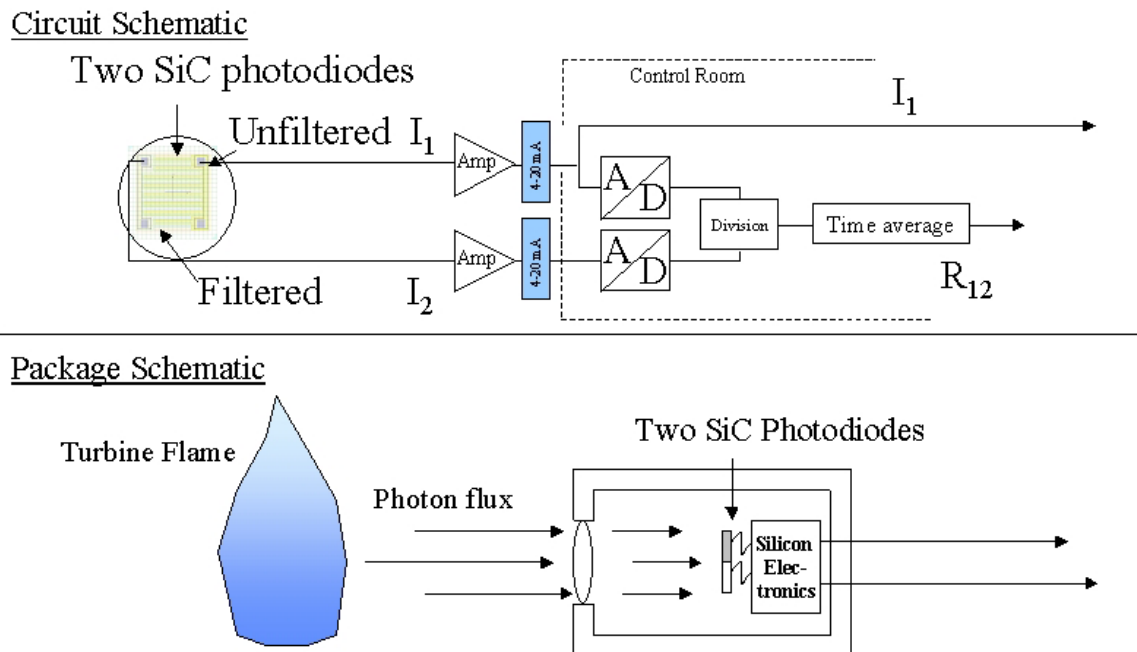


Figure 1-1. Schematic diagram of the flame temperature sensor. The sensor housing will contain two amplifiers. Data collection, including the A/D converters, will be done outside the test cell.

Final Report

1.4 APPROACH

Initial analytical calculations using the commercially available LIFBASE computer program, which describes how the OH line intensities change with temperature, indicated that a reasonable sensitivity to $\pm 20^\circ\text{F}$ flame temperature changes could be anticipated. Examples of OH line intensities as a function of wavelength for different temperatures can be found in Rea (1991, 319-322).

The calculations involve adding up all the line strengths (S_i) within each portion of the band after multiplying each line strength by the quantum mechanical form of the blackbody radiation law:

$$(8\pi h\nu^3/c^3)(e^{h\nu/kT} - 1)^{-1}$$

Because we are using a ratio the flame temperature ratio function is simply:

$$R(T) = \frac{I_i(T)}{I_j(T)} = \frac{\sum_i \nu_i^3 (\exp(h\nu_i / kT) - 1)^{-1} S_i}{\sum_j \nu_j^3 (\exp(h\nu_j / kT) - 1)^{-1} S_j}$$

This equation can be further simplified to read:

$$R(T) = (\sum_i B_i S_i) / (\sum_j B_j S_j)$$

Where B is the blackbody scaling factor as a function of wavelength.

Three hardware approaches were investigated in parallel. Each approach needed to supply the ratio of two segments of the OH band, that is, a ratio composed of (1) a numerator obtained by the integrated intensities of the emission lines in the long-wavelength region and (2) a denominator composed of the integrated line intensities of the entire band or of the short-wavelength region.

1.4.1 GaN, AlGaN Photodiodes

The potential advantage of using GaN and AlGaN alloys is that they may produce photodiodes with extremely sharp, long-wavelength responsivity cutoffs. That is because these semiconductor materials are direct band gap systems, which means the conduction band and valence band minimum are both centered at the same location in solid state momentum space and therefore do not require phonon-assisted optical transitions. That is not the case for SiC, which is an indirect band gap semiconductor and therefore exhibits a very broad, long-wavelength cutoff tail. Another advantage of the AlGaN system is that it can produce direct band gap semiconductor materials with band gaps varying between 3.4 eV (GaN) and 6.2 eV (AlN) with corresponding sharp wavelength responsivity cutoffs of between 365 nm and 200 nm, respectively. Therefore if these materials were used to make photodiodes, they would function as active filters to produce photocurrents for any tailored optical responsivity band between these two wavelengths.

This approach would use a GaN photodiode to measure the total intensity of the OH band between 200 nm and 365 nm, and an AlGaN photodiode with about 30% Al to measure the intensity between 200 nm and 313 nm. In order to obtain the integrated intensity of the long-wavelength region, the output of the AlGaN photodiode would have to be subtracted from the output of the GaN photodiode. The ratio of these two signals could be used directly since:

Final Report

$$R(T) = \frac{I_{\text{GaN}}(T) - I_{\text{AlGaN}}(T)}{I_{\text{GaN}}(T)} = 1 - \frac{I_{\text{AlGaN}}(T)}{I_{\text{GaN}}(T)}$$

The investigation proceeded by obtaining GaN and AlGaN films epitaxially grown on sapphire substrates. The transmission characteristics of these films are shown in Figure 1-2. GaN photodiodes were obtained from various sources or fabricated at GE Global Research Center (GEGRC). The very sharp, long-wavelength cutoff of a typical GaN photodiode is shown in Figure 1-3. The GaN photodiodes fabricated at GEGRC used a thin metal Schottky barrier on n-type material to avoid the difficulties of making p-type GaN material. These diodes exhibited larger dark currents than the SiC photodiodes. The p-i-n GaN and AlGaN photodiodes were obtained from others and the responsivities at 300 nm of both types were 2.5 to 4 times lower than a SiC photodiode at 300 nm.² The difficulty of making good AlGaN photodiodes using material containing about 30% Al required for the right cutoff at about 313 nm (Brunner et al. 1997) was indicated by reported long-wavelength cutoffs for photodiodes made from material with 20 to 30% Al that were gradual and not at all sharp. That result is in keeping with some of the transmission characteristics shown in Figure 1-2. This approach was abandoned since it was decided that the GaN, AlGaN photodiode technology was not sufficiently mature to be used for this program.

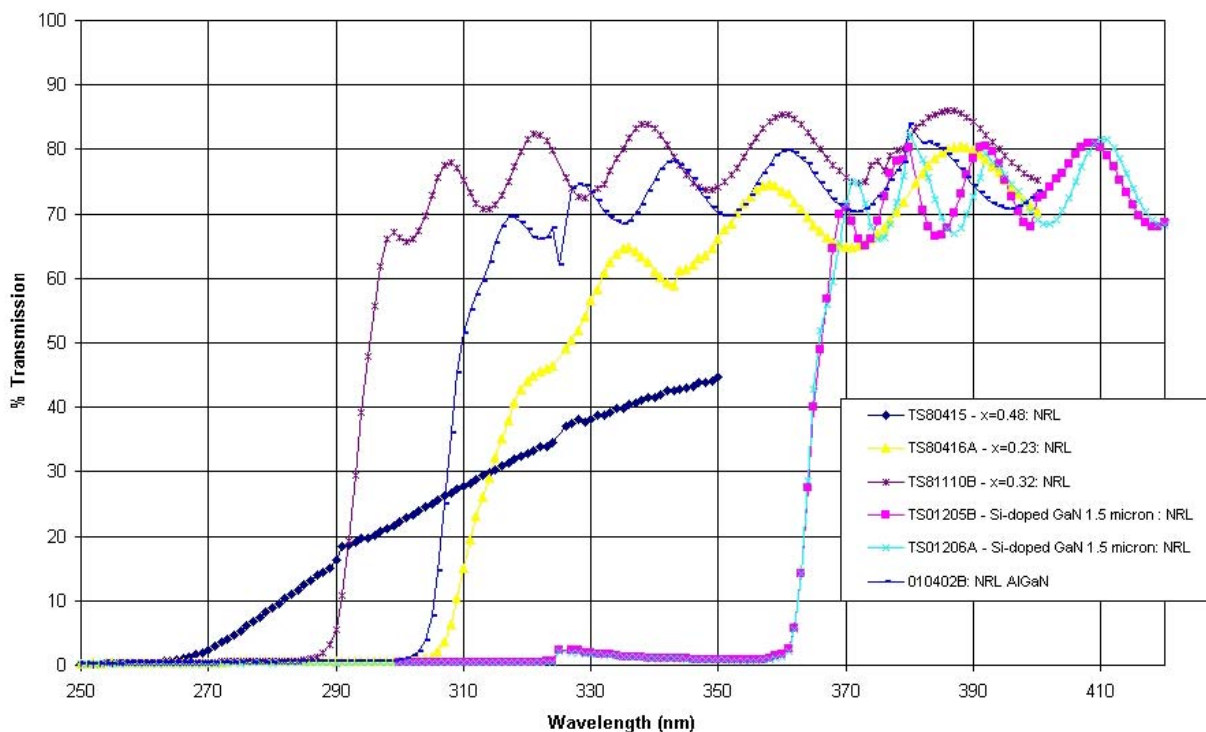


Figure 1-2. Transmission characteristics of GaN and Al_xGa_{1-x}N compounds with various amounts of Al, from x=0 to x=0.48, compared with a multiple dielectric filter, all on sapphire substrates.

² These GaN, AlGa_N and photodiode samples were obtained from various sources: Advanced Technology Materials, Inc.; the Naval Research Laboratory in Washington, DC; the Honeywell Solid State Division in Minneapolis, MN, and the Electrical Engineering Dept. of Northwestern University in Evanston, IL.

Final Report

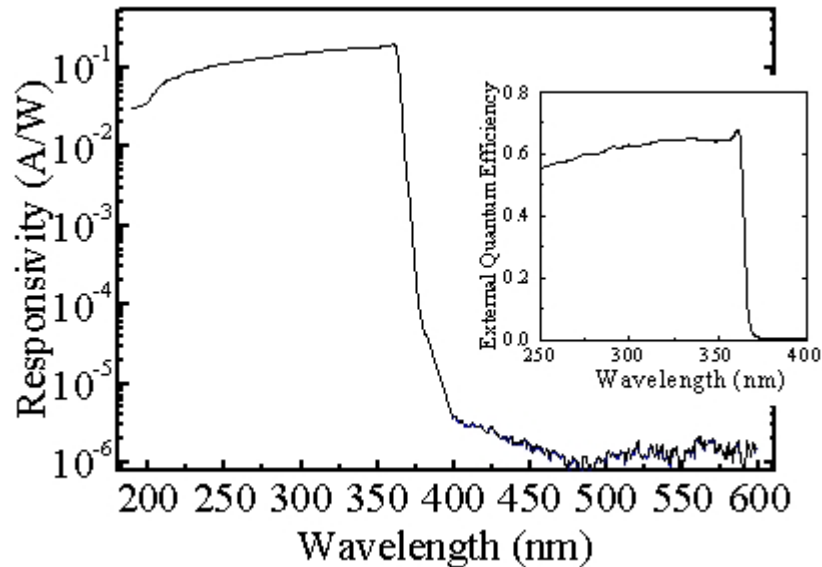


Figure 1-3. GaN p-i-n photodiode spectral responsivity (Sandvik et al. 2000).

1.4.2 Integral Multiple Layer Dielectric Filters on SiC Photodiodes

GEGRC has a well-established record of producing many thousands of SiC photodiodes with reproducible characteristics. Chip yield on processed wafers is also exceptionally high.

In this approach, which explores the possibility of using integral multiple layer dielectric filters, the integrated intensity of the long-wavelength region of the OH band between about 312 nm and 340 nm is obtained by using a long pass UV filter applied to the surface of a SiC photodiode. This intensity will be the numerator of the ratio, and the denominator will be the integrated intensity of the whole band obtained from an unfiltered SiC photodiode so that: $R(T) = I_{SiC}(\text{Long Pass Filtered}) / I_{SiC}(\text{Unfiltered})$.

1.4.2.1 Characterization of Multiple Layer Dielectric Filters

Multiple layer dielectric filters are composed of alternating thin layers of dielectric materials. Optical modeling to determine the transmission characteristics of these filters was carried out with sapphire and SiC substrates (Figure 1-4). The optical model at the left shows a very high degree of overlap between the ordinary and extraordinary index models for SiC, which means that variances in the polarization of light incident on the surface should not result in significantly different transmission behaviors. Further, the extent of the overlap indicated that the angle of incidence of radiation to the surface should have only a small or negligible effect.

Filters deposited on sapphire substrates were obtained in order to verify the analytical models. Angular dependence is shown in Figure 1-5. Figure 1-6 shows the transmission of this filter as a function of temperature.

Final Report

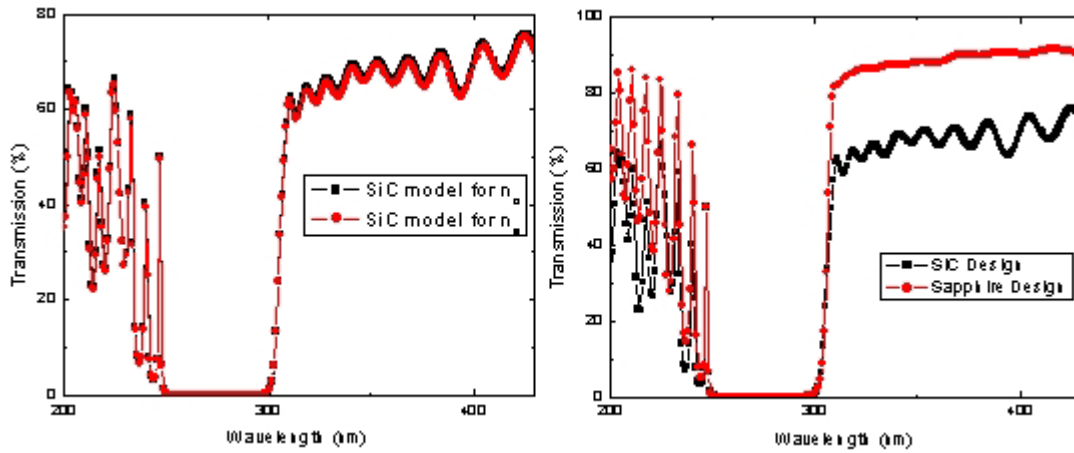


Figure 1-4. Optical models of transmission characteristics using the ordinary (n_o) and extraordinary (n_e) indices of refraction for SiC (left) and a SiC model (with 6000 Å SiO_2) and sapphire (right).

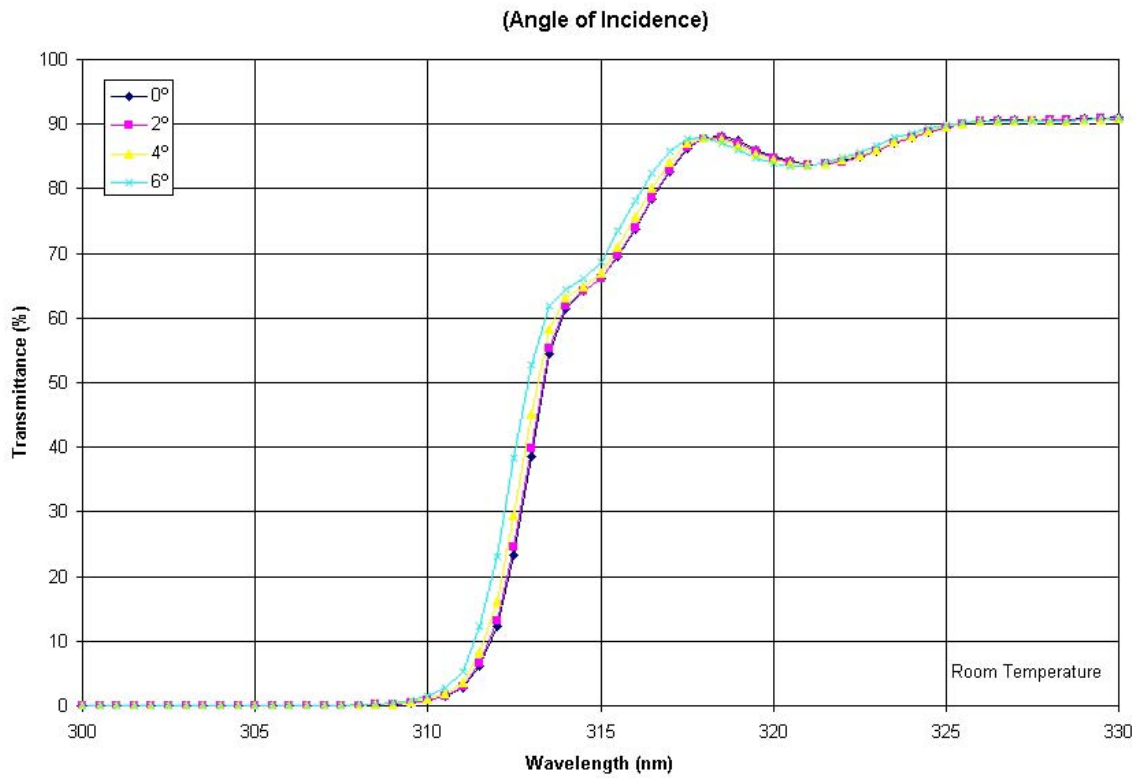


Figure 1-5. Multiple dielectric filter transmission as a function of incident angle.

Final Report

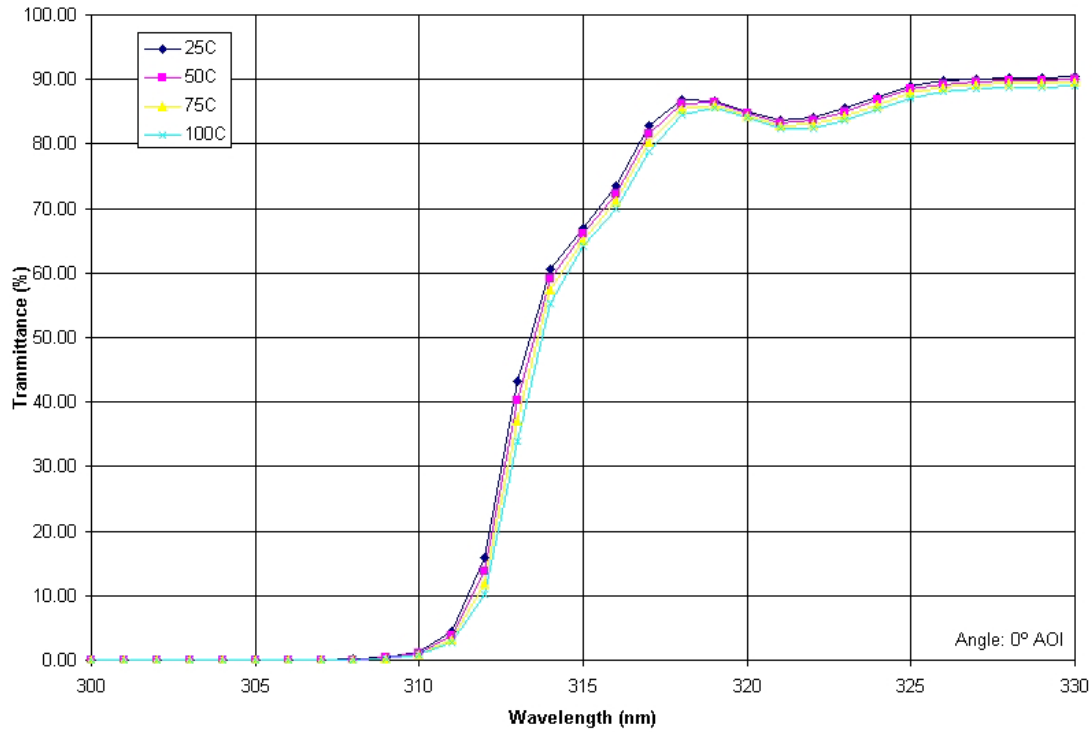


Figure 1-6. Multiple dielectric filter transmission as a function of temperature.

A comparison between analytical modeling and experimental results is shown in Figure 1-7.

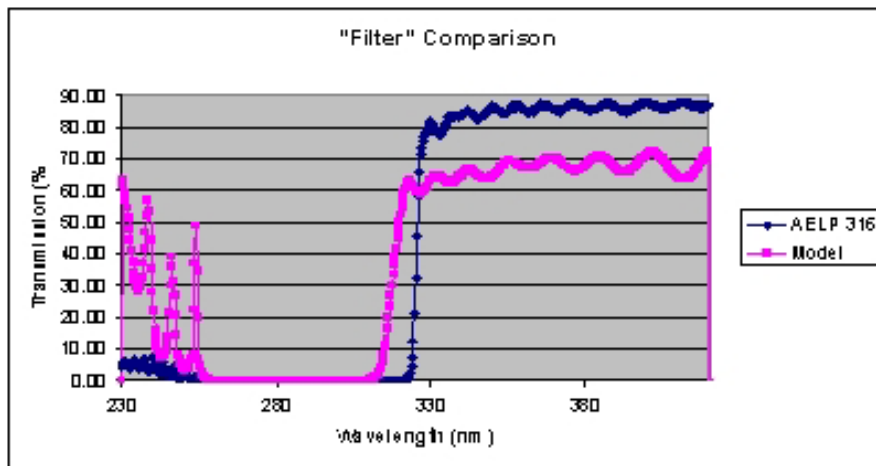


Figure 1-7. Transmission comparison between the measured dielectric stack (AELP 316) and the theoretical calculation of transmission for the same filter.

Results of an evaluation for uniformity and reliability are shown in Figures 1-8 and 1-9. The transmission properties of the filters were measured with a high-resolution spectrometer at

Final Report

several places across the wafer. Measurements were done before annealing, and after, with an annealing cycle at 350 °C for 10 minutes in air. This process simulated the highest temperature process the chips will see during production.

Experience with multiple dielectric layer filters shows good uniformity and control of cutoff. As shown in Figure 1-8, the percentage range in transmission uniformity was approximately 2% or less over the window at 250 nm to 450 nm except near the cutoff wavelength. There the measured range was 5%; however, the measurement calibration was only accurate to ± 2 nm, which makes this value of uniformity a possible artifact of the transmission measurements.

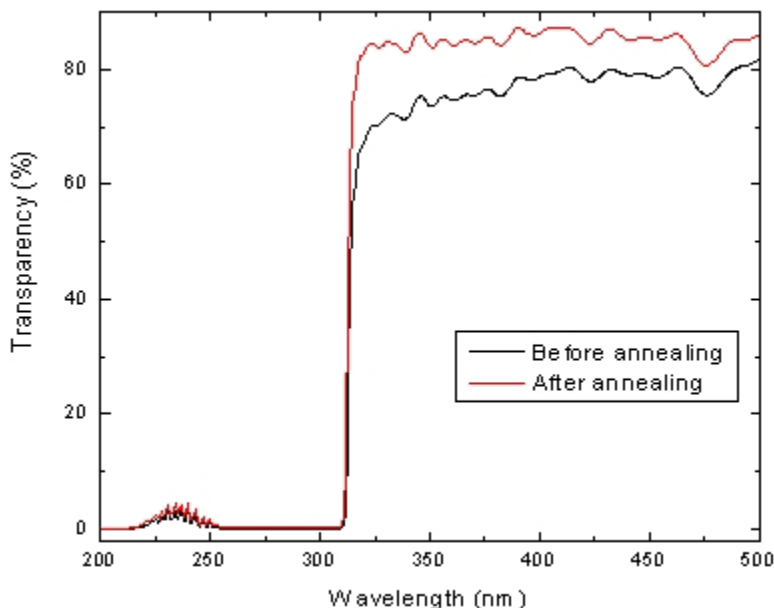


Figure 1-8. Filter evaluation before and after annealing.

In Figure 1-8, an improvement in the cutoff of the filter is observed after the annealing treatment. This phenomenon is likely due to the fact that the films are oxygen deficient after deposition, and an annealing treatment in air provides some oxygenation of the thin films, which has the effect of bringing the filter materials closer to stoichiometric.

The filter material was evaluated to determine any possible changes that might occur during diode fabrication and packaging. As shown in Figure 1-9, any increase in range or non-uniformity in percentage transmission at cutoff should not affect the sensor's performance. In addition, the chip package is filled with dry nitrogen so the possibility of oxygenation during sensor operating life is remote.

Final Report

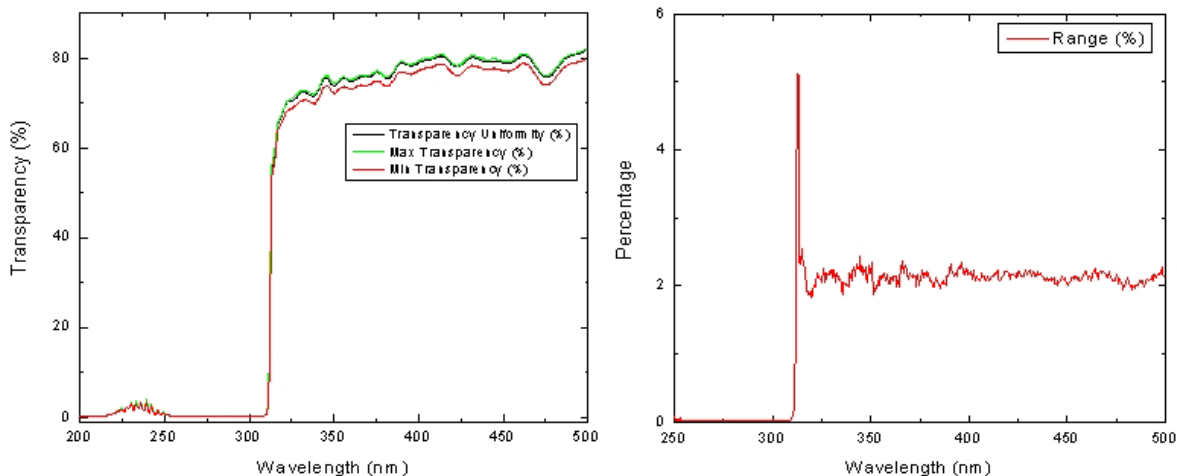


Figure 1-9. Filter transmission characteristics before and after annealing. At left, the filter uniformity, and at right, the range at each wavelength.

1.4.3 The SiC Dual Diode

The purpose of the dual diode design is to provide the capability of detecting light from two different spectral ranges for the implementation of a simple two-zone spectrometer. In this case, one zone collects light over the entire range of diode sensitivity from ≈ 200 to 400 nm, and the other zone collects light over a portion of this range. An optical long-pass filter defines the lower cutoff wavelength of the second zone, and the specific cutoff wavelength is chosen so that the UV emission spectrum from a combustion flame is divided into two portions.

1.4.3.1 Dual Diode Design Considerations

The dual diode is a new type of photodiode device chip that combines the functions of the filtered and unfiltered receptors. The design of this chip needed to satisfy both electrical and optical requirements. Since the original SiC flame sensor (FTS01) was already in production, it was decided that the same stainless steel housing and optics should be used. Because the new chip had to be compatible with the photodiode package, the chip size had to be between 1 and 2 mm². The fabrication masks included chip sizes of 1, 1.5, and 2 mm².

The first generation dual diode flame temperature sensor chip was designed to satisfy a number of critical requirements: tolerance to misalignment of the incident beam of light, good electrical and optical isolation between the zones, equal active area of the individual zones, and sharp optical filter cutoff at the desired wavelength. Figure 1-10 shows the interdigitated design of the FTS chip designed to satisfy those requirements. One zone contains a filtered diode; the other contains an unfiltered diode.

Final Report

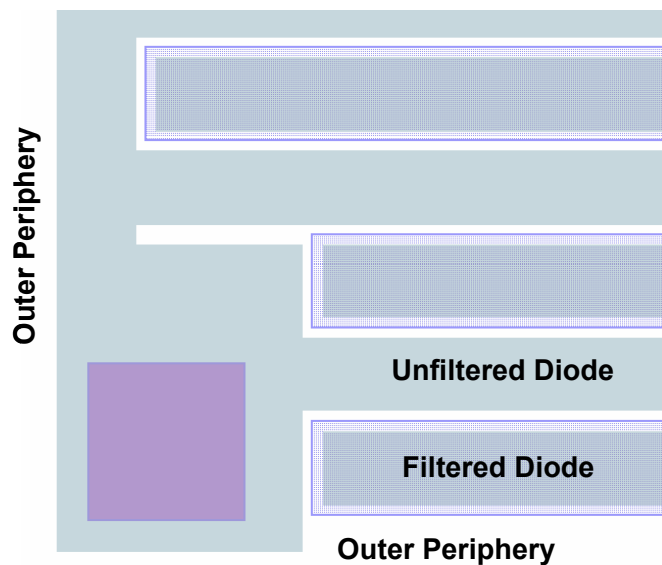


Figure 1-10. Top view of the FTS01 dual diode layout showing both filtered and unfiltered zones.

The interdigitated layout gives this design tolerance to central beam alignment. A trench that extends through the top n+ layer into the p- layer isolates the two zones. In this design, the separation distance between adjacent zones is an important factor. This separation distance must be larger than the minority carrier diffusion length to prevent electrical cross talk between the zones. Cross talk is generally defined as the unwanted interference between separate components within a device. For example, cross talk could be any electrical signal in the filtered photodiode resulting from leakage or noise in the unfiltered diode. The trench that isolates adjacent diode zones is 20 μm ; the minority carrier diffusion length, using optical responsivity measurements, is on the order of 2 μm (Brown, Downey et al. 1991). Determination of the diffusion length did not depend on any assumptions about carrier lifetime and mobility because it is based on matching the long-wavelength responsivity using well-established optical absorption coefficients.

The chip must meet the following requirements:

- Use the same converging lens as a standard flame sensor (i.e., 1-inch focal length defocused to 0.966 inch)
- Use a 0.8 mm² diameter spot to illuminate a 1 mm² chip (Gaussian profile)
- Be as large as might be needed (up to 4 mm²) for higher sensitivity
- Minimize cross talk
- Uniformly illuminate both zones of the dual diode

Prototype chip design involves a type of photodiode chip never made before. The design of this chip takes into account the size, optical characteristics, and semiconductor physics of SiC. The present plan is to use the same optics, chip package, and sensor housing as currently used in the production of Reuter Stokes flame detectors.

Final Report

There are two sources of cross talk: optical, which means photons that impinge on one diode somehow produce a signal in the other diode; and electrical, which means that the two diodes are not sufficiently isolated from each other. One way to insure that there is no cross talk at all is to eliminate every possibility of electrical cross talk and then insure that both sets of photons (filtered and unfiltered) do not produce contaminating signals in either diode.

Because the photon flux received by the two diodes needs to be as nearly equal as possible, the optical characteristics of the focusing lens need to be considered. It is assumed that the distribution of light across the diode is Gaussian (as shown in Figure 1-11) and that some misalignment of the chip to the center of the beam occurs during assembly. Both problems are resolved by using interdigitated optically sensitive diode fingers and a proper finger pitch, as shown in Figures 1-12 and 1-13.

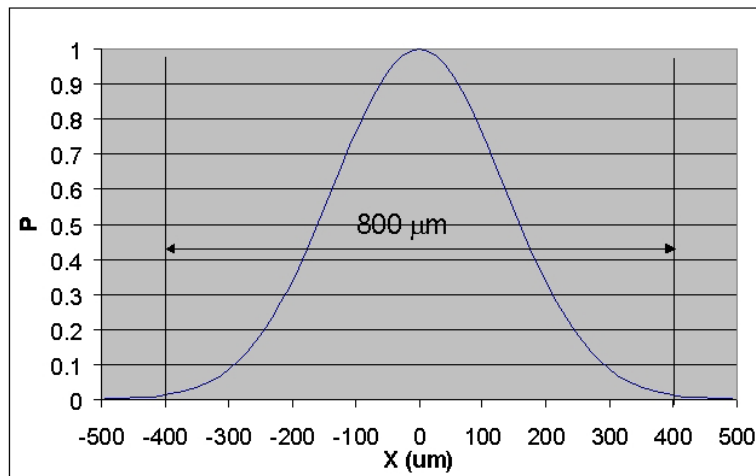


Figure 1-11. Optical beam intensity profile in relative units from edge to edge illuminating the present 1 mm² SiC chip in production sensor. This distribution has a Gaussian profile, with a standard deviation of 135 microns.

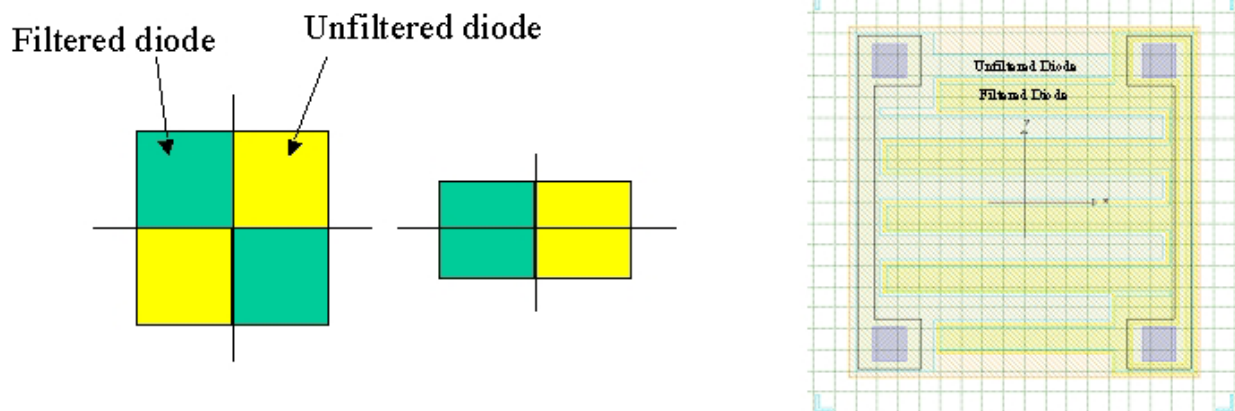


Figure 1-12. Basic chip design considerations. The interdigitated design should provide tolerance for the Gaussian illumination pattern and misalignment of the chip.

Final Report

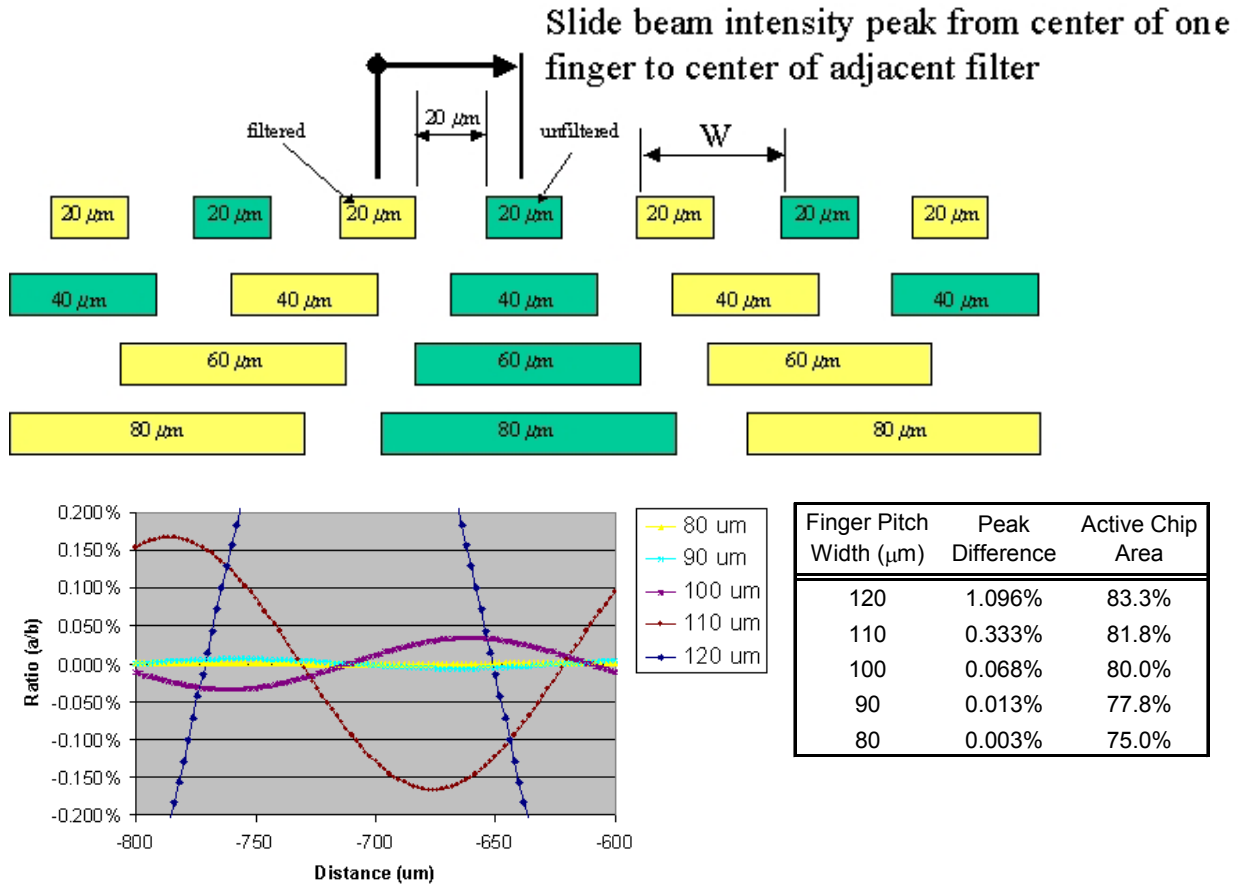


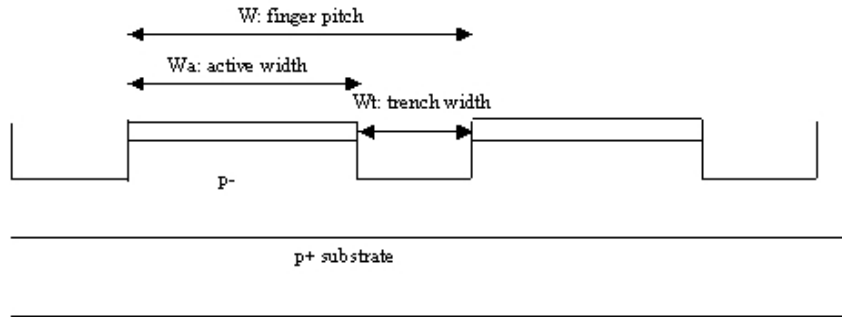
Figure 1-13. The effect of beam misalignment in multi-fingered SiC photodiodes.

Electrical and optical cross talk can be eliminated by taking into account the diffusion length of electrons in p-type material. As described in Section 1.4.3.1, this has been determined by other work to be about 2 microns. Therefore a finger spacing or mesa trench 20 microns wide, including a metal light blocking stripe (Mo), was deemed adequate.

Figure 1-14 summarizes results from 2D numerical simulations where the electron diffusion length was set at 2.2 μm . The table in the figure indicates the amount of photo-generated current that is detected in the unilluminated diode zone when 300 nm light is incident on the illuminated zone. The table at the left considers the case where the light blocker covers only half of the trench region; the table at the right considers the case when light is not allowed to illuminate any of the trench. With a 5- μm -wide trench, 0.61% of the generated photo current spills over into the adjacent unilluminated zone. In the limiting case of a 20- μm trench and 100% of the trench covered by a light blocker, only 0.004% (<1/10,000) of the photo current from the illuminated zone reached the unilluminated zone thereby essentially eliminating cross talk.

The misalignment issue was modeled so that optimum finger pitch could be determined. Peak difference needs to be minimized without markedly decreasing the optically active area of the chip.

Final Report



Illuminated to midpoint of trench

Trench Width Wt (μm)	W=50 μm	W=100 μm
5	1.20%	0.61%
10	1.30%	0.61%

Illuminated only to edge of trench

Trench Width Wt (μm)	W=50 μm	W=100 μm
5	0.27%	0.13%
10	0.09%	0.04%
20		0.004%

Wavelength=300 nm
 Electron diffusion length=2.2 μm
 Lifetime=4.7 ns

Figure 1-14. An optical cross talk simulation.

Optically generated electrons from the alternate filtered and unfiltered fingers should not be allowed to sense electrons generated in an adjacent finger. Because the diffusion length of electrons is quite short in SiC material, design of such a dual diode chip is feasible. Therefore a finger pitch of 60 or 90 μm with 20 μm spacing (trench width) is practical.

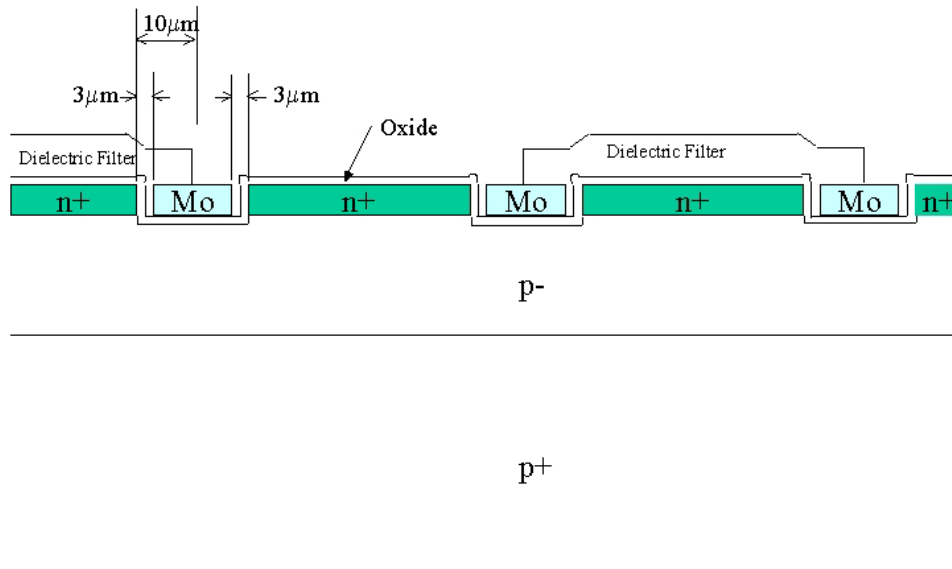


Figure 1-15. Cross section zone of the SiC dual diode showing the filtered and unfiltered fingers and a Mo stripe in the mesa trenches that is required to optically isolate adjacent fingers.

Final Report

The electrical and optical tests that were performed are listed in Table 1-1. Design variations included in the mask set are shown in Figures 1-16 and 1-17.

Table 1-1. Dual Diode Test Plan

Electrical Testing	Optical Testing
Same as Standard Detector	Spectral Characterization
- forward conduction	- determine filter characteristic
- reverse leakage	Scanning beam photo response
- leakage at low reverse bias	
diode isolation	- determine effect of beam misalignment

1x1_dual-diode_A
Finger Pitch: 90 μm

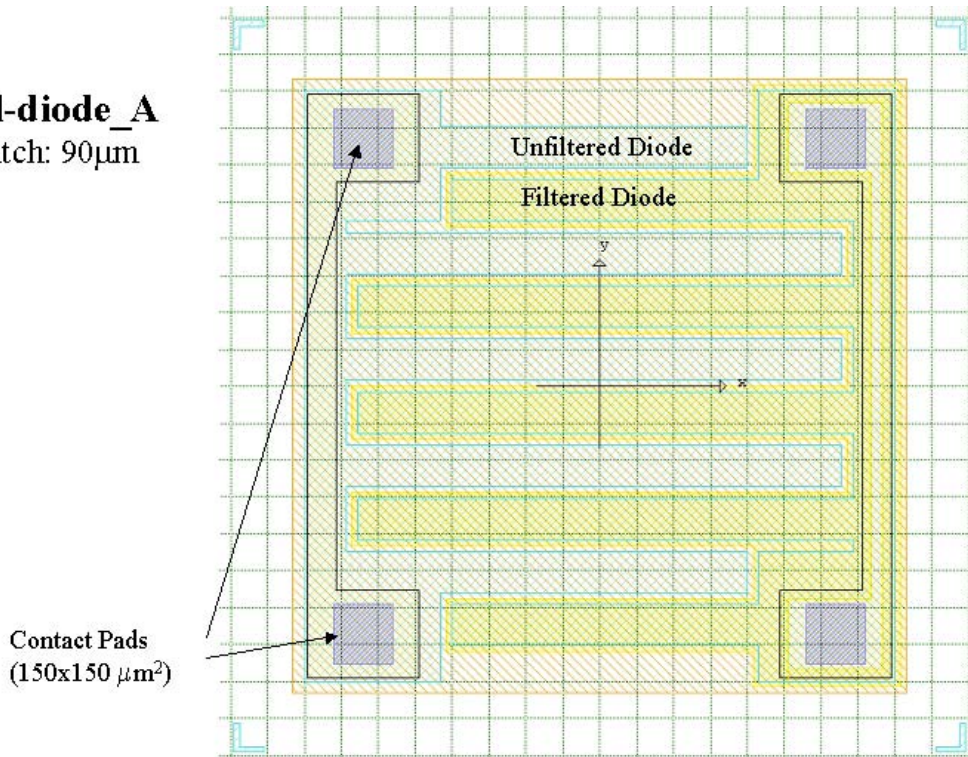
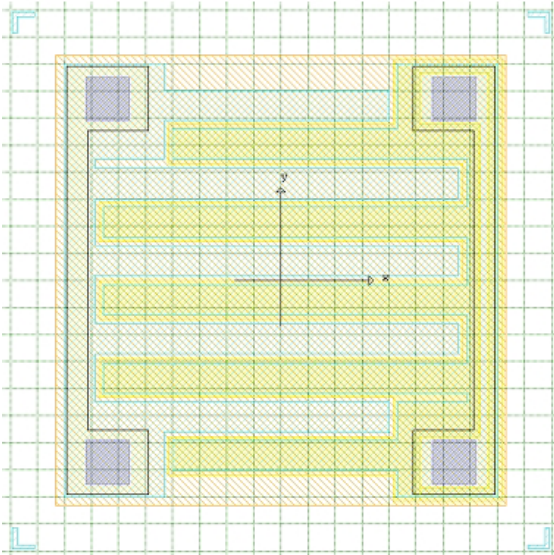


Figure 1-16. Top view of the dual diode.

Final Report

1x1_dual-diode_A
Finger Pitch: 90 μm
70 μm finger 20 μm trench



1x1_dual-diode_B
Finger Pitch: 20 μm
40 μm finger 20 μm trench

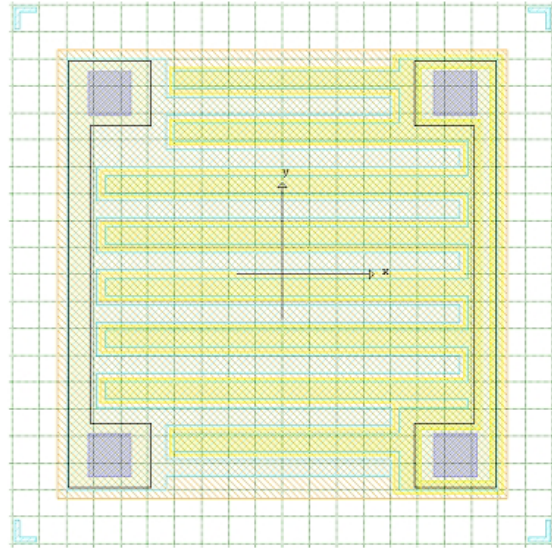


Figure 1-17. 1-mm² dual diodes with different finger widths and pitches.

1.4.3.2 Dual Diode Test Results (FTS01) and Fault Verification Experiments

The measurements made to investigate the probability of optical and electrical cross talk found in the first generation of the flame temperature sensor dual diode chip (FTS01) are summarized in Section 1.4.3.2.1. The results presented are from a 2-inch diameter, 6H-SiC, p+ substrate wafer and standard photodiode epitaxial layers from Cree Inc.

1.4.3.2.1 Optical Test Results

The responsivity of a standard SiC photodiode made with p+ substrates and p- and n+ epitaxial layers is shown in Figure 1-18.

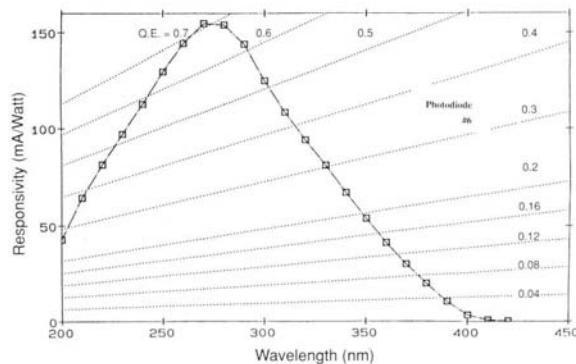


Figure 1-18. Standard SiC photodiode fabricated by GE for Reuter Stokes flame detectors.

Final Report

The responsivity of filtered and unfiltered SiC photodiodes made for this project is shown in Figure 1-19. The filtered photodiode's stop band region shows about 20% and 30% responsivity; thereby contradicting the theoretical calculations of Figures 1-4 and 1-7 and the experimental results in Figures 1-5, 1-6, and 1-7. This deviation from expected behavior would produce a ratio higher than expected and a reduction in sensitivity to flame temperature changes. This deviation was thought to be generated by photo response caused by light hitting the edges of the chip not covered by the filter.

To determine whether uncovered filter edges were the cause of the problem, a spot beam test was initially proposed, in which a beam of light would be focused entirely on the active area of the device, with very little or no light hitting the mesa trench or its edges. This test was performed to examine the amount of photocurrent resulting from photocurrent generation at or near the mesa edges, which is unwanted, as the filter does not extend into this region. Initial tests were performed using this method; however, the results were unclear probably because of a diffraction pattern produced by the small pinhole.

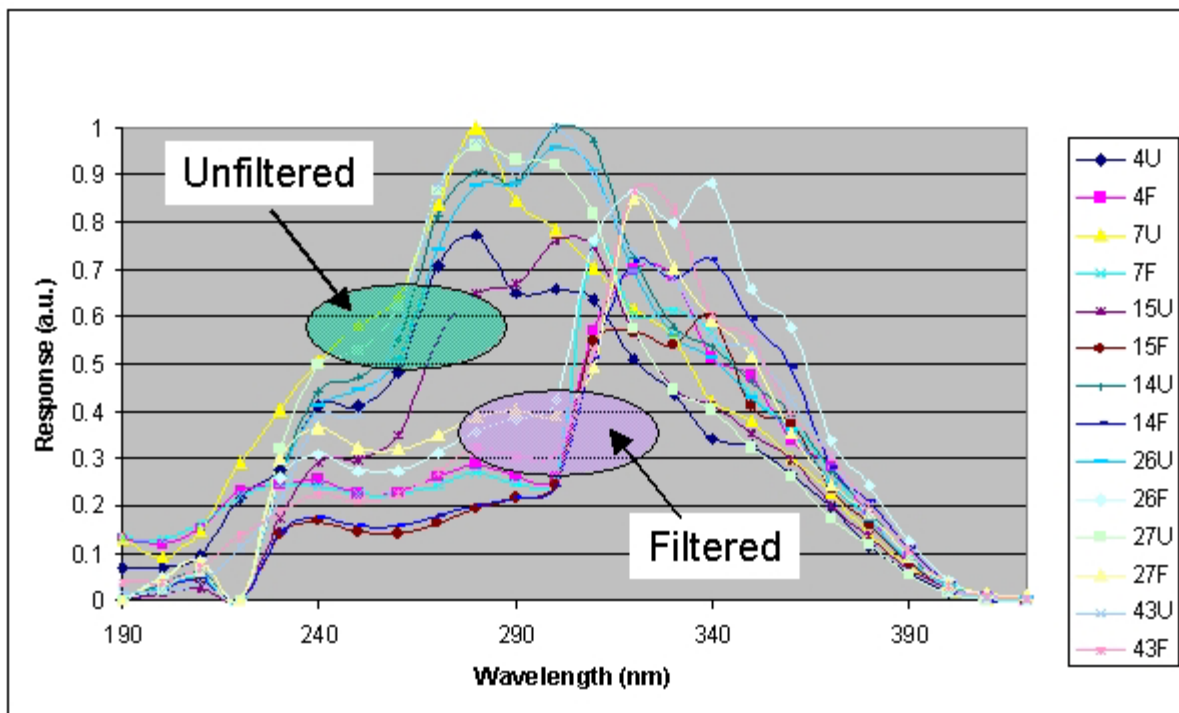


Figure 1-19. Spectral responsivity of various dual diodes.

A better approach was to block all the curf and mesa edges on the chip keeping a small circle over the active area open, as shown in Figure 1-20. In this test, only the central active area was exposed to light.

Final Report



Figure 1-20. Most of the chip at the left is covered with epoxy, with the center circle over the active area. At the right is an uncovered chip, shown for comparison.

The responsivity curves before and after the epoxy coating have all been normalized to remove the effect of area difference resulting from the epoxy coverage. Both curves were normalized to the one with the greater peak, thus keeping the set consistent within each device for the filtered and unfiltered halves

The results of these measurements are very encouraging. The normalized spectral responsivities of PD65 are shown in Figure 1-21. Here, the two curves show the measurement without epoxy and the measurement after the epoxy was applied so that only the active area was left open. As the PD65 device has no fingers and is covered completely with the filter, it is reasonable to conclude that the difference in response between 220 and ~300 nm is due to the response from the edge of the mesa and the region extending a short distance beyond. When this edge area is completely covered, the stop band response is greatly reduced, forcing the behavior of the diode more closely to the calculated response.

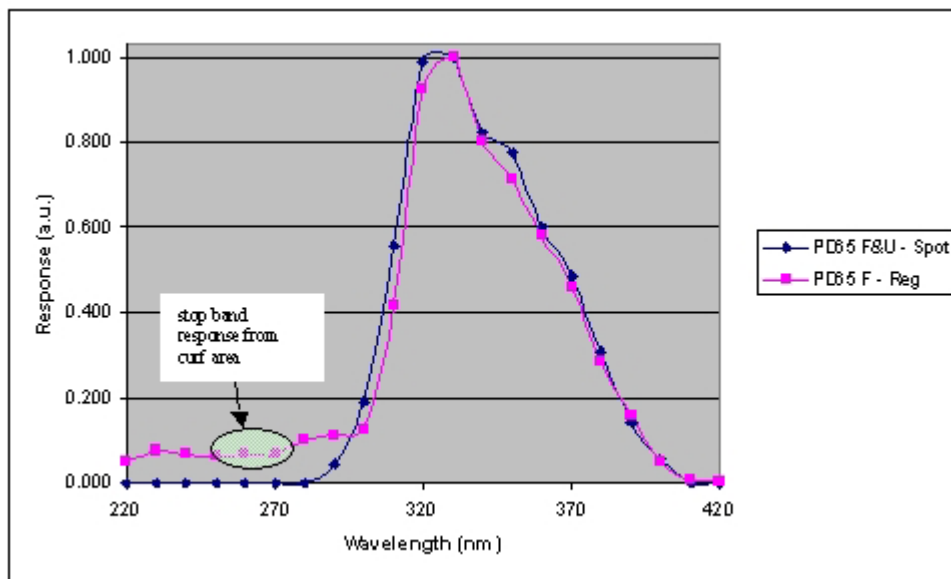


Figure 1-21. Normalized photoresponse of PD65, before and after the application of epoxy in areas over the curf.

Final Report

The normalized responsivities of PD61, all filter, with fingers, was measured; the results are shown in Figure 1-22. In a similar fashion to PD65, the effect of cross talk is likely to be small because the two devices are the same optically, as shown by the overlap of the pink and blue curves (“unfiltered” and “filtered”).

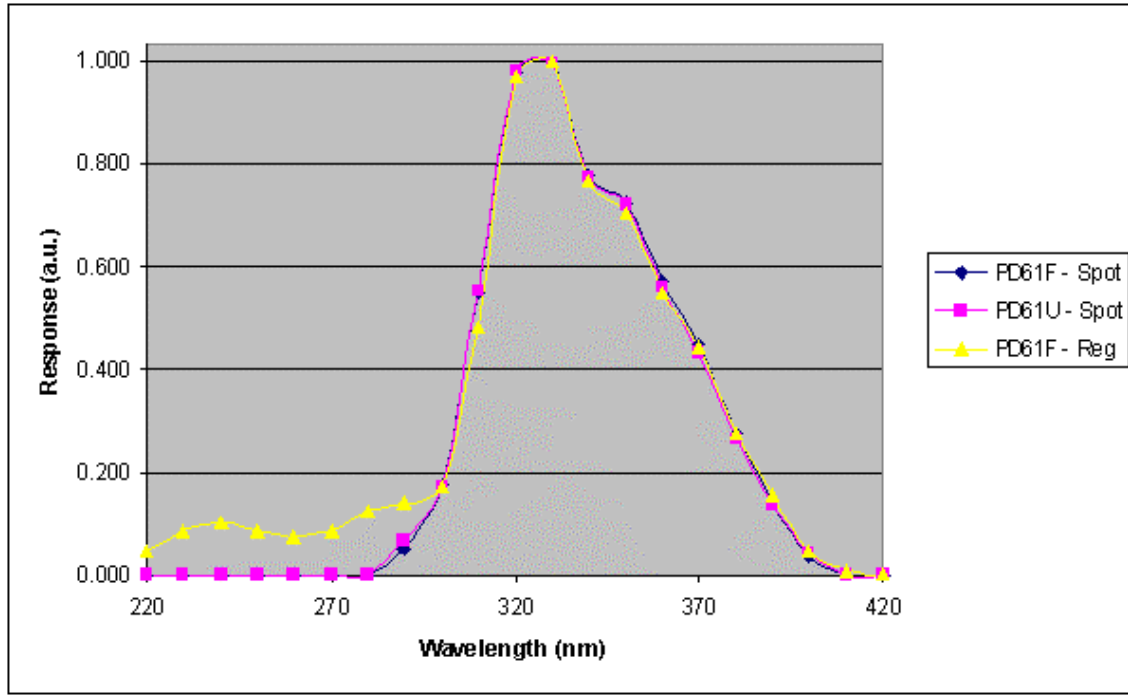


Figure 1-22. Normalized photoresponse of a photodiode with fingers, PD61, that is completely covered by a filter before and after the application of epoxy in areas over the curf.

As with PD65, the stop band response from 220 up to ~ 285 nm is almost completely eliminated and is reduced up to ~ 300 nm. Above 300 nm, the curves are in good agreement. Reasonable speculation here again says that the difference in responses from 220 to ~ 285 nm is coming largely, if not completely, from responses being generated at the edges and perhaps from 5 to 6 μm beyond the edge.

In the area between 300 and 315 nm, there is a high degree of sensitivity that remains unaccounted for. One possible explanation is the variability in filter thickness resulting from the finger etching. This seems unlikely, however, because PD65, in which there are no fingers, has a similar response. Another explanation may be that the filter transmission curve was somehow modified either by a thin residue on the surface or by slightly etching the surface through acid/solvent treatments during diode fabrication.

1.4.3.2.2 Electrical Test Results

Cross talk is defined as an unwanted signal that gets coupled from one isolated region of a device to another. In the dual photodiode there are three isolated regions: the outer periphery of the device, the unfiltered diode region and the filtered diode region as shown in Figure 1-10. Cross

Final Report

talk may arise due to spillover of either electrical or optical signals. Optical cross talk occurs when unwanted light reaches an active region of the device producing added photocurrent beyond that caused by desired incident light. Electrical cross talk occurs when an unwanted electrical current reaches an active region from another region that is not sufficiently isolated. Separate tests have been made to measure both forms of cross talk. This zone focuses on the electrical cross talk measurements made on packaged dual photodiodes. The test pass criteria and a tabulation of test results of packaged diodes are given in Appendix Section 1B.

1.4.3.2.3 Isolation Tests

As part of the routine electrical tests during autoprobing, a series of isolation tests were run to check the isolation between the filtered and unfiltered diodes. Figure 1-23 shows the configuration used for isolation testing. With this configuration, the measurement can be made in two directions; namely, with the unfiltered diode in reverse bias and the other diode forward biased (U-F) or with the filtered diode in reverse bias and the other diode forward biased (F-U).

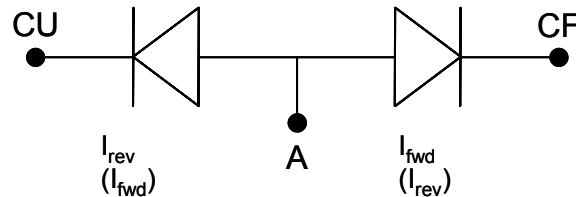


Figure 1-23. Isolation test configuration. For this test, the anode (A) is floating and a voltage is applied between the unfiltered cathode (CU) and the filtered cathode (CF).

Table 1-2 is a summary of isolation test results for several diodes at two different voltages and in both directions (U-F and F-U). At 0.5 V and 10 V the corresponding current limits are 2 pA and 1 nA respectively. These diodes failed the isolation test because the isolation currents are higher than the yield limit. A number of factors could contribute to these large isolation currents as will be discussed in Sections 1.4.3.2.4 and 1.4.3.2.5.

Table 1-2. Isolation Tests between Unfiltered (U) and Filtered (F) Diodes

Device #	Name	U-F isolation current @ 0.5V	F-U isolation current @ 0.5V	U-F isolation current @ 10V	F-U isolation current @ 10V
	Yield Criteria	<1E-9	<1E-9	<2E-12	<2E-12
4	1X1X90	1.13E-06	3.59E-12	5.14E-08	5.22E-08
7	1X1X60	3.63E-06	3.95E-12	2.38E-07	1.50E-07
14	1.5X1.5X90	1.93E-06	8.59E-12	9.11E-08	1.02E-07
15	1.5X1.5X90	2.33E-07	5.10E-14	1.58E-08	2.82E-08
26	1.5X1.5X60	6.96E-07	3.87E-12	2.66E-08	1.57E-08
27	1.5X1.5X60	2.06E-06	1.32E-11	9.04E-08	1.02E-07
43	2X2X60	n/m	n/m	n/m	n/m

1.4.3.2.4 Reverse Leakage Current Tests

The reverse leakage current from both filtered and unfiltered diodes was systematically measured at voltages up to 10 V reverse bias. Figure 1-24 shows the measurement configuration where the filtered diode is measured between CF and A with CU floating, and the unfiltered diode is

Final Report

measured between CU and A with CF floating. Table 1-3 lists the reverse leakage currents for the same subset of diodes at voltages of 0.5 V and 10 V reverse bias where the current limits are the same as those used for the isolation tests. For these diodes, leakage currents were well below the current limit at both 0.5 V and 10 V indicating that reverse leakage current is not a source of poor isolation between diodes.

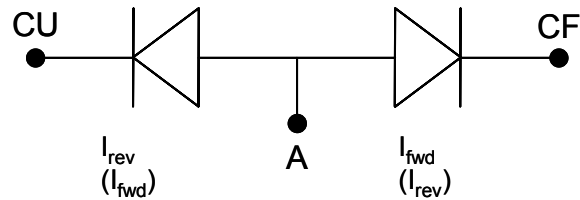


Figure 1-24. Reverse leakage current test configuration where measurement is made between the anode (A) and either cathode (CF or CU) with the third terminal floating.

Table 1-3. Reverse Leakage Current for Unfiltered (U) and Filtered (F) Diodes

Device #	Name	U dark current @ 0.5V	F dark current at 0.5 V	U rev leakage current @ 10 V	F rev leakage current @ 10 V
	Yield Criteria	<1E-9	<1E-9	<2E-12	<2E-12
4	1X1X90	6.00E-14	8.90E-14	2.60E-10	2.10E-12
7	1X1X60	8.50E-14	1.50E-13	2.00E-10	2.40E-10
14	1.5X1.5X90	1.20E-13	1.30E-13	4.00E-10	3.00E-10
15	1.5X1.5X90	2.20E-13	2.60E-13	6.20E-10	4.90E-10
26	1.5X1.5X60	1.50E-13	1.80E-13	5.40E-10	1.00E-11
27	1.5X1.5X60	1.00E-13	1.60E-13	4.80E-10	1.90E-10
43	2X2X60	1.30E-13	1.40E-13	1.00E-15	n/m

1.4.3.2.5 Parasitic NPN Bipolar Transistor Tests

Another possible source of cross talk is the parasitic negative-positive-negative (NPN) transistor involving the cathodes of adjacent filtered and unfiltered diodes, serving as emitter and collector, and the common anode serving as the base, as shown in Figure 1-25. Current between cathodes can arise by the transport of minority carriers across the p- base layer originating from the forward biased emitter and reaching the zero or reverse biased collector. Since the dual diode is electrically symmetrical, either the unfiltered cathode or the filtered cathode can serve as the emitter. When the unfiltered diode is forward biased, electrons injected into the base will diffuse through the p- base layer a distance on the order of the electron diffusion length. If the diffusion length in the p- layer is sufficiently large, electrons may reach the adjacent cathode (collector) before recombining and giving rise to a parasitic current between the cathodes. If the base width is significantly large compared with the diffusion length, however, base transport will be negligible, giving rise to negligible gain of the parasitic NPN transistor.

Final Report

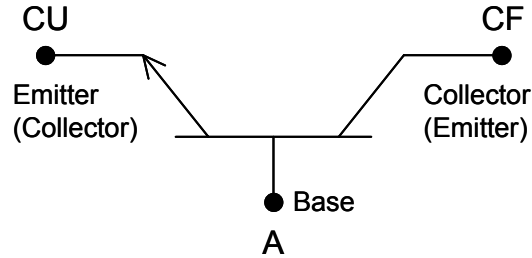


Figure 1-25. Parasitic NPN bipolar transistor test where the anode serves as the base, either the unfiltered cathode or the filtered cathode serves as the emitter, and the third terminal serves as the collector.

The diffusion length in a semiconductor is related to the minority carrier lifetime, which is typically an unspecified parameter. For lightly doped layers, the minority carrier lifetime is a function of the concentration and energy levels of traps present in the material. Minority carrier lifetime is reduced in heavily doped layers where the majority carrier concentration is large and electron-hole recombination can occur more readily. The electron diffusion length is related to lifetime (τ_n) by the expression $L_n = (D_n\tau_n)^{1/2}$, where D_n is the electron diffusion constant. Figure 1-26 shows the electron diffusion length as a function of lifetime for the 6H-SiC p-type epitaxial layer found in the dual diode structure, with an assumed electron mobility of $300 \text{ cm}^2/\text{Vsec}$. The minority carrier lifetime in lightly doped n-type material has been measured for both 4H and 6H-SiC and exhibits an increasing trend with epitaxial layer thickness (Kordina et al. 1996). For 4H-SiC layers, a $24 \text{ }\mu\text{m}$ n-type layer gave a hole lifetime of $0.44 \text{ }\mu\text{s}$ while a $60 \text{ }\mu\text{m}$ layer yielded a lifetime $2 \text{ }\mu\text{s}$. A $24 \text{ }\mu\text{m}$ n-type epitaxial layer on 6H-SiC gave a hole lifetime of $0.11 \text{ }\mu\text{s}$, 4 times smaller than the lifetime of 4H-SiC. The trend of longer lifetime with a thicker epitaxial layer could be due to the eventual dissipation of lifetime-limiting defects originating at the epitaxial-layer/substrate interface as the epitaxial layer thickness increases. A similar trend for electron lifetime in p-type material is assumed. The p-type epitaxial layer in the GE GRC SiC photodiodes is only 5 or $6 \text{ }\mu\text{m}$ thick.

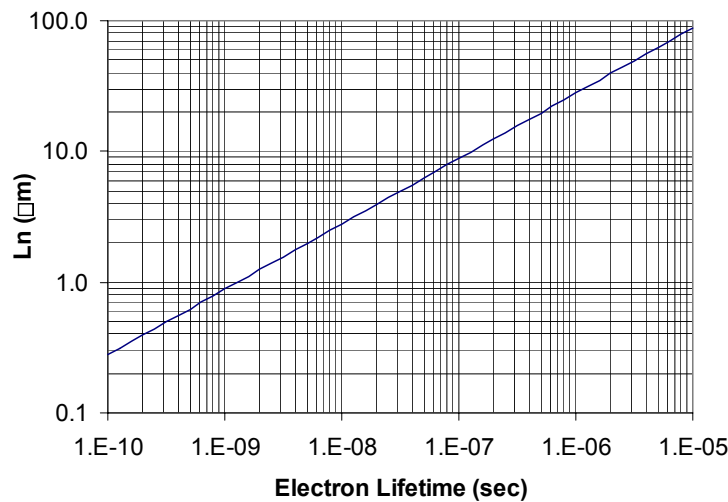


Figure 1-26. Electron diffusion length versus electron lifetime for 6H-SiC, p-type epitaxial layer, $N_a=1e16 \text{ cm}^{-3}$, $\mu_n=300 \text{ cm}^2/\text{Vsec}$.

Final Report

Common-emitter transistor gain measurements were made to determine an upper bound for the electron diffusion length in these dual diodes. These measurements were made on several packaged dual diodes with the measurement configuration shown in Figure 1-27. The collector bias of 6 V was used to ensure that the collector-base junction never becomes forward biased.

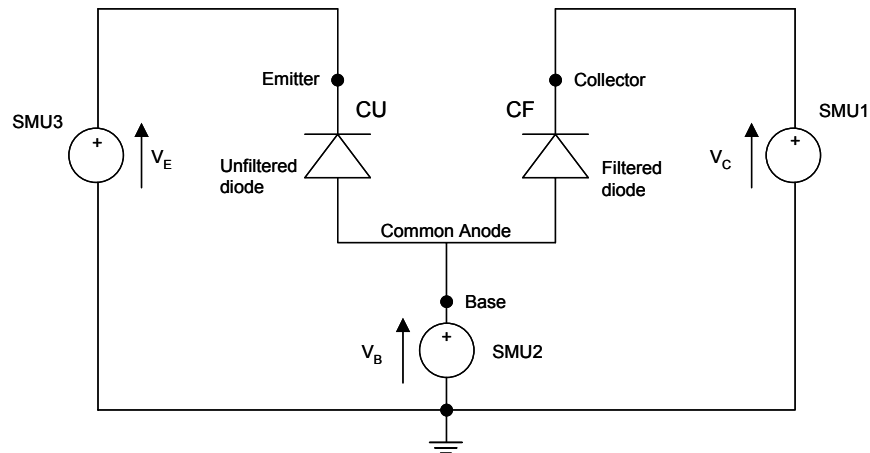


Figure 1-27. Configuration used to measure bipolar transistor gain.

Using the configuration shown in Figure 1-27, Gummel plots were made for several packaged dual diodes. One example is shown in Figure 1-28. For this device, it is evident that the current gain is very low since the collector current is always much less than the base current. The common-emitter current gain (β) is determined as the ratio of collector current to base current and the common-base current gain (α) is determined as $\alpha = \beta / (1 + \beta)$.

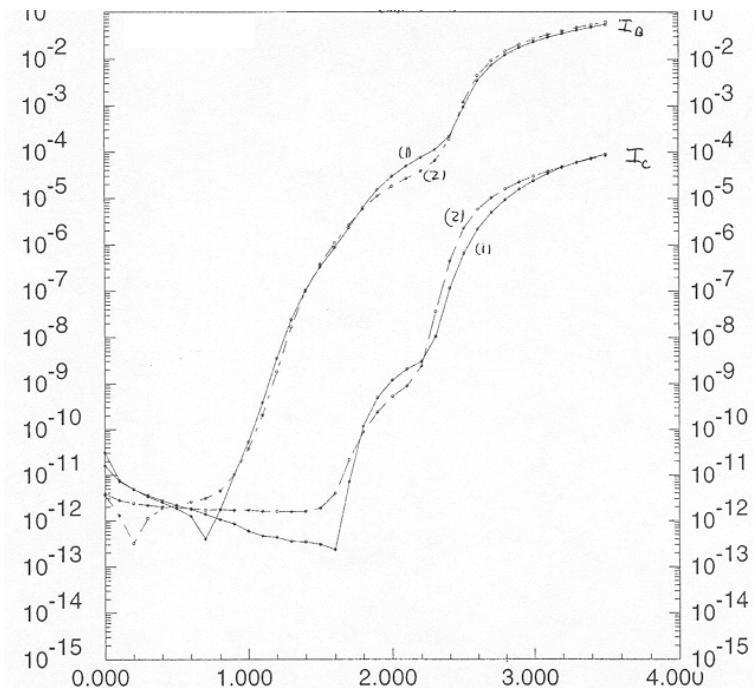


Figure 1-28. Gummel plot of a packaged dual photodiode, dark conditions. The base current is shown on the left vertical axis, the collector current on the right vertical axis, and the base voltage is shown by the horizontal axis on the bottom.

Final Report

An estimate of the diffusion length can be made by assuming that the transistor is base-transport limited. The large carrier concentration ratio from emitter to base (greater than 10^3) makes this assumption reasonably accurate

The base transport factor, α_t , is related to the base width (W_B) and electron diffusion length as:

$$\alpha_t = \frac{1}{\cosh(W_B / L_B)}$$

For this dual diode structure, $W_B = 20 \mu\text{m}$. An estimate for the diffusion length can be made using this expression and the approximation $\alpha \approx \alpha_t$. The current gain was measured in both the forward (1) and reverse (2) directions. The forward direction defines the unfiltered cathode as the emitter, and the reverse direction defines the filtered cathode as the emitter. Table 1-4 gives the measurement results for four of the packaged diodes where the gain is extracted at a base voltage of 2.6 V. These diodes were chosen because they exhibited good isolation. As may be seen from the table, the common-base current gain was on the order of 10^{-3} and the corresponding electron diffusion length ranges from 2.4 to 2.8 μm . These values correspond to electron lifetimes ranging from 7.5 to 10 ns. For an indirect band gap semiconductor, this range of lifetime values for a lightly doped p-type layer is relatively short, suggesting the presence of high levels of trapping centers in the material.

Table 1-4. Transistor Gain Measurements for Several Packaged Dual Photodiodes

Device	I_{c_1} (A)	I_{b_1} (A)	α_1	L_n (μm)	I_{c_2} (A)	I_{b_2} (A)	α_2	L_n (μm)
PD01	3.0E-06	2.5E-03	1.2E-03	2.7	5.0E-06	4.0E-03	1.2E-03	2.7
PD02	3.0E-06	3.0E-03	1.0E-03	2.6	5.0E-06	4.0E-03	1.2E-03	2.7
PD09	2.0E-06	3.5E-03	5.7E-04	2.5	5.0E-06	4.0E-03	1.2E-03	2.7
PD10	1.5E-06	3.0E-03	5.0E-04	2.4	6.0E-06	4.0E-03	1.5E-03	2.8

Some devices exhibited poor isolation between filtered and unfiltered cathodes. The Gummel plot of Figure 1-29 shows results from a device where I_c and I_b are not parallel where the collector current is large near zero base bias and rises only gradually with I_b . This larger than expected collector current could be due to a surface conductance channel that facilitates the conduction path between adjacent cathodes. Leakage current from each individual diode is on the order of 10^{-10} A or less over the range of 0 to 10 V (as shown in Figure 1-30) indicating that the large collector current does not originate from diode leakage.

Final Report

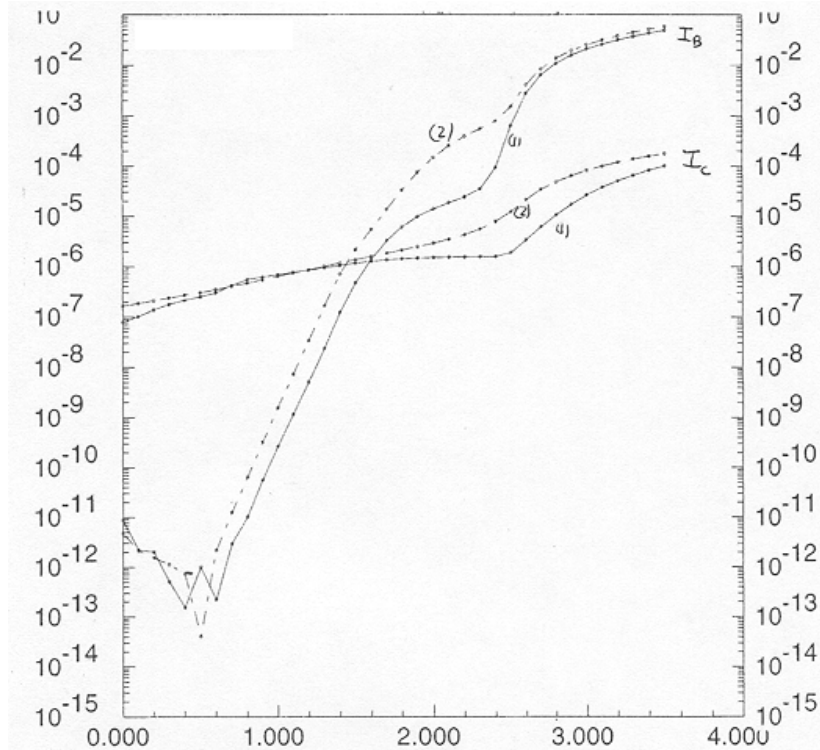


Figure 1-29. Gummel plot of a packaged dual photodiode showing significant conductance between cathode fingers. The base current is shown on the left vertical axis, the collector current on the right vertical axis, and the base voltage is shown by the horizontal axis on the bottom.

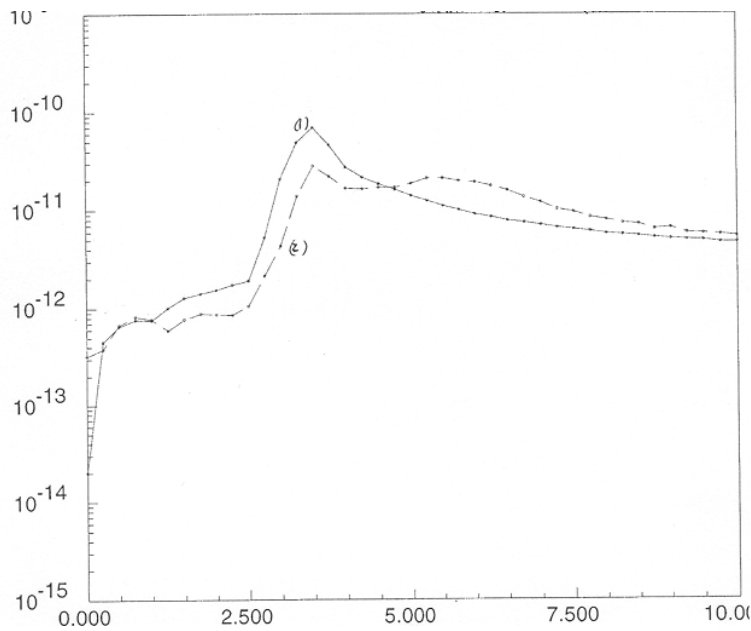


Figure 1-30. Leakage current of individual filtered and unfiltered diodes (dark conditions). The current is shown on the vertical axis, and the voltage is shown on the horizontal axis on the bottom.

Final Report

1.4.3.3 Discussion of FTS01 Dual Diode Tests

Optical responsivity measurements indicated that there was considerable responsivity in the stop band of the filtered diode. Experiments showed that optical responsivity can occur from the mesa edges or nearby, in the p- region just beyond this edge.

The optical filter that was used effectively blocks higher energy light. Measurements show that 84% of light is transmitted at 320 nm while less than 0.01% is transmitted at 300 nm. These optical transmission measurements were made on sapphire test substrates deposited concurrently with the device wafers.

The unfiltered diodes showed response extending from 200 to 400 nm, similar to conventional UV photodiodes used in the Reuter Stokes flame detector. Ideally, the filtered diode would have the same response as the unfiltered diode above the cutoff and then have zero response at shorter wavelengths. The filtered diodes measured in Figure 1-20 show a reduction in response below the filter cutoff but not an elimination of response. This stop-band photo response could come from a number of sources, either optical or electrical. Experiments showed that stop band optical responsivity can occur because the filter does not cover the edges of the mesa.

Electrical cross talk measurements indicated that in some cases electrical isolation was insufficient. Measurements of parasitic bipolar gain showed that the electron diffusion length with lightly doped p-type SiC is between 2 and 3 μm which verified the original design parameter of 20 μm for dual diode finger spacing. Because bipolar gain was very low, the most likely candidate for lack of isolation is an n-type surface channel over the lightly doped p type regions which connects the n+ regions together.

1.4.4 The Fiber Optic Spectrometer

The fiber optic spectrometer uses a fiber optic cable to collect the light and transmit it to a diffraction grating. The dispersed light impinges on a Si charge coupled device (CCD) coated with a phosphor to produce electrical outputs into the UV region as a function of wavelength. The resolution is not as high as would be attained with the very narrow slit spectrometer that would be required to resolve individual spectral lines, but it is perfectly adequate to trace the shape of the OH band. This device requires integration times of 1 to 3 seconds. It also requires a relatively large photon intensity to produce good signal-to-noise. The spectrometer gives 2048 pts between 179 and 868 nm. The distribution of points varies somewhat over this wavelength range. The spectrometer, including the fiber optic cable, may be calibrated over its effective range of 200 to 1100 nm, which then gives true relative intensity versus wavelength.

Complete flexibility is possible with this method because the integrated intensity over various groups of wavelengths within the OH band can be calculated easily from the spectrum. For example, the ratio could be the integrated intensity of the long-wavelength region, which changes rapidly with temperature, divided by the short-wavelength region, which changes only slightly with temperature.

1.5 THE COMBUSTION PROCESS AND CONCEPT UNIQUENESS

The dry low NO_x (DLN) combustion flames used in GE gas turbines use swirler type nozzles or flame holders to premix the fuel and air before combustion occurs. As the combustion process proceeds, the plasma temperature increases rapidly until it reaches a maximum. OH molecules—

Final Report

as well as CN, CH, CO, NO molecules, and others—are a product of the combustion process. These molecules are in an excited state and produce characteristic photon emission spectra.

When the combustion process is completed and the maximum temperature has been achieved, these OH molecules cease to exist. When the intensity of the OH emission band is measured by using a SiC photodiode and a very small aperture is used to determine OH band intensity as a function of axial position, the intensity is observed to be low initially, then it climbs to a peak and rapidly diminishes.

The OH photon intensity is a function of the number of OH molecules produced by the combustion process at any point along that axial line, not the temperature of the plasma, which reaches its maximum very soon after the OH emission intensity dies. In order to determine OH band shape, which is a direct indication of temperature, a ratio of two intensities is required since a ratio cancels out the number of molecules in the volume of plasma within the field of view.

The spectrum “seen” by the detector is a confluence or average of the spectral intensities produced by all the molecules within the field of view. The intensity for a particular band of wavelengths can therefore be written as:

$$I(T) = N \int_{\lambda_1}^{\lambda_2} B(\lambda, T) S(\lambda, T) d\lambda$$

where N is the number of molecules, B is the quantum mechanical form of the black body radiation law, and <S> is the distribution of line strengths that represents all the molecules. Therefore the ratio of two bands of the observed spectrum produced by the same group of molecules is :

$$R(T) = \frac{\int_{\lambda_2}^{\lambda_3} B(\lambda, T) S(\lambda, T) d\lambda}{\int_{\lambda_1}^{\lambda_3} B(\lambda, T) S(\lambda, T) d\lambda}$$

This ratio represents the emission intensity as a function of wavelength of a single average OH molecule within that volume. In other words, the ratio cancels out the fuel factor. The plasma temperature can then be determined from these ratios.

This method of taking ratios of two intensities composed of the integrated intensities in the long-wavelength region of the OH band divided by either the total integrated intensity over the entire band or by the integrated intensity of the short-wavelength region is unique in several respects.

Its uniqueness results from having the ratio represent the specific volumetric average temperature of all the molecules in the volume within the field of view. An integrated intensity as a function of wavelength before the ratio is taken represents the volumetric average. These ratios can then be directly and uniquely related to any number of well-known calibration methods. In the preferred case, this temperature has been the final or maximum combustion temperature determined by the combustible gas mixture or the concentration of unburned oxygen measured by the emission probe. For a hydrocarbon fuel these ratios are unique because they represent the specific volumetric spectral average of any type of spectral distribution within the field of view.

Another way of thinking about this phenomenon is to consider a different example. Visualize a number of tungsten filament lights in a room. For instance, there are two groups of ceiling lights. One group is composed of hot blue lights and the second group is cool red. A measurement of the spectral distribution of intensities on a table top would be a spectral average and a spectral representation of the light intensity produced by these two groups. If the ratio of the number of

Final Report

lighted lamps within these two groups is kept constant and more or fewer lamps in both groups are turned on or off, the total intensity changes but the shape of the spectrum does not. Intensity by itself tells nothing about the temperature of the light sources, but the shape of the black body spectrum does. If on the other hand more hot (blue) lights are now turned on and the number of cool (red) lights turned on remains the same, then the spectrum would shift towards the blue, still representing the average black body temperature of all the lights. It is important to recognize that the spectral intensity curve as a function of wavelength is already an average spectral intensity, and this spectrum is a representative of what might be called the single “average” light that can be used to determine the average temperature of all the filaments in all the lights.

Because the combustion zone is not in equilibrium, referring to the temperature of the zone is somewhat of a misnomer. All the molecules within this zone are in excited states and optical transitions between these states produce photons of various wavelengths. If one could “look into” the combustion zone, one would observe a random burning process composed of explosive pockets of burning gas. This random process produces flame intensity fluctuations. Measurements of flame intensity were made using a SiC flame detector and by taking thousands of samples over a time interval of a few seconds. These data plots show that the distribution in intensity is normal as shown in Figure 1-31.

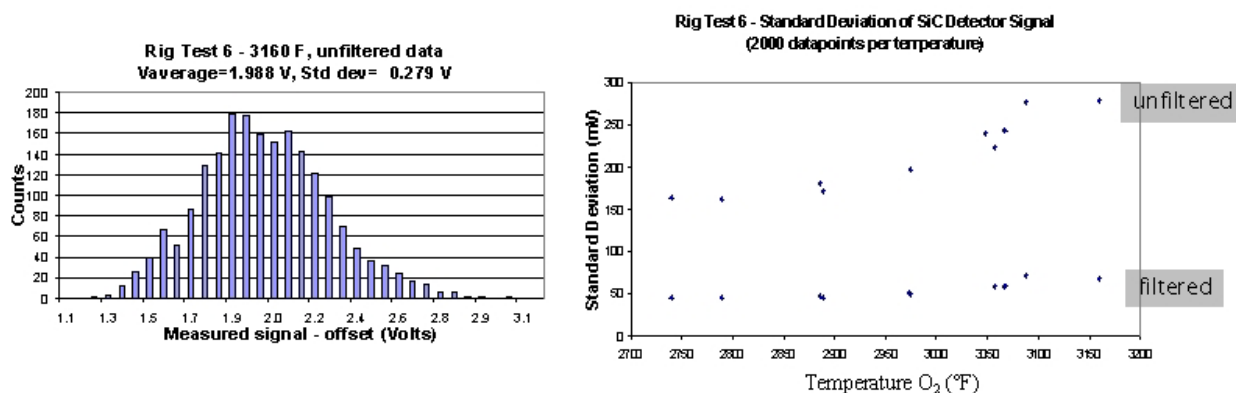


Figure 1-31. Data showing signal distribution at 3160°F flame temperature caused by flame emission fluctuations, and standard deviation of filtered and unfiltered signals versus temperature.

Time-averaging the signals shown in Figure 1-31 eliminates the problem of fast flame fluctuations so that good average intensity can be obtained for any given fuel and air combustion mixture.

1.6 EXPERIMENTAL

1.6.1 The Atmospheric Rig with LM6000 Premixing Flame Holder

A LM6000 premixing nozzle running at 1 atm was used for all the feasibility experiments. The first experiments used unheated air. The initial results were encouraging but they were not reproducible. There was no reproducibility during a single day or day to day. The sensitivity to flame temperature changes was found to be lower than that calculated using the LIFBASE computer code.

Final Report

Many faults with this combustor rig were soon identified. An extensive upgrade was required. One goal was to get agreement between flame temperature determinations made using air and fuel flow calculations and temperatures determined by measuring the amount of unburned O₂ in the exhaust. The use of heated air to extend the operating range to lower temperatures thereby avoiding lean blow out was considered.

Every effort was made to eliminate air leakage so as to be able to get the agreement between T_{Flow} and T_{O₂} as close as possible. Venturi meters were installed and a new gas analyzer was used to determine T_{O₂}. Before the experiment every day, the gas analyzer was calibrated using ambient air. The flame was enclosed in a rectangular quartz tube. This tube was repeatedly annealed to eliminate internal stress in order to minimize the potential for cracking. The flame could be moved up and down so that data could be obtained as a function of axial position.

1.6.1.1 Calibration of Revised Atmospheric LM6000 Premixed Combustor Flame

During the initial run the variation in temperature across the width of the burner was determined using a single point probe. The temperature variation was large, as may be seen in Figure 1-32. For all data presented in this report, standard natural gas was used as fuel. In other data, pure methane was used to compare the flame spectral output with natural gas, and minimal differences were noted.

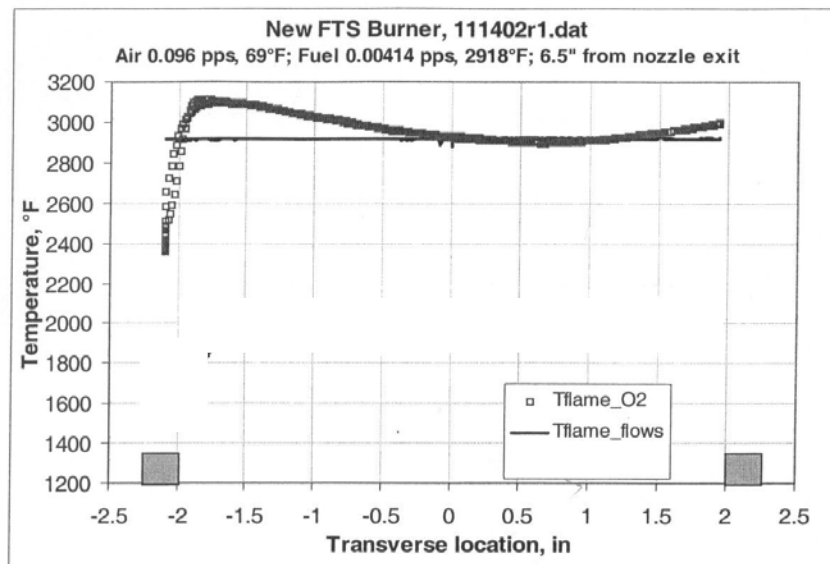


Figure 1-32. Flame temperature variation through the flame near the exhaust end of the quartz liner.

A global or averaging emission probe with a series of holes extending across the width of the quartz tube was attached to the tube's open downstream end, as shown in Figure 1-33.

Final Report

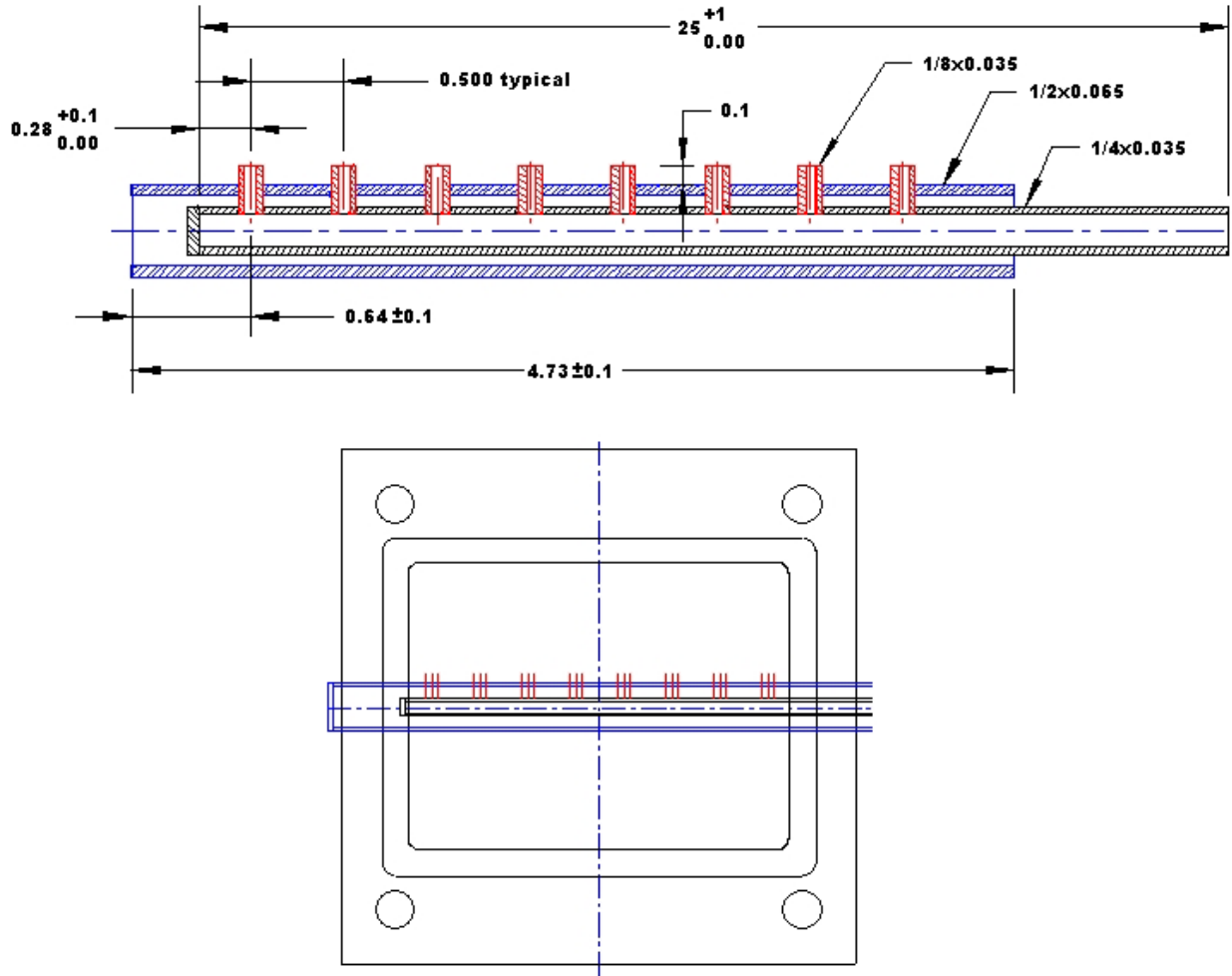


Figure 1-33. Distributed emissions probe.

Figure 1-34 shows the excellent correlation between the flame temperatures determined by measuring the unburned O_2 at the end of the flame containment shroud (quartz tube) using the disturbed averaging probe and those obtained by calculating the flame temperature using the fuel and air flows. The agreement is remarkable. Even though the temperature variation from side to side was $200^\circ C$, the distributed emission probe did an excellent job of averaging thereby enabling its temperature determination to agree with that of the fuel and air flow temperature calculations. This result shows the capability of the single flame using 100% premixed atmospheric combustor and when heated air is used. This approach eliminated the previous divergence between the two methods at the low flame temperatures.

Final Report

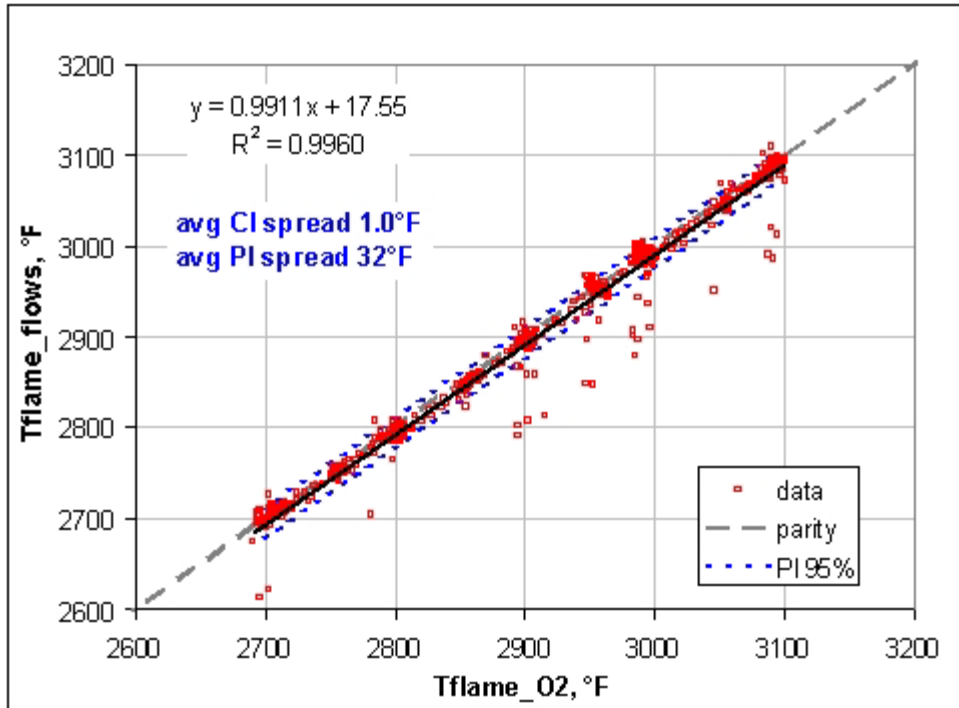


Figure 1-34. Comparison of flame temperatures determined by the oxygen emission probe and combustible gas flows.

1.6.2 Combustor Experiments and Results

1.6.2.1 Combustor Test Results and Dual Diode Simulations

Using Spectrometer Data

Early results using the filter-in-and-out method and a single diode flame sensor indicated that the ratio of filtered to unfiltered signals was much higher than expected. The use of a fiber optic spectrometer showed that the OH band extended farther into the long-wavelength region than the LIFBASE computer code indicated. Staff at Stanford's High Temperature Gas Dynamics Laboratory explained that the difference arose because numerous line intensities were not included in the code we were using. Further simulations of expected sensitivity of the ratio to flame temperature changes were made using spectrometer data instead.

These simulations were done by overlaying the spectrometer data with the SiC photodiode's responsivity versus wavelength to obtain the unfiltered diode's responsivity and combining that with the filter characteristics to get the filtered diode's responsivity. The calculations resulted in ratios that were variable from diode to diode, which is not too surprising given the differences in spectral responsivity observed in Figure 1-19. It should be noted that in the current prototype sensors, the amplifier gain for the filtered diode was increased by a factor of 3. This added factor of 3 was also simulated, as shown in Figure 1-35.

Final Report

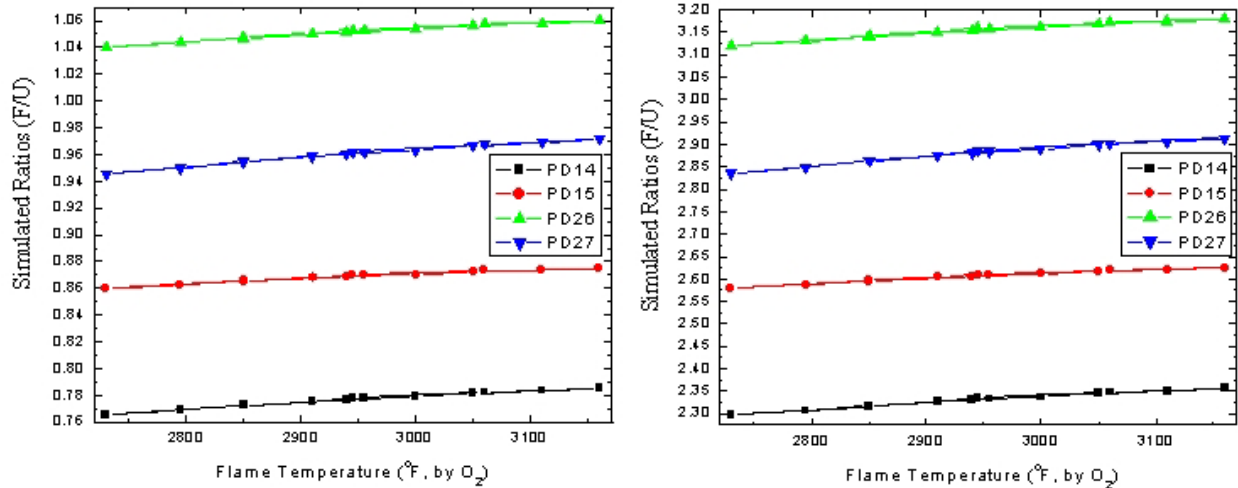


Figure 1-35. Simulated ratios using spectrometer data for the four 1.5 mm chips. At left, the as-simulated values (no gain), and at right, those values multiplied by 3.

When compared to measured ratios, the agreement with simulated ratios is reasonable, as shown in Figure 1-36.

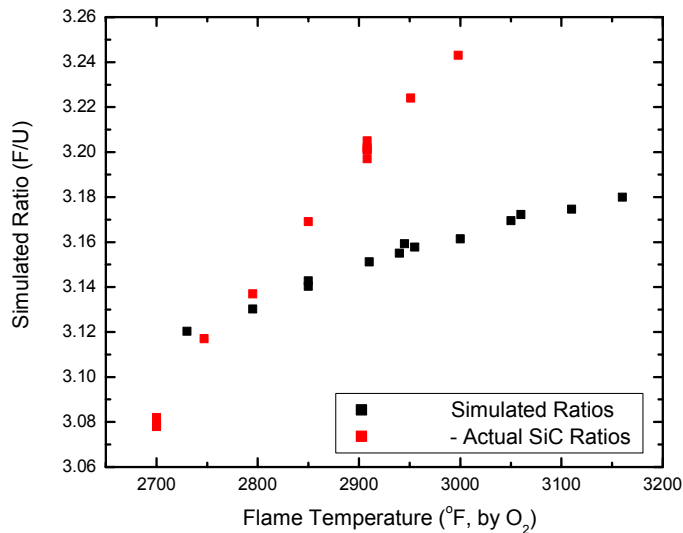


Figure 1-36. Comparison of simulated and measured ratios of PD26.

After the the atmospheric combustor was upgraded, and a water-cooled adjustable iris was built to control the field of view, a number of experiments were performed. These experiments were done using dual diode chips packaged and mounted on the circuit board within the standard stainless steel flame detector housings designed by Reuter Stokes. Two operational amplifiers were included on this circuit board, and these two outputs were connected to A/D converters whose output was sent to a PC. In addition, the fiber from the spectrometer was also mounted in a flame detector housing in the same location as the photodiode chip would be. This setup is shown in Figure 1-37.

Final Report

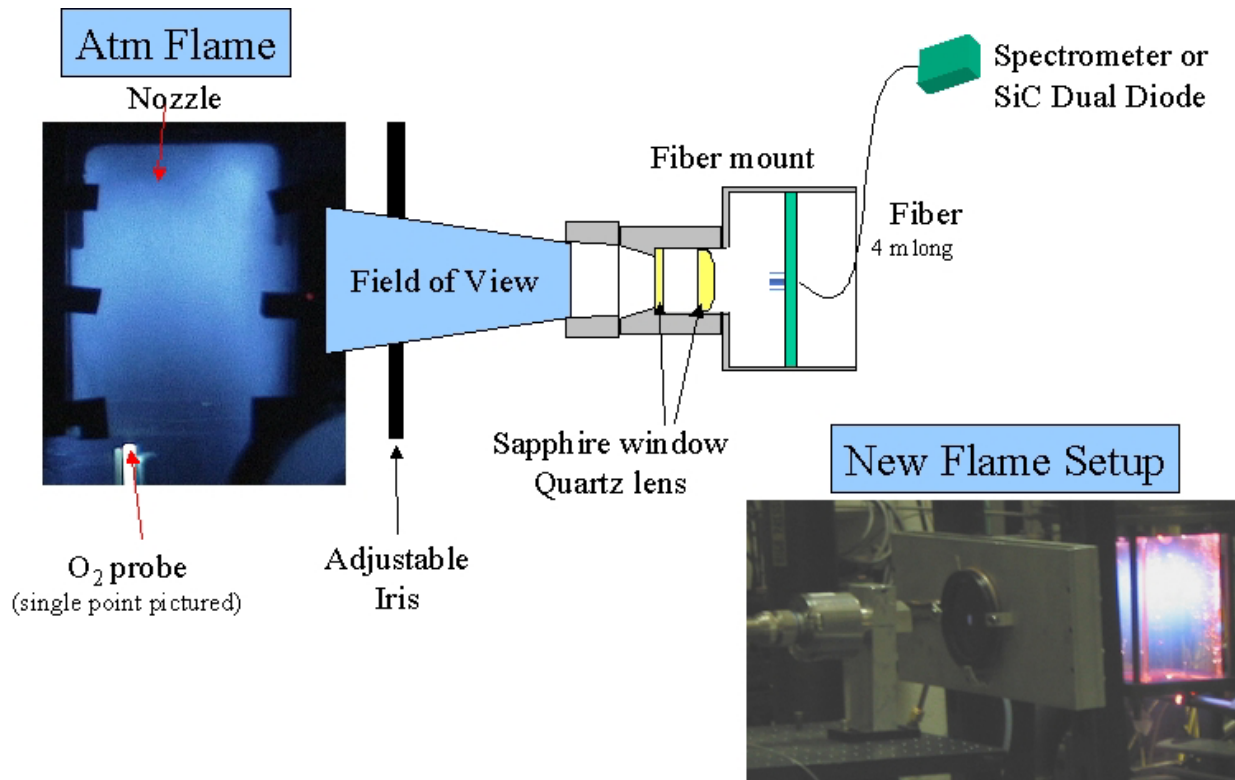


Figure 1-37. Experimental apparatus for flame temperature measurements using either an optical fiber optic spectrometer or dual SiC photodiode sensor.

Two basic sets of measurements were carried out. One set was to focus near the downstream end of the combustion zone and change the fuel flow in order to ramp the combustion temperature up and down. The other set was to fix the temperature and scan the flame axially. A detailed overview of these experiments is shown in Appendix Section 1D.1.

1.6.2.2 Spectrometer Data

Figure 1-38 shows the intensity as a function of distance from the nozzle for three temperatures. Numerous runs were also done by changing the fuel flow to change the temperature. This was done by starting high, at about 3100°F; sweeping down to about 2700°F, and then returning to the high point.

The ratio data for two sets of temperature sweeps on separate days is shown in Figure 1-39. These ratios were obtained by integrating the long-wavelength intensity (ratio numerator) and that between the shorter wavelengths (ratio denominator). The sensitivity to a change of 20°F is a remarkable 2.4%, and the linearity is excellent. Some of the raw data from Figure 1-39 is re-plotted in Figure 1-40 to highlight the precision of the sensor using statistical rigor. Temperature versus measured ratio shows a prediction interval of $\pm 30^\circ\text{F}$ and a confidence interval of $\pm 10^\circ\text{F}$ in Figure 1-40. This data confirms the feasibility of the concept.

Final Report

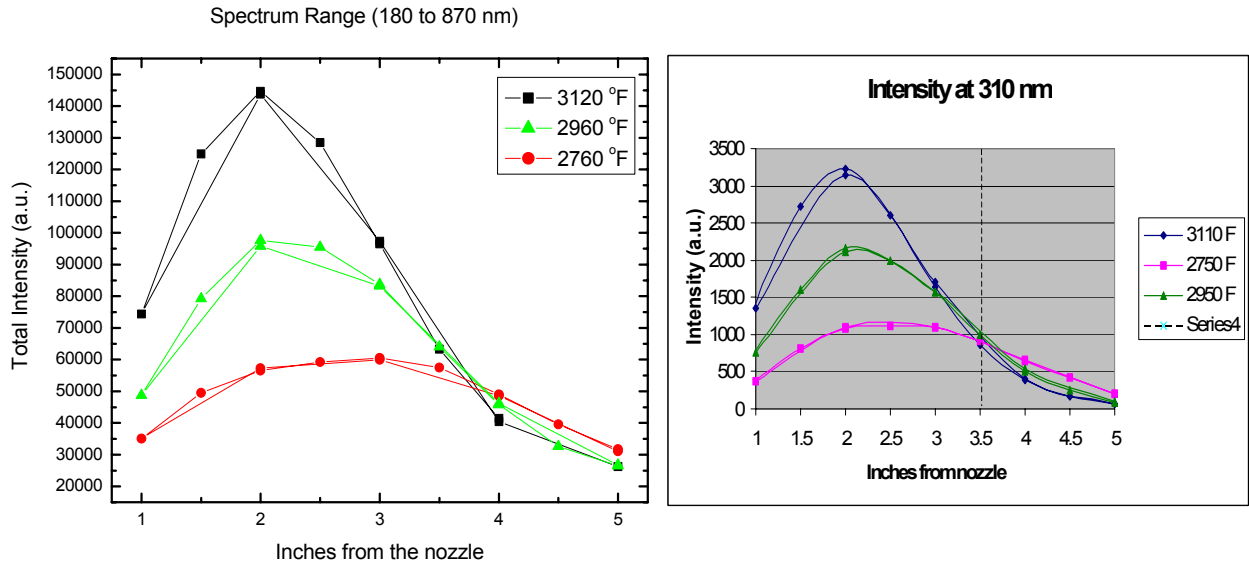


Figure 1-38. Spectral intensity versus position of the flame. The integrated intensity for the range of 180 to 870 nm (left) and the line intensity at 310 nm (right) show relatively good agreement.

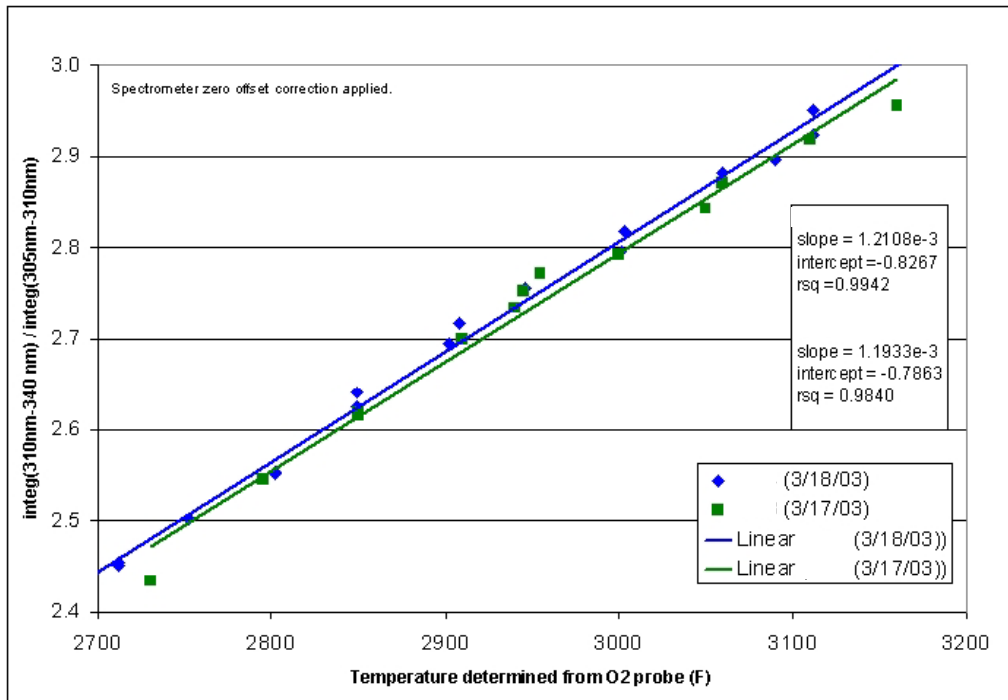


Figure 1-39. R(T) spectrometer data using a ratio of the OH band intensity as specified.

Final Report

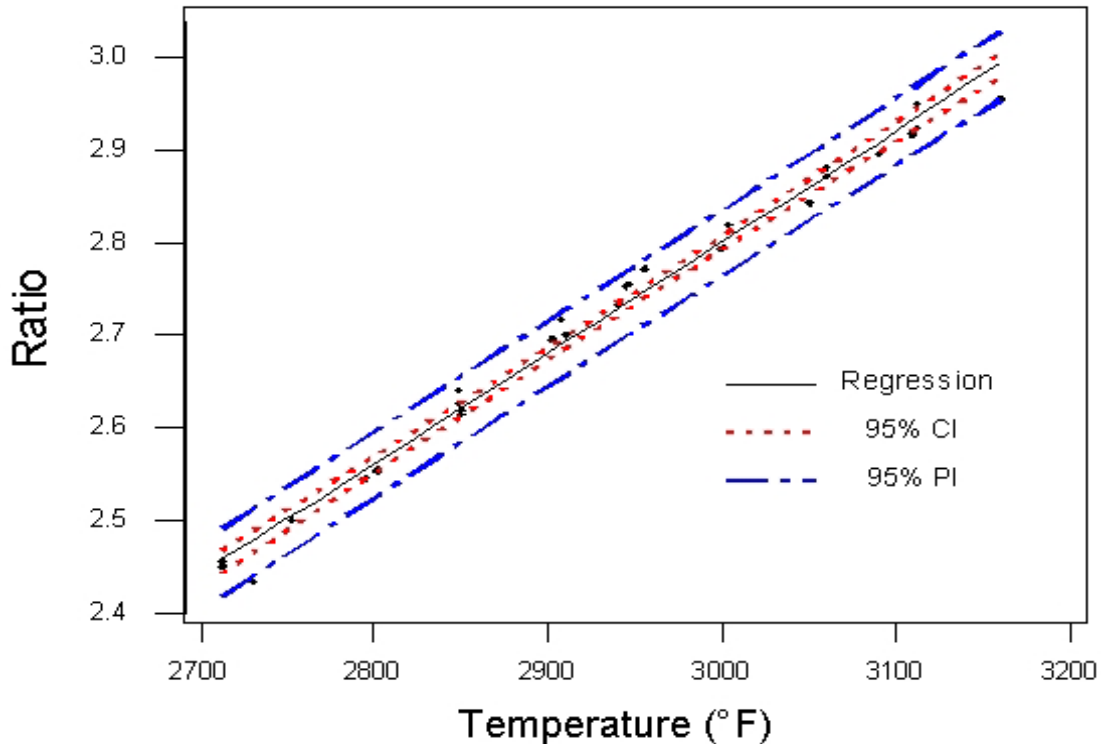


Figure 1-40. Spectrometer R(T) prediction interval and confidence interval.

Dual diode data was also taken using temperature and axial sweeps as was done using the spectrometer. In this instance each data point on the graphs is a time average of several thousand ratios using data rates of 200 and 500 Hz. The results are shown in Figure 1-41. The nature of the outliers in Figure 1-41 is presently unknown. The source of error may be from the testing facility, where the accuracy of the oxygen measurements is more limited, or where the rig shifted to a different combustion regime. There is no physical reason why the sensor itself would be less accurate at higher temperatures; however, there is no data that definitively indicate that. The slope and line fitting difference in the two rates of data sampling highlight the likelihood that the faster the sample rate (to a point), the more accurate the measurements. The increase in accuracy may be due to the higher rate of capture of flame fluctuations when the sensor's signal is taken at a faster frequency. To avoid aliasing of certain flame phenomena including dynamics, the intent is to sample at a minimum of 500 Hz. Beyond that, the nature of the cause is unknown. The 1% sensitivity shown in Figure 1-41 is the percentage change in the raw signal. That is, for example, a 0.01 V shift every 20°F with a baseline signal of 1 V. The sensitivity of about 1% per 20°F change in flame temperature is remarkable.

The prediction interval of $\pm 45^\circ\text{F}$ and a confidence interval of $\pm 20^\circ\text{F}$ is shown in Figure 1-42. Measurement of the sensor performance could be plotted as the uncertainty of flame temperature given a measurement of the ratio. However, the expectation of this plot would be that it would show the reduction in residuals as a percentage of the overall ratio, but will not be significant.

Final Report

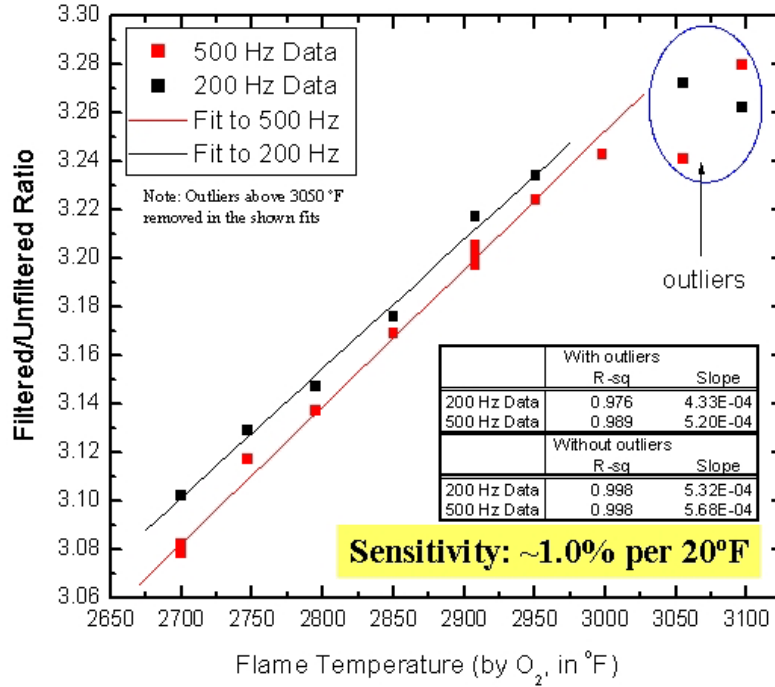


Figure 1-41. R(T) data obtained using the first generation Dual Diode Sensor.

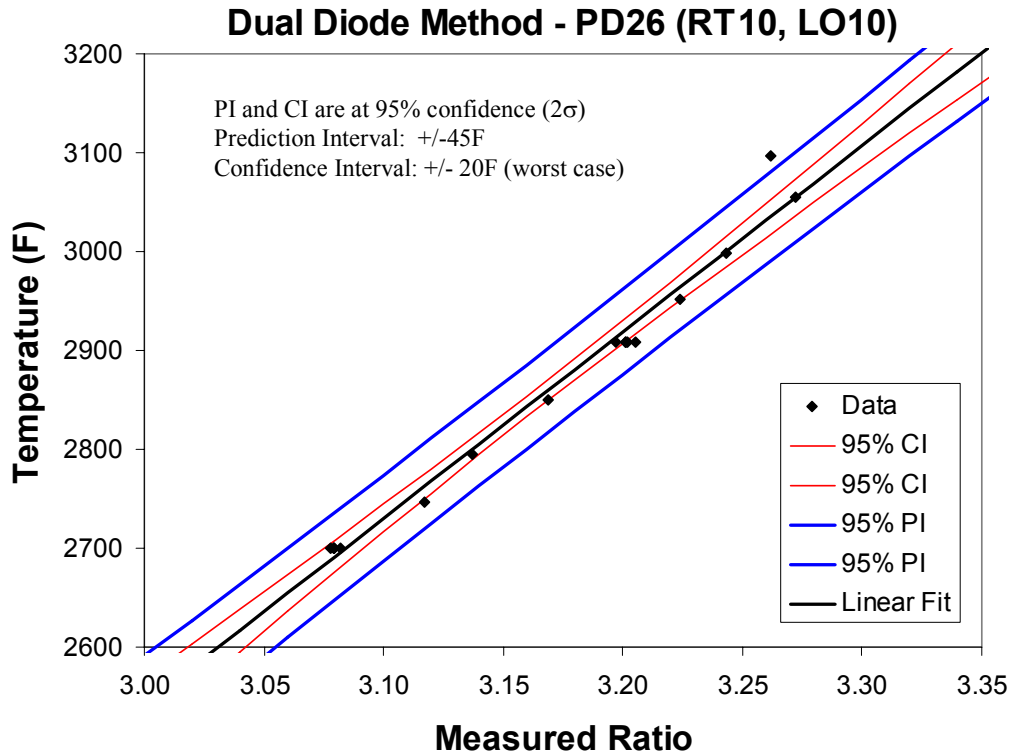


Figure 1-42. Mod 1 Dual Diode Sensor R(T) prediction interval and confidence interval.

Final Report

1.7 DISCUSSION OF RESULTS

This study demonstrated the feasibility of the segmented OH band intensity ratio concept. It also achieved the sensitivity and accuracy goal. The method that was used is independent of the distribution of OH molecular excitation levels (temperatures) within the sensor's field of view since it yields the specific volumetric average temperature.

Three methods of proving this concept were investigated. The GaN, AlGaN method was eliminated because this technology is not yet mature enough. The SiC long pass multiple layer dielectric filter approach was therefore pursued. Even though the first batch of photodiodes presented technical difficulties, this method is feasible.

The specific volumetric average ratios will uniquely determine the average volumetric flame temperature for the volume within the field of view. Therefore the temperature determined will depend on how the sensor is aimed at the combustion flame.

The method is capable of remarkably high sensitivity, exceeding 2% per 20°F at temperatures as high as 3000°F for the spectrometer method. The SiC dual diode method should also be capable of approaching this degree of sensitivity once the technical difficulties of the first such devices are corrected. The accuracy was also proven to be remarkable, showing a confidence level of $\pm 10^\circ\text{F}$ for the spectrometer data. However, it should be noted that there may be a degree of offset between the ratios and their calibration as a result of using unconsumed oxygen in the exhaust. This is because the field of view was relatively large in order to get good signal levels for the short LM6000 flame.

Even so, an advantage not yet realized by those who have tried other methods is the robust size of the signal levels because the signal intensity results from integrating the intensity over a large group of lines and is not dependent on the intensity of a single line. It should also be noted that the shape of the OH band is independent of pressure whereas individual spectral lines are not.

This method is therefore well qualified to monitor the temperature of premixed hydrocarbon flames. And the sensitivity and accuracy numbers are much superior to any method previously reported in the literature.

1.7.1 Sensor Calibration

Two types of sensors were explored: a SiC dual diode and a photospectrometer. Both types can be calibrated using (1) the experimentally determined OH spectrum characteristics for a set of different equivalence ratios or (2) final combustion temperatures. These final temperatures were determined both from fuel/air mixtures and from the unburned oxygen concentration in the exhaust. Both of these methods were in excellent agreement because care was taken to eliminate air leaks. In fact this set of spectra could be regarded as a calibration set for all future OH segmented band ratio detectors. In this regard the ratios for fiber optic detectors are already calibrated if it may be assumed that all the sensor spectrometers to be used were calibrated at the factory to correct for the wavelength variation in quantum efficiency for each of the pixel elements in the CCD sensor chip. In the case of the dual diode chip, it cannot be assumed that the spectral responsivity as a function of wavelength will be the same for every chip. That will require that the sensor be calibrated after assembly by measuring the responsivity characteristics using a monochromator. These characteristics are then superimposed over the set of OH spectra shown in Figure 1-39 to get the ratio as a function of temperature. The sensor housing will then

Final Report

be marked with a calibration code, which in turn would be installed in the control software deck, or alternately an electronic control chip could be added to in the electronics within the sensor housing. Clearly the present SiC dual diode technical difficulties need to be resolved for optimum performance.

1.8 DISTRIBUTED CONTROL SYSTEM FACTORS

The original plan of combining the capabilities of the present SiC flame detector (FD) so that it can also determine flame temperature using the SiC dual diode may not be a practical commercialization route. There are a number of reasons for this.

First, the SiC FD is a well-established, stand-alone product. SiC FD ports have already been installed in numerous gas turbines where the FD performs admirably. Because of the automatic gain switch, the electronic circuitry has enormous dynamic range. For example, it can detect light off the secondary flame in a DLN-1 combustor, which requires “seeing” the flame axially through a one-eighth-inch-diameter hole in the swirler yet can still track the flame intensity to full power. Because the Flame Temperature Sensor (FTS) requires linear amplification, however, its dynamic range is limited.

The various FD ports are most probably not located in the correct position for good flame temperature measurements. Because the linear amplifiers have a limited dynamic range, the gain of the amplifiers needs to be determined for the FTS. Signal output levels using the LM6000 flame were used to determine the size of the feedback resistor. The optimal method to manage this in a real system has yet to be determined. Software would be needed to make decisions in order to maintain the voltage output within range and keep track of the load resistor value. This method would avoid the need to tamper with the circuit inside the detector housing. Also in order to track flame dynamics in every combustion section (or can), the AC component of the signal needs to be extracted, probably amplified, and sent to the fast Fourier transfer (FFT) card in the control room.

All of these issues of gain and dynamic range also apply to the spectrometer method. Because the spectrometer has a very low response time, it would not be able to track dynamics.

1.9 CONCLUSIONS

The Flame Temperature Sensor portion of the Smart Power Turbine Program was highly successful. This research used a careful approach to the design, development, and testing of novel sensors, yielding proof of concept demonstrations in front of a combustion nozzle. The final result of this project was a pair of candidate tools—the SiC dual diode and the photospectrometer—both of which demonstrated high promise for greatly improving the efficiency of power generation technology, while offering a controlled level of emissions.

Plans are being made to demonstrate the practicality of this concept using large multiple-nozzle combustors used in GE Power System gas turbines. If these demonstrations are successful, a means of controlling the fuel flow for every combustor can on the turbine may be realized using vernier fuel flow valves. They would be part of the closed loop control system that takes advantage of the Flame Temperature Sensor. Using closed loop control would ensure that every combustor is working at its best operating point to maximize efficiency while maintaining safe levels of NO_x emissions. In some cases, that could mean a reduction in NO_x emissions by thousands of tons per year.

Final Report

1.10 REFERENCES

- Brown, D.M., and J.L. Henkes, "Gas Turbine Combustion Control Using Flame Spectroscopy to Reduce NO_x", GE CRD Memo (1991). Abstracts from this memo are included in Appendix Sections 1A.1 through 1A.3 of this report.
- Brown, D.M., E. Downey, M. Ghezzi, J. Kretchmer, R. Saia, Y. Liu, J. Edmond, G. Gati, J. Pimply, and W. Schneider, "Silicon Carbide UV Photodiodes," *IEEE Trans. Electron Dev.*, 1993, vol. 40, pp. 325-333; *Trans. First International High Temperature Electronics Conf.*, Albuquerque, NM., June 1991, pp. 214-219.
- Brown, D.M., E. Downey, J. Kretchmer, G. Michon, E. Shu, and D. Schneider; "SiC Flame Sensors for Gas Turbine Control Systems," *Solid State Electronics*, 1998, vol. 42, no. 5, pp. 755-760.
- Brunner, D, H. Angerer, E. Bustarret, F. Freudenberg, R. Hopler, R. Dimitrov, O. Ambacher, and M. Stutzmann, "Optical constants of epitaxial AlGa_N films and their temperature dependence," *Journal of Applied Physics*, 1997, vol. 82, pp 5090 ff.
- Dean, A.J., "Single Cup Dual Fuel DACRS Testing: SiC Detector Measurements," May 26, 1994, M&I REP 2.Doc.
- Hicks, Y.R., R.J. Locke, R.C. Anderson, M. Zuller, and H.J. Schuck, "Imaging Fluorescent Combustion Species in Gas Turbine Flame Tubes: On Complexities in Real Systems," NASA Technical Memo, 107491, 33rd Joint Propulsion Conference, Seattle, Washington, July 1997.
- Kordina, O., J.P. Bergman, C. Hallin, E. Janzen, "The Minority Carrier Lifetime of n-type 4H- and 6H-SiC Epitaxial Layers," *Appl. Phys. Lett.*, 1996, vol 69, no. 5, pp. 679-681.
- Rea, E.C., "Rapid-Tuning Laser Wavelength Modulation Spectroscopy with Applications in Combustion Diagnostics and OH Line Shape Studies," High Temperature Gasdynamics Laboratory of the Mechanical Engineering Dept., Stanford University, Topical Report, March 1991.
- Sandvik, P.M., D. Walker, P. Kung, K. Mi, F. Shahedipour, V. Kumar, X. Zhang, J. Diaz, C. L. Jelen, and M. Razeghi, "Solar-blind AlGa_N p-i-n photodetectors grown on LEO and non-LEO Ga_N," in *Photodetector Materials and Devices* vol.V, ed. Gail J. Brown, *SPIE Proceedings Series 3948*, Bellingham, Wash. 2000, pp. 265-272.
- Vaidza, D.B., J.J. Horvath, and A.E.S. Green, "Remote Temperature Measurements in Gas and Gas-Coal Flames Using the OH (0,0) Middle-UV Band," *Applied Optics*, 1982, vol. 21, no. 18, pp. 3357-3362.

Final Report

2 FUEL QUALITY SENSOR

2.1 INTRODUCTION

For decades the standard device for detecting the presence of combustible gases, such as methane and propane, has been the pellistor. In this device, an embedded resistive temperature sensor is used to detect the heat of combustion on an electrically-heated catalytic bead. Since the early 1990s there have been numerous attempts to miniaturize this device to improve its time response, thermal efficiency, and manufacturability. In addition to miniaturization, an improved sensor platform would have to be designed to withstand high temperatures in a chemically-reactive environment, while maintaining the small thermal mass necessary for a fast time response. Micro-pellistor research has shown that these devices can exhibit improved time response and efficiency over their macro-sized counterparts. Since integrated-circuit-like batch manufacturing technology is used to make the sensor platform, the ease of platform manufacturing has improved with miniaturization. Despite the manufacturability and performance advantages of the micro-pellistor, the catalyst deposition on the sensor continues to be a major manufacturing bottleneck; the deposition of fine amounts of robust catalyst is difficult to control on such a small platform. In the work reported here, the approach taken to catalyst deposition on the fuel performance sensor has required the development of novel deposition techniques, for example, the use of a micropen system.

Design and manufacturing challenges were addressed in an attempt to use a micro-pellistor as the basis for a Fuel Quality Sensor System to measure in real-time, or near real-time, the LHV of natural gas. The LHV sensor is now performing rapid calorimetry measurements on a broad range of natural gas fuels. If the LHV of fuels can be determined in near real-time, power generation facilities using such fuels can adjust operational parameters on a more rapid time scale than is now possible. Implementation of the LHV sensor in future power turbines would potentially increase the efficiency of turbine operation and result in more economical production of electricity.

2.2 DEVICE DEVELOPMENT

The primary goal of the LHV Sensor project was to develop a cost-effective device to monitor in real-time, or near real-time, the LHV of natural gas. The device will be based on a macro-scale gas combustion sensor, called a pellistor, that utilizes catalytic combustion. These devices have been used for decades to sense combustible gas. Pellistors are used in pairs, with one device catalytically combusting fuel and the other acting as a reference source to account for signal drift. The sensing mechanism involves measuring the resistance change of a heated platinum wire or bead. Natural gas that contacts the heated catalyst will oxidize, releasing heat that will increase the resistance of the filament. This heat release will be proportional to the concentration of the analyte. The reference pellistor will not initiate combustion; however, it will be used to account for changes in gas flow and ambient temperature. This stable sensing system has made pellistors a standard for combustible gas sensing. The production of a similar, micro-sized, device would allow for the measurement of fuel LHV. Because of its small thermal mass and superior thermal isolation, a micro-sized device would have high sensitivity to thermal fluctuation. While gas chromatography is the current standard method for LHV sensing, the cost of such systems is prohibitive for large-scale use in gas turbine plants. The LHV Sensor was

Final Report

created using batch fabrication techniques that make large numbers of devices in each lot, which lowers the device cost significantly.

Since stable flames are difficult to achieve on a small scale because of enhanced heat loss arising from large surface-to-volume ratios, catalysts will be used in the LHV Sensor as well. Catalytic materials provide a natural, surface-based method for flame ignition and stabilization. The combination of a microhotplate—to provide precise heating and temperature measurement—with catalyst materials—to provide for sustained combustion on the microscale—will form the basis of the LHV Sensor. During sensor operation, the microhotplate will heat the catalyst, which will in turn sustain natural gas combustion over the surface of the device. The thermal energy liberated by this combustion will then be measured by the hotplate to determine the Btu content of the natural gas and, ultimately, the LHV of the fuel.

2.2.1 Lower Heating Value Sensor Production

2.2.1.1 Microhotplate Design

The microhotplate, which provides precise heating and temperature measurement, consists of a thin, 1- μm (0.039-mil) thick, membrane of low-stress silicon nitride suspended from a silicon frame. Thin meander wiring of Ti/Pt, which provides both temperature sensing and heating, covers the surface of the suspended membrane. The heating elements double as temperature sensors by using a circuit to monitor the resistance change of the wire caused by thermal fluctuations. A device schematic is shown in Figure 2-1 and an image of the device top in Figure 2-2.

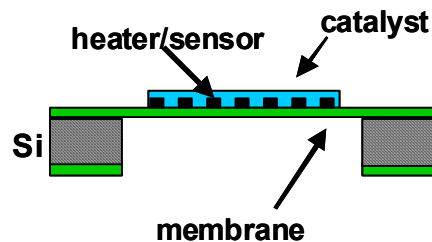


Figure 2-1. Schematic of a microhotplate cross section.

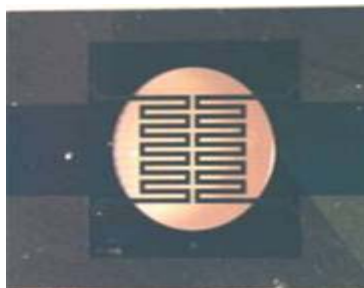


Figure 2-2. Top view of a microhotplate.

Analysis of the design shows the many benefits, and some of the drawbacks, of this micro-scale device. The silicon nitride membrane has an extremely low thermal conductivity, stemming from its material properties and its thickness, which gives the device the necessary thermal isolation.

Final Report

This high thermal isolation, coupled with the extremely small device mass, provides for a high thermal sensitivity, typically better than $0.4 \text{ mW}/^\circ\text{C}$ ($0.0014 \text{ Btu}/(\text{hr } ^\circ\text{C})$). Although an excellent temperature sensor, this device did have some drawbacks. The thin silicon nitride membrane was brittle, so special care had to be taken during fabrication, catalyst deposition, and device testing; otherwise membrane rupture would ruin the device. Adhesion between the silicon nitride membrane material and catalysts was also poor. The chemical resistance of silicon nitride meant that the alumina and platinum catalysts formed poor bonds with this material. Additionally, the thin Ti/Pt wiring required significant modification as the sensor program progressed. The titanium adhesion layer was vulnerable to oxidation caused by the high temperatures involved in testing, as well as the chemically reactive environment in which the devices were tested. Titanium oxidation can cause radical resistance variations to arise within the wiring, as well as delamination of the wiring from the membrane. Both of these conditions could render the devices unusable.

2.2.1.2 Microhotplate Fabrication

The method of microhotplate fabrication in this task, using batch fabrication techniques and the process flow described below, allowed large numbers of devices to be made in parallel. The costs of each fabrication step are spread among many devices, reducing the overall device cost. Simultaneous fabrication of the devices also insures a high degree of uniformity across the devices within a single lot; the LHV Sensor, like the macro-sized pellistors, requires a closely matched reference and active device for optimum performance.

Before device fabrication in Sandia's cleanroom facilities began, the silicon wafers were sent to an outside vendor that deposited the silicon nitride layer with the necessary specialized equipment. At Sandia, a thin-film Ti/Pt heater was patterned, using e-beam evaporated metal; typically, $\sim 1700 \text{ \AA}$ (0.0066 mil) of Pt and a 100 \AA (0.00039 mil) Ti adhesion layer were used. Another patterning step placed thick, $1 \text{ }\mu\text{m}$ (0.039 mil), gold pads for electrical contacts on the surface. On the opposite side of the wafer an opening centered on the heater was plasma etched in the silicon nitride membrane. The membrane was then released by through-wafer silicon etching. Either Bosch plasma etching or potassium hydroxide (KOH) etching could be used to remove the silicon and release the membrane, with no discernable operational differences between the completed devices made by the two methods. For Bosch etching, an etch stop layer of $0.5 \text{ }\mu\text{m}$ (0.0196 mil) of thermally-grown oxide was used to prevent undesired etching of the nitride layer; any residual oxide remaining after the Bosch etch was stripped in buffered hydrofluoric acid. For KOH etching, no additional etch stop layer was required. After etching, the wafer was diced, and the devices were cleaned, separated, and prepared for catalyst deposition.

2.2.1.3 Design Modifications

Over the course of the device development, modifications were made to the basic design that improved device performance and survivability. Improvements to the device wiring were made based on the works of Firebaugh et al. (1998) and Briand et al. (2002). These improvements included the replacement of titanium, as an adhesion layer, with tantalum to increase the long-term survivability of the wiring. The replacement was made because of tantalum's higher resistance to thermal oxidation. To mitigate chemical attack on the wiring and aid in catalyst adhesion, dielectric passivation consisting of thin, alternating overcoats of silicon dioxide and silicon nitride were placed over the membrane and wiring. The overcoats were placed in

Final Report

alternate layers to reduce the overcoat stress, and to fill in pinhole defects that may have formed in any single dielectric layer. Each of the first two overcoats, silicon nitride followed by silicon dioxide, had a thickness of 1000 Å (0.0039 mil), and the final two overcoats were silicon nitride and silicon dioxide with a thickness of 500 Å (0.0019 mil). The last coating of silicon dioxide served as an adhesion layer for the subsequent catalyst deposition.

2.2.1.4 Microhotplate Design Iterations

In addition to the standard design, called the Hot 4 design, several other designs underwent testing. A device using the variable width wiring design, described in Section 2.2.2, was built in small quantities to test performance. In limited testing, these devices performed well, and they exhibited an improved operational lifetime. In the most recent redesign, known as the Hot 7 redesign, this wiring configuration, shown in Figure 2-3, has become standard, replacing the previous meander heater design. Another Hot 7 design iteration involved shrinking the overall membrane to heater ratio. This concentrated the heated zone into a smaller area and therefore reduced the mechanical stresses on the membrane. This observation was reported by Dibbern (1990) and Neda et al.(1996) in the technical literature.

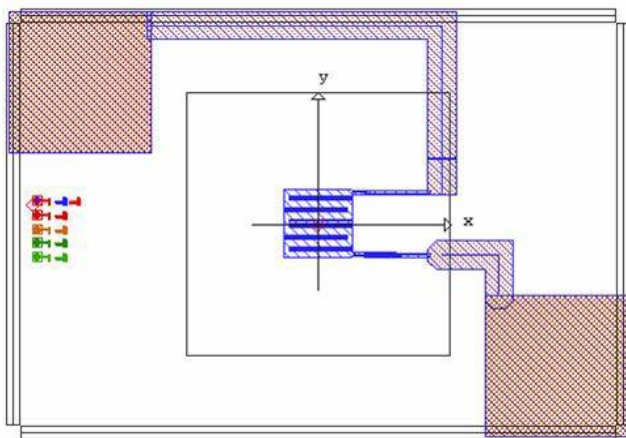


Figure 2-3. Image of Hot 7 design.

The speciation of natural gas constituents required a unique microhotplate design that would integrate a number of elements into a single device. These elements would provide the locations for depositing the variety of catalyst materials needed to perform speciation. The additional elements would also be used for reference devices and to provide system redundancy. A prototype design was constructed that featured a 10-element array of microhotplates combined onto a single device: front and back views are shown in Figure 2-4. This device has been tested in an application similar to the LHV sensor, where it performed well.

Final Report

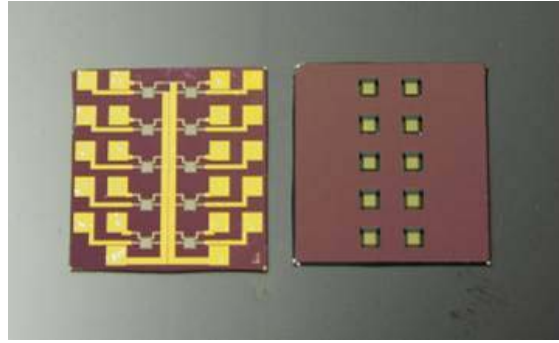


Figure 2-4. Front and back view of the 10-element array.

2.2.2 Modeling

To verify the decisions made during design, as well as to aid in the design of future microhotplate iterations, an extensive program of thermal-electric modeling was pursued. This modeling used a finite element modeling software package called ANSYS multiphysics. ANSYS multiphysics is a sophisticated code that allows the user immense flexibility and provides a variety of modeling options. It is capable of solving a variety of physics, from thermal and mechanical problems to elaborate systems involving the interaction of two or three different physics.

The first model created in ANSYS attempted to replicate the results of a steady-state infrared microscope measurement of the basic microhotplate design. A Barnes InfrascopTM was used for these measurements. This system employed a liquid-nitrogen-cooled array of $5 \times 5 \mu\text{m}$ ($0.196 \times 0.196 \text{ mil}$) InSb pixels with spectral sensitivity from $1.5\text{-}5.5 \mu\text{m}$ ($0.059\text{-}0.216 \text{ mil}$). Radiative emission from the sample was focused on the array by a system of IR optics. In this test, the microhotplate had a voltage load of 3.11 V on its wiring, and was placed on a heated stage elevated to a temperature of 80°C (176°F). Figure 2-5 shows the infrared microscope measurement of this active, heated microhotplate. ANSYS was able to model these results successfully, as shown in Figure 2-6. Replication of these results provided important baseline information such as the proper convection and thermal radiation coefficients to use for future efforts.

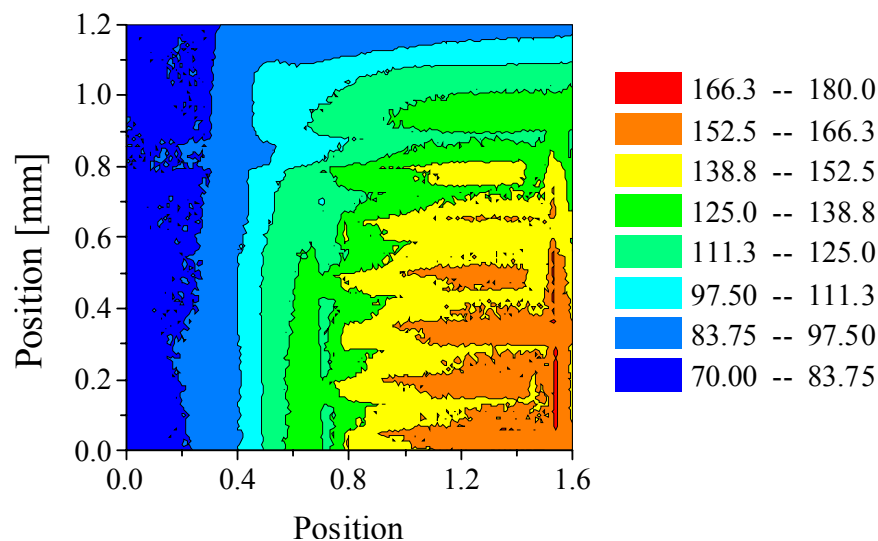


Figure 2-5. Infrared microscope image of a microhotplate.

Final Report

Subsequent ANSYS models were used to design and optimize the pattern of the wiring on the silicon nitride membrane. Since the combustion of the natural gas is sensitive to variations in the temperature of the catalyst, the design goal was to produce a wiring configuration that yielded the largest possible area of uniform temperature. While it was determined that the basic design was acceptable, wiring refinements could greatly increase the size of this area. Figure 2-7 shows a half-symmetry model of a microhotplate designed in ANSYS that features an optimized wiring pattern. This wiring configuration features variable width wiring to promote the concentration and distribution of thermal energy where needed. The variable width wiring design features approximately 50% more thermally uniform area than the basic microhotplate.

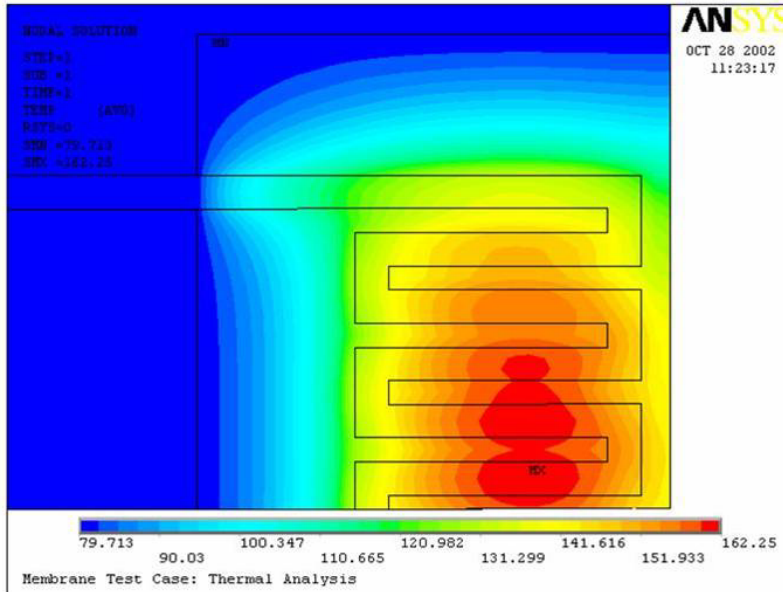


Figure 2-6. ANSYS model of microhotplate.

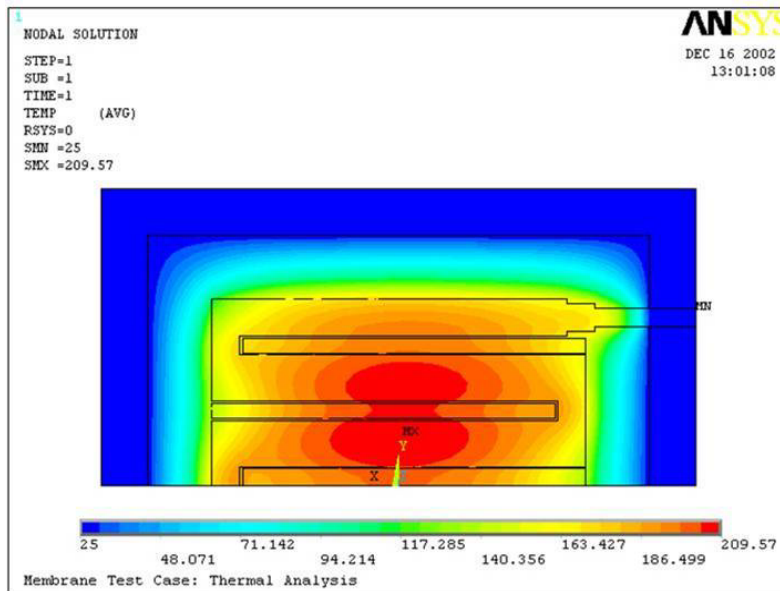


Figure 2-7. Variable-width ANSYS microhotplate model.

Final Report

2.2.3 Catalysts

2.2.3.1 Catalyst Preparation

While the microhotplate senses the heating caused by natural gas combustion, the catalyst promotes and stabilizes this combustion, which makes it a requisite component of the LHV Sensor. The presence of the catalyst allows combustion to occur at a lower temperature than it would if thermal energy alone was used to initiate combustion. This lower temperature operation results in an extended microhotplate lifetime. Given the importance of the catalyst's function, it must be deposited with repeatability and precision. Failure to do so could result in making the analysis and repeatability of the device signal suspect.

The catalysts used in this program included both commercial and internally developed formulations. The commercial catalysts came from Industrial Scientific Corp. The Industrial Scientific Corp catalysts (proprietary formulations) were platinum, palladium, and rubidium based. The Sandia catalyst powders, consisting of pure alumina (for the reference device), 1 wt% Pt/alumina, 10 wt% Pt/alumina, and 1 wt% Pd/alumina, were calcined for 2 hours at 600°C (1112°F) in air and were prepared by incipient wetness.

2.2.3.2 Catalyst Deposition

To apply the catalyst to the microhotplates for this task, novel approaches to catalyst deposition had to be developed. Commonly used methods such as silk-screening and slurry deposition (Zanini et al. 1994) lacked the precision and repeatability needed. In order to achieve repeatability, an Omicron Micropen 400 printing system was adapted for catalyst deposition. The Micropen is a thick film direct-write tool originally designed for the microelectronics industry to deposit thin film capacitors and resistors. It can control film geometry and thickness very accurately, which makes it a suitable candidate for repeatable catalyst deposition. It writes patterns by dispensing a slurry/paste through a pen tip onto a moving X-Y print table. For the catalyst layers, a print area was designed in AutoCAD to fit on the active area of a microhotplate and transferred to a print file within the Micropen software package.

Pastes or "inks" suitable for direct-write printing with the micropen had to be created from the catalyst powders. Both aqueous (water + additives) and organic solvent systems were used in paste production, although only aqueous pastes were evaluated for the data presented here. For aqueous pastes, the powder catalysts were dispersed in water with a pH adjusted to ~ pH 4 using nitric acid. A drying inhibitor, Avecia Humectant GRB2, was added to prevent rapid evaporation, which would otherwise clog the pen tip between printing runs and cause cracking of the deposited paste during drying. The alumina/water/GRB2 paste was mixed, for 15 minutes using a Specs Mill, in a Nalgene bottle with alumina media to reduce catalyst agglomerate size. Reduction of agglomerate size is necessary to allow smooth paste flow through the Micropen tips, which are 25-250 μm (0.984-9.84 mil) in diameter. Pastes were partially dried or diluted with water and milled again until the desired rheology was obtained. The final paste had a weak yield stress and resisted flow due to gravity but flowed easily under applied pressure, as in the micropen print conditions. Typical pastes were in the range of 10-30 volume percent solids. A printed, 25 μm (0.984 mil) thickness Pt:Al₂O₃ catalyst pad is shown in Figure 2-8. The thickness of the catalyst layers was designed to be in the range of 25-75 μm (0.984-2.95 mil), where high reproducibility and good adhesion were obtained. The micropen dispenses a controllable volume of paste per time, enabling control of thickness by varying print volume, paste concentration, and

Final Report

write speed. Film thickness was characterized using a COBRA laser profilometer. The printed catalyst pads were dried at 100-300 °C (212-572 °F) to enable solvent removal.



Figure 2-8. Printed Pt catalyst pad.

2.3 EXPERIMENTAL

2.3.1 Apparatus

2.3.1.1 Test Fixtures

Test fixtures were required for experimenting with the catalyst-coated microhotplate LHV sensor to deliver fuel/air mixtures and for electrical input/output functions. Initially, conventional semiconductor dual in-line packages (DIPs) were used for electrical connections; fluidic connections were achieved via machined glass flow lids affixed over the active area of the LHV sensor. The small size and insulating properties of these lids meant that water vapor, created by combustion, could condense in the fixture interior, making combustion difficult to maintain and causing pressure fluctuations capable of rupturing the device. The application of the lids to the substrates was a difficult task, often causing membrane rupture. Overall, this was a time-consuming process, with low yield, and was eventually abandoned for packaging schemes tailored to specific experimental needs.

To address the issues with the glass lid and permit drop-in replacement of the LHV sensor, a fixture with a larger internal volume was constructed. This approach is a step on the way to modular packaging for easy replacement of the device in the field. Figure 2-9 shows the combustion fixture, which had the necessary ports for gas flow, electrical interconnection, and temperature sensing. Internally, the fixture's volume was about 683 mm³ (0.0416 in³). The gas inlet, with an inner diameter of 315 μm (12.40 mils), was placed about 1.5 mm (0.059 in) above the LHV sensor, which assured that the fuel/air stream would not directly impinge on the LHV sensor. The fixture used conventional wiring, which could be manually soldered onto the microcombustor dies to accommodate various bond pad layouts. Overall, this fixture reduced device preparation time significantly. The larger internal volume meant that water vapor was free to exit the fixture, instead of dousing the flame as it had previously, and that the membranes were no longer subjected to failure-inducing pressure loadings. The base plate of the fixture had the necessary space to mount two LHV sensors, which made it possible to test various coatings simultaneously in an array concept. At a minimum, an active catalyst device and an inactive reference device are required; Figure 2-9 shows this configuration. The active and inactive devices respond similarly to flow and temperature variations so these common mode effects can be canceled. After catalyst deposition and fixturing were complete, the device was tested.

Final Report

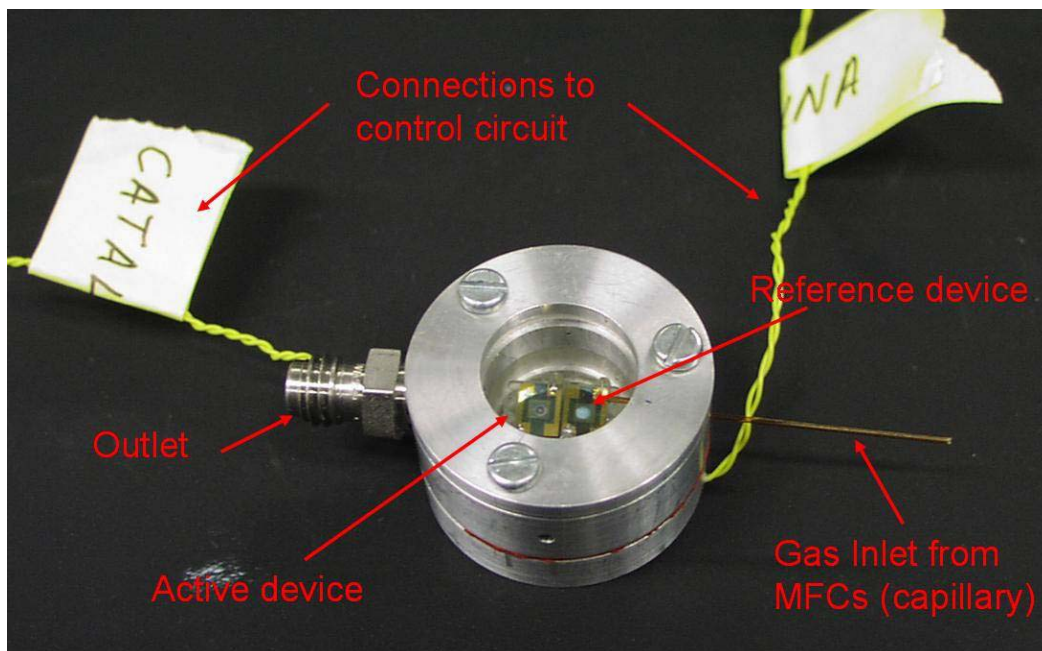


Figure 2-9. Combustion fixture.

2.3.1.2 Control Circuits

The microhotplate platform for the LHV sensor contains a resistive heater. Using appropriate circuitry, the resistance can be measured during operation and, applying the measured temperature coefficient of resistance (TCR) of the heater, the average temperature of the microhotplate can be inferred. To prevent the temperature of the LHV sensor from varying with combustion conditions, constant-voltage or constant-current operation must be avoided. Constant-resistance operation, on the other hand, maintains constant average temperature of the LHV sensor through the TCR.

A constant-resistance control circuit was developed to heat the LHV sensor to a constant average temperature during use. Figure 2-10 is a schematic diagram of a circuit that controls a single LHV sensor. This circuit was the first one developed in this task. The two operational amplifier circuits shown at the left provide signals proportional to the voltage across and the current through the microhotplate, respectively. Those voltages are divided by the microprocessor section of the circuit and, by Ohm's Law, a voltage proportional to the resistance of the LHV microhotplate is produced. The voltage-proportional resistance is compared with a set-point voltage using the op amp circuit shown at the right on the schematic. The greater the difference between these voltages, the greater the voltage on the gate of the MOSFET and the greater the current provided through the exterior current loop to the microhotplate. When the voltages are equivalent, the feedback current stabilizes in value. To set the temperature on the LHV sensor, the set-point voltage is increased until the desired temperature of the microhotplate, as inferred by the TCR and the proportional resistance, is achieved. The proportional voltage and current are also used to determine the power provided to the LHV sensor during combustion.

Final Report

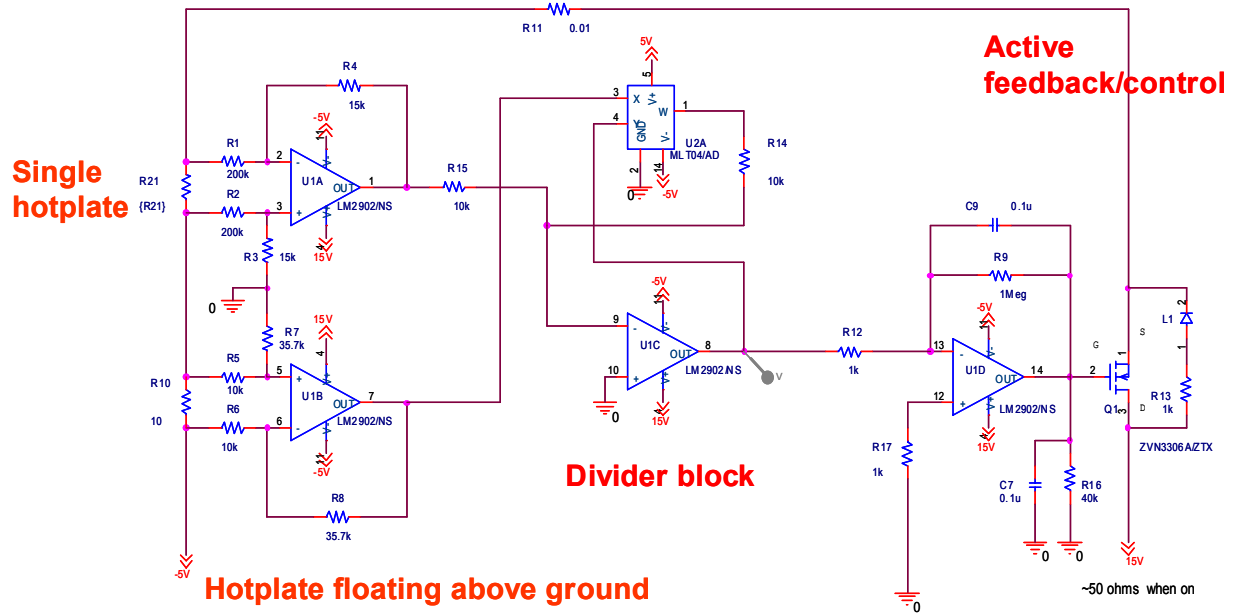


Figure 2-10. Schematic of the constant resistance control circuit.

The circuit of Figure 2-10 worked well for individual LHV sensors. When the circuit was used with the 10-element array design, however, problems were discovered. They arose from the use of a common ground line on the array device, but the low side of the LHV sensor in the control circuit was floated above ground by the current-viewing resistor (CVR). The most recent circuit design remedied this situation by switching the location of the CVR and the LHV microhotplate, grounding the low side of the LHV sensor. To shield the circuit from external effects, buffer stages were added to the input/output locations. Two circuits were added to the same board to learn how, eventually, to operate a multi-element array, and the drive capabilities of the circuits were increased to allow higher maximum operation temperatures. One of the two circuits on the board is shown in Figure 2-11. The performance of this circuit was demonstrated in field trials at the GE Global Research Center.

Final Report

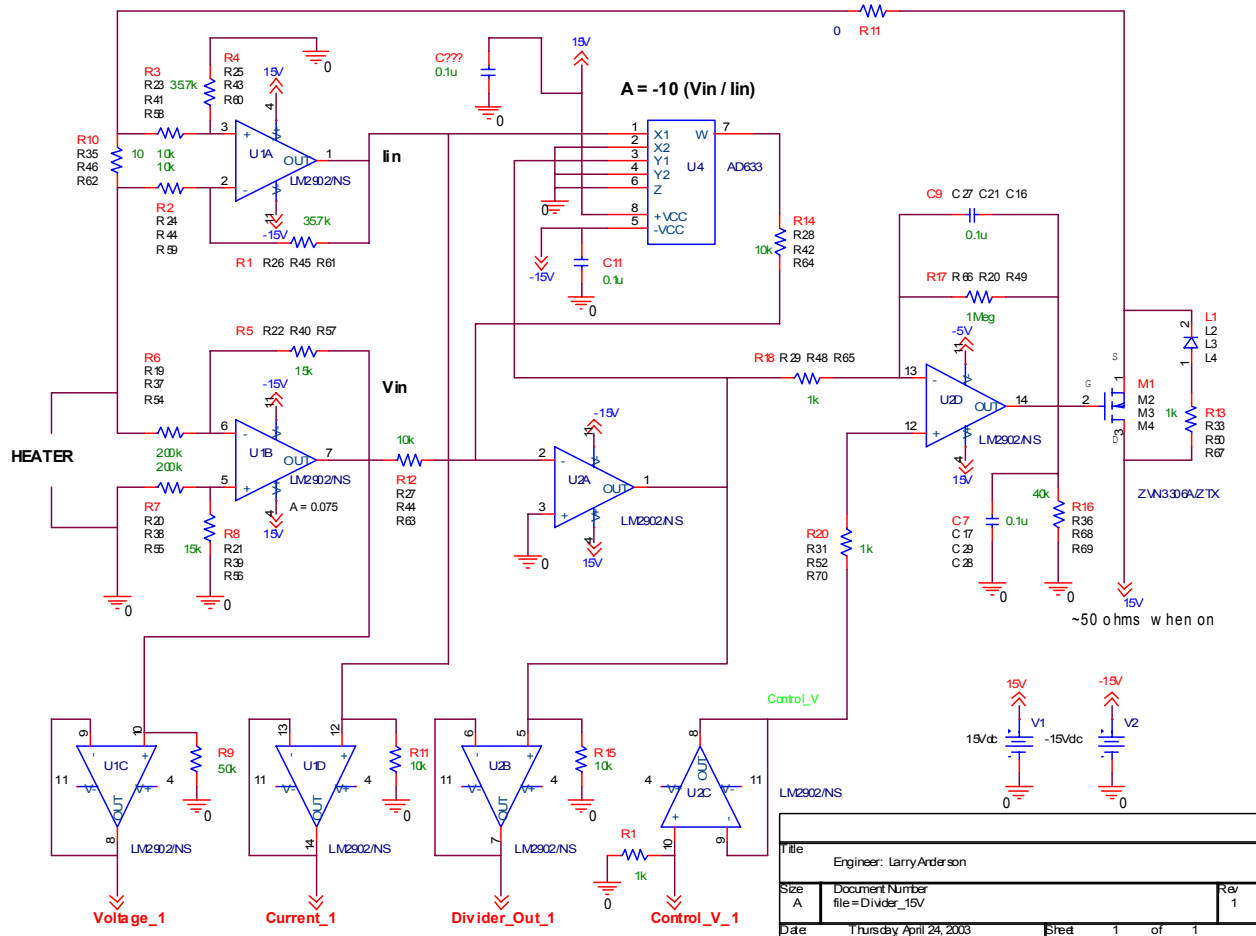


Figure 2-11. Buffered control circuit.

2.3.1.3 Gas Delivery and Data Acquisition System

To evaluate the performance of the LHV sensor in the presence of natural gas (NG) mixes, the system shown in Figure 2-12 was developed. The test fixture with dual LHV sensors, referred to in Section 2.3.1.1, is the focal point of the system and provides electrical and fluidic contact with the LHV sensors. The fixture provides electrical connection to the constant-resistance control circuit(s), a gas inlet to allow fuel/air mixtures to enter, and an exhaust to remove combustion products and unspent fuel. In initial testing two individual control circuits of the kind shown in Figure 2-10 were used to control one LHV sensor pair. Recently, the apparatus was improved so that the buffered dual circuit of Figure 2-11 could be used to control both devices. The proportional voltage and proportional current from both devices are routed to the multiplexer (MUX)—HP 34970A—so that the temperature and power of the devices during operation can be calculated and stored in the attached personal computer. Set-point voltages to set the temperature on each device were delivered to the control circuit by the MUX.

A bed of mass flow controllers (MFCs) was attached to a gas manifold, which was connected to the test fixture. Quick disconnects were installed on the MFC inlets to allow rapid change-out of gas bottles. One-way valves, flame arrestors, and excess flow valves were installed on the combustible gases for safety. One MFC was dedicated to metering “house air,” filtered through Dryright, to provide an oxidizer to the test fixture. Each MFC was calibrated using a true

Final Report

volumetric flow meter (Gilibrator, Gillian Instruments); MFC voltage versus flow rate was measured and recorded. These voltages were then chosen in the computer control system and delivered to the MFC by the MUX during testing; return voltages from the MFCs, for feedback control, were routed back to the computer through the MUX. To simulate a variety of NG fuels, tanks of pure methane, ethane, and propane were tested at first. Later, four premixed NG calibration standard bottles were purchased to generate calibration curves for the LHV sensor. Table 2-1 lists the composition of these cylinders.

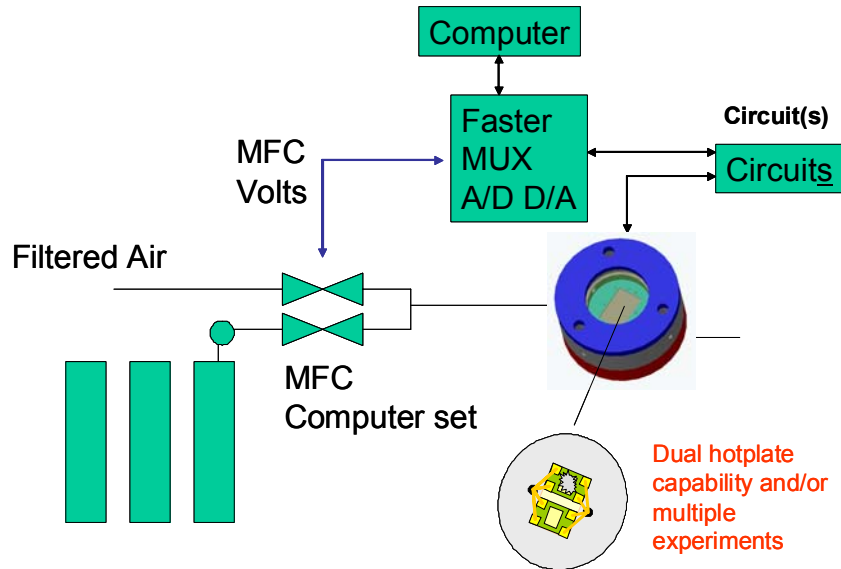


Figure 2-12. Schematic of test setup.

Table 2-1. Composition of Natural Gas Standards

Component (mole percent)	GPA Standard	Calorimetric Standard	High Ethane Standard	Helium-Enriched Standard
Helium	0.50	-	-	2.00
Nitrogen	5.00	2.50	9.00	1.60
Carbon Dioxide	1.00	3.00	0.50	0.20
Methane	70.50	88.73	64.00	88.90
Ethane	9.00	3.50	12.50	3.00
Propane	6.00	1.00	7.00	1.70
Isobutane	3.00	0.40	3.00	1.00
n-Butane	3.00	0.40	3.00	1.00
Isopentane	1.00	0.15	0.50	0.30
n-Pentane	1.00	0.15	0.50	0.30
Neopentane	-	0.10	-	-
n-Hexane	-	0.05	-	-
n-Heptane	-	0.02	-	-
Btu/Ft ³ .	1298	1028	1282.2	1083

Final Report

2.3.1.4 Testing Protocols

The following conditions pertain to the data presented in Sections 2.4.1 to 2.4.4. In initial testing, the test sequence alternated between air only and air plus fuel at regular intervals. The fuels used in the initial tests were methane, ethane, propane, natural gas, and sometimes hydrogen. The total flow rate increased due to the addition of the fuel during the sensor challenges. Since the LHV sensor is flow sensitive, the effects of variable flow had to be corrected for in the data analysis routines. Concentrations of 0.8-40% of the total inlet gas composition, at inlet flow rates of 5-40 ml/min (0.305-2.44 in³/min) were tested. The temperature of the LHV sensor was set by the constant-resistance control circuit, and ranged from 83-600°C (181-1112°F) in these initial tests.

The following conditions pertain specifically to the data of Section 2.4.5. Recently, the test sequence itself was altered to permit total constant flow throughout a test run. The air flow rate was decreased during fuel/air challenges to exactly compensate for the addition of fuel flow. Natural gas cylinders, shown in Table 2-1, were tested exclusively. Total flow rates varied from 20-40 ml/min (1.22-2.44 in³/min) and concentrations tested were principally between 7 and 43%.

2.4 RESULTS AND DISCUSSION

2.4.1 Delta Plots

Figure 2-13 shows the base response of a Pt-catalyst-coated LHV sensor to ~2, 4, 5.9, and 7.7% concentrations of methane. At time 3525 sec, the air flow rate 30 ml/min (1.83 in³/min) and an operation temperature of 500°C (932°F) resulted in a baseline power of ~0.64 W (2.18 Btu/hr) provided to the sensor by the constant-resistance control circuit. At ~3575 sec, the methane MFC was switched and 2.04% of the total flow became methane. As combustion is initiated by the heated LHV sensor catalyst, the heat of combustion provides power to the heater, and in response the circuit power required to maintain constant resistance (average temperature) drops. The time response of the device itself to fuel/air changes is very rapid, on the order of milliseconds. The time required to reach a steady state power drop of roughly 0.02 W (0.068 Btu/hr), in this case, is due to the time required to completely fill the test fixture internal volume with combustible gas. At roughly 3625 seconds, the methane MFC is switched off and the LHV sensor returns to baseline power with only air flowing over the device. This procedure was repeated for the higher concentrations of methane shown in the figure. In each case the power provided by the circuit drops when the fuel MFC is switched on, allowing combustible gas to flow over the LHV sensor. As the concentration of methane increases, so does the power change from baseline. This power change from a sensor baseline is taken as the response of the LHV sensor to combustible gas mixes. The change in power or “delta” is extracted from the data and inserted into “delta plots” indicating the response of the device over a variety of conditions. Figure 2-14 shows a delta plot (or power change plot) for various LHV sensor temperatures and gas concentrations.

Final Report

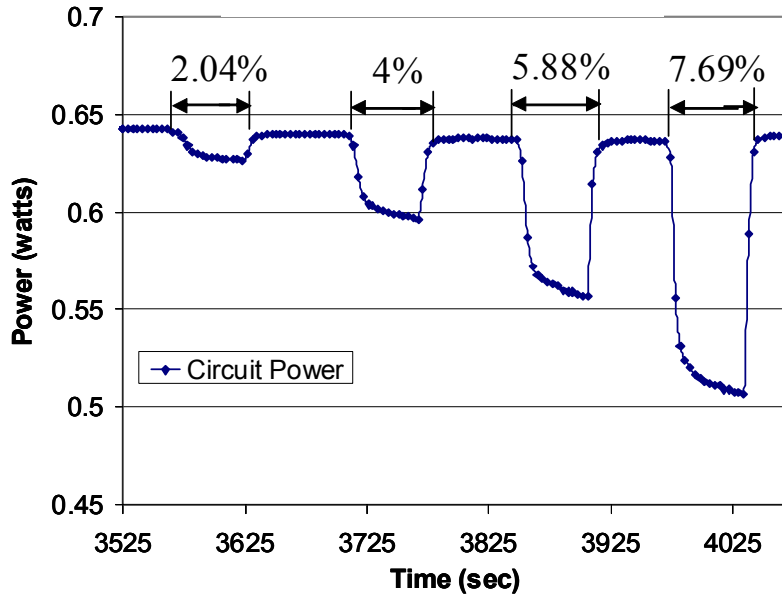


Figure 2-13. LHV sensor response.

2.4.1.1 Diverse Combustion Behavior

Figure 2-14 illustrates three distinct combustion phenomena. Between 200-400°C (392-752°F) reaction-rate limited (RRL) combustion is occurring on the surface of the LHV sensor catalyst. Mass-transfer limited (MTL) surface combustion is observed between approximately 400- 500°C (752 – 932°F). Finally, for temperatures greater than 500°C (932°F), the flame is observed to lift off the surface, taking part in a catalytically-stabilized flame. This is the first report of such diverse behavior in a microscale catalytic device. For the LHV sensor, it is likely that the MTL surface combustion is preferable because of the relative insensitivity of response to temperature variations. However, RRL surface combustion and flame liftoff could be useful operation modes for this sensor, or other catalytically-based microsensors.

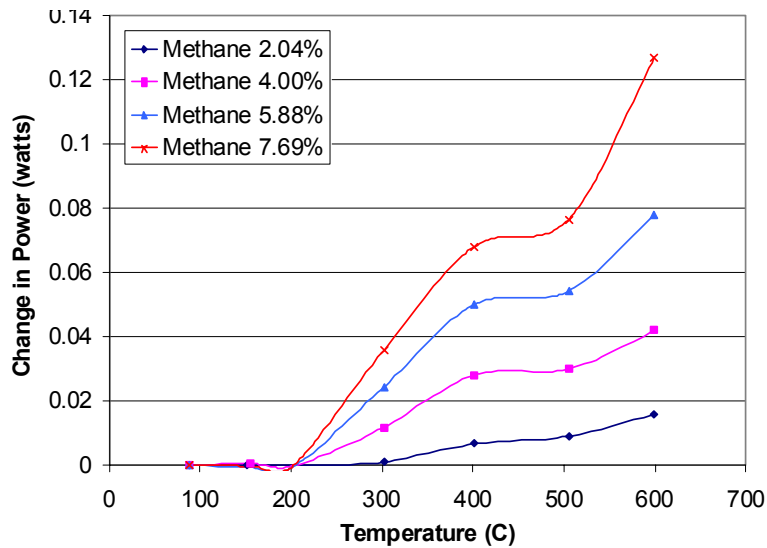


Figure 2-14. Delta plot.

Final Report

2.4.2 Speciation

The primary goal of this task was to measure the LHV of NG fuels. Of secondary interest was the determination of the relative quantities of the various components of NG mixes. If a sufficient number of the components could be identified and quantified, then the NG fuel dew point could be assessed, in addition to the LHV. It was demonstrated that by using an array of different catalysts operating at different temperatures, the relative amounts of components of the mixture could be determined. The technique is based on the fact that the various components of NG, such as methane, ethane, propane, and butane, have different combustion behaviors dependent on catalyst type and temperature (Ménil et al. 1995). In this work, the variation in combustion behavior of NG on Pt and Pd catalysts was demonstrated for a variety of conditions. The contour plots of Figure 2-15 show these results, which form the basis for speciation measurements. Ultimately it was determined that the similarity in NG fuels, and need for higher-order component analysis led to relaxation of the requirement for speciation in NG fuels with the LHV sensor. Nonetheless, the concept has been shown feasible and may have use in the future.

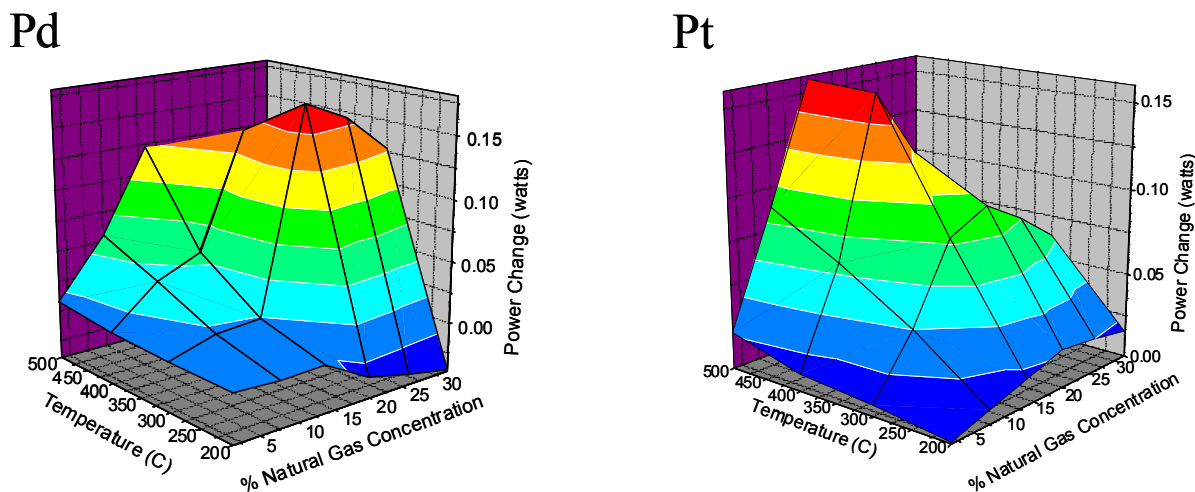


Figure 2-15. Contour plots of catalyst combustion behavior.

2.4.3 Expanded Limits of Flammability and Combustion Efficiency

In this task it was shown that the catalytic nature of the LHV sensor has benefits in terms of its range of operation. The use of catalysts on the LHV sensor expands the limits of flammability (LoF) of combustion fuels as compared with conventional flames, as shown in Table 2-2. For example, an unoptimized LoF of 1-43% for NG in air was demonstrated with the microcombustor, whereas conventionally 4-16% is observed. The LoF for hydrogen, methane, ethane, and propane are likewise expanded. It is expected that the LoF for higher-carbon-number components of NG will be expanded as well. For fuel quality measurements, expanded LoF permits reduced sensor operation temperatures, lean or rich fuel/air mixes, and low gas flows. Overall fuel-rich combustion, for example, allows higher-carbon-number components of NG to be combusted even though they are in much lower concentration than low-carbon-number components.

Final Report

Table 2-2. Catalytic versus Conventional Limits of Flammability

Hydrocarbon	Conventional Limits of Flammability	Catalytically-Stabilized Limits of Flammability
Natural Gas	4-16%	1.3-43%
Methane	5-15%	2-20%
Propane	2.1-9.5%	1-11.5%

The primary goal of the LHV sensor is the determination of the total heating value of the inlet gas. Despite the fact that the volume of the drop-in test fixture used in these experiments was too large to allow for complete combustion of all the fuel, gas combustion did occur in reasonably repeatable amounts. Table 2-3 shows that the microcombustor routinely combusted repeatable amounts of hydrocarbon, no matter what the hydrocarbon concentration was, with average efficiencies deviating by a maximum of 5%. These results likely indicate that the catalytic combustion did occur in the vicinity of the catalyst coating. In support of this view, further analysis shows that the majority of injected hydrocarbons are not combusted. Analysis shows the combustion of 15.78% methane in a gas flow of 10 ml/min (0.61 in³/min) with a microcombustor at 600°C (1112°F) produced 158 mW (539 Btu/hr). A mole of methane at room temperature and atmospheric pressure will occupy 24,290 ml (0.857 ft³) and will produce 802 kJ (760.15 Btu) when perfectly combusted. From the analysis above, this would amount to 1.578 ml/min (0.096 in³/min) of methane flowing into the fixture. Assuming perfect combustion, approximately 860 mW (2.93 Btu/hr) will be liberated. Given the signal change, of 158 mW (0.539 Btu/hr), this corresponds to only 18.37% of the total combustion energy possible being detected. Since the microcombustor was a capable temperature sensor, with a sensitivity of 0.4 mW/°C (0.0014 Btu/(hr °C)), this result showed that most of the hydrocarbons bypass the microcombustor because of the relatively large internal fixture volume. In the future, other natural gas formulations will be combusted, and the results compared with these results. If the efficiencies are truly repeatable, then the relative heating values of various fuels will be discernable. Furthermore, packaging with smaller internal volume is envisioned in the near future, which would reduce bypass effects.

Table 2-3. Combustion Efficiencies

Hydrocarbon	Catalyst	Air Flow	Percent Concentration	Average Combustion Efficiency
Natural Gas	Pt	10 cc	6.92%	15.3%
	Pd	10 cc	17.92%	10.23%
		30 cc	6.78%	7.9%
Methane	Pt	10 cc	20.0%	9.27%
		30 cc	7.69%	11.45%
Propane	Pt	10 cc	11.5%	9.18%
		30 cc	4.15%	12.7%

Final Report

2.4.4 Calibration Curves for NG at Constant Flow

As noted in Section 2.3.1.4, the test protocol was modified recently to provide total constant flow throughout a test sequence. The data discussed here was taken with constant flow. Three of the four NG cylinders of Table 2-1 were used. Total flow rate varied from 20–40 ml/min (1.22–2.44 in³/min) and most of the concentrations tested were between 15 and 20%. LHV temperature was usually controlled between 300–500°C (572–932°F). Figure 2-16 gives a delta plot showing the variation in combustion behavior for a single NG mix and two different catalyst spot sizes versus temperature. This data shows that the spot size of the catalyst has a large effect, not surprisingly, on the sensitivity of the LHV sensor. This result further bolsters the view that most combustion is occurring directly over the catalyst and response would therefore improve with reduced volume packaging.

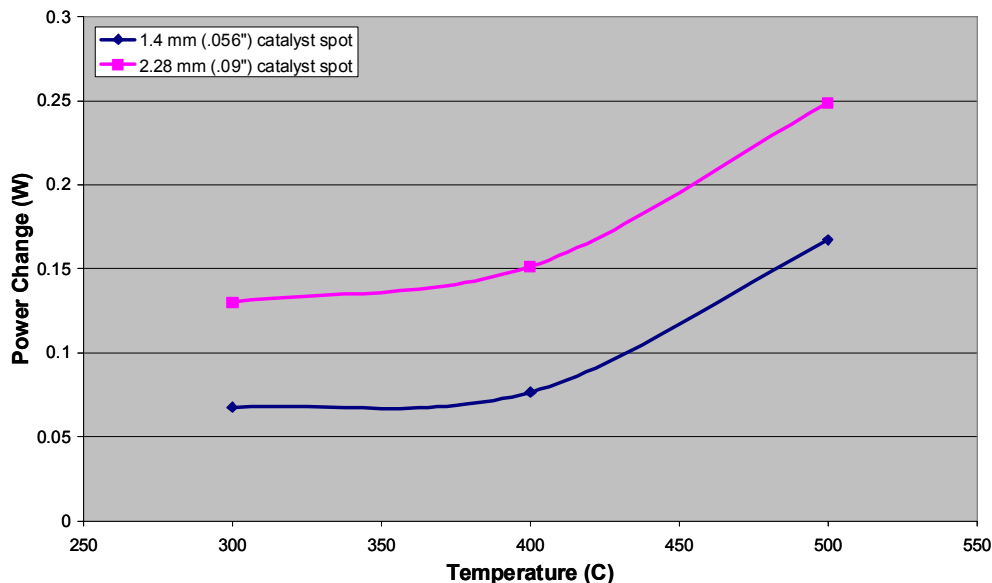


Figure 2-16. Combustion varying by catalyst spot size.

Figure 2-17 shows the performance of one device tested three consecutive times with different NG standards. The results show a signal variation with temperature, and a nonlinear correlation between Btu value and signal (i.e., a nonlinear calibration curve). Table 2-4 shows the repeatability of the device, combusting natural gas mixture 303100-U, as determined by this preliminary experiment. Experiments such as these will be the focus of on-going research.

Final Report

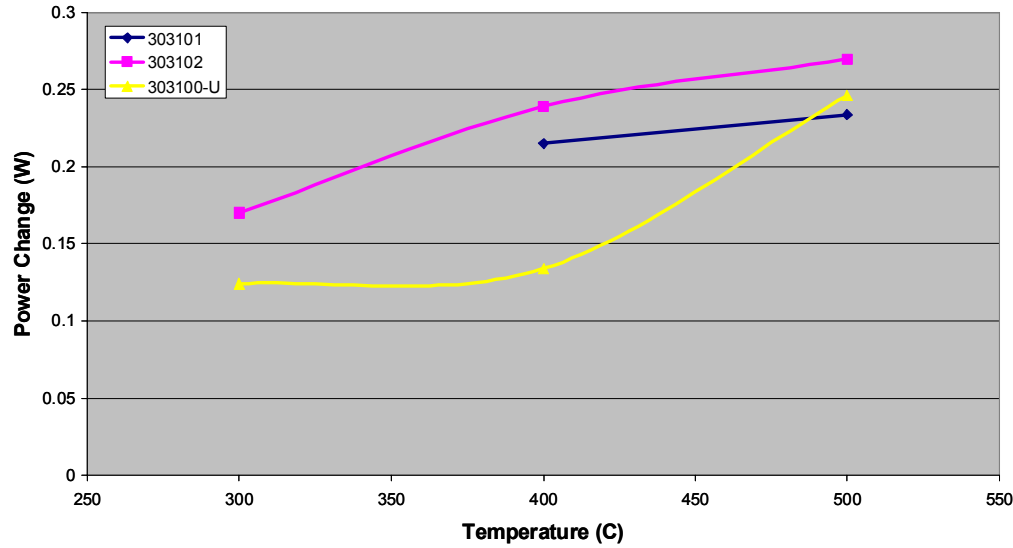


Figure 2-17. Combustion of different NG standards.

Table 2-4. Repeatability of 303100-U Combustion Signal

Temperature (C)	Standard Deviation	Average Power Change (W)
300	.009	.055
400	.009	.071
500	.021	.135

2.4.5 Validation and Combustion Modeling

To study catalyst behavior independent of the LHV sensor in a well-characterized conventional apparatus, some catalyst testing was performed in a u-tube reactor. The u-tube had an internal diameter of 4 mm (0.157 in) and the catalyst bed was held in place with quartz wool. The u-tube reactor was placed in a heating mantle and the temperature was monitored by a thermocouple placed at the top of the catalyst bed. Conversion was measured using a gas chromatograph outfitted with a thermal conductivity detector (TCD); argon was used as a carrier and reference gas. For transient temperature experiments, the temperature controller was programmed to ramp at 5°C/min (41°F/min).

Various catalysts were tested including thin films, catalyst powder, and micropen-deposited catalyst films. Figure 2-18 gives an example of the data taken with this setup for methane and propane combustion on a micropenned Pt catalyst. The data supports speciation based on catalyst temperature; propane combusts at a significantly lower temperature than methane. RRL and MTL operations are shown to be very similar to those demonstrated with the LHV sensor in Figure 2-14. Figure 2-19 compares u-tube data with data from the LHV sensor, which was

Final Report

corrected for actual catalyst surface temperature, confirming the catalyst type behavior of the LHV sensor. Figure 2-20 compares Pt and Pd catalyst response. Speciation based on Pt and Pd catalysts is evident, but Pd catalysts are seen to deactivate above 550°C (1022°F) with some recovery.

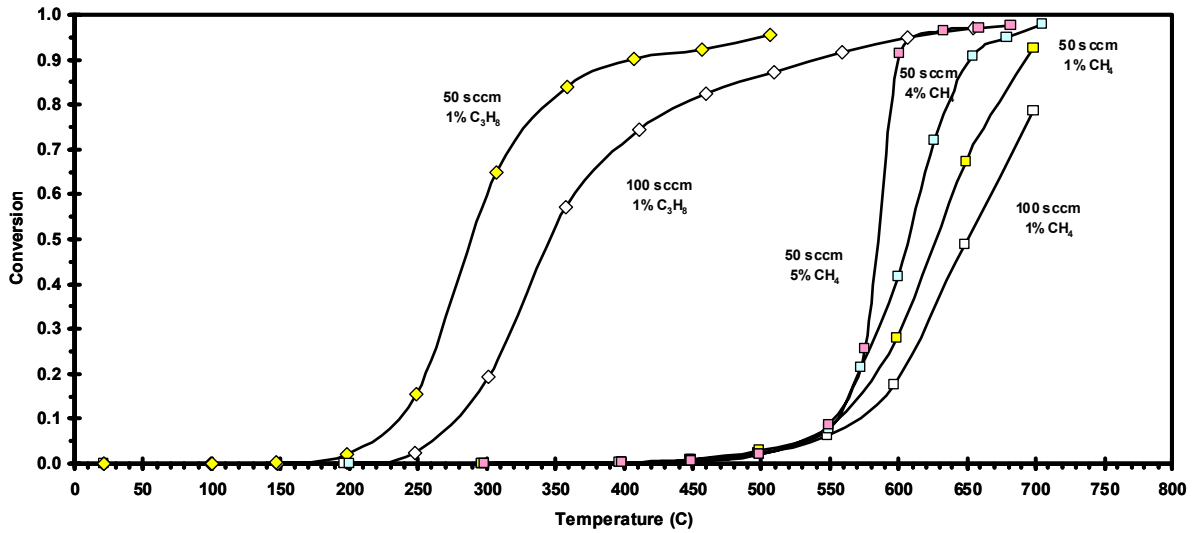


Figure 2-18. Micropenned Pt catalyst in a u-tube reactor.

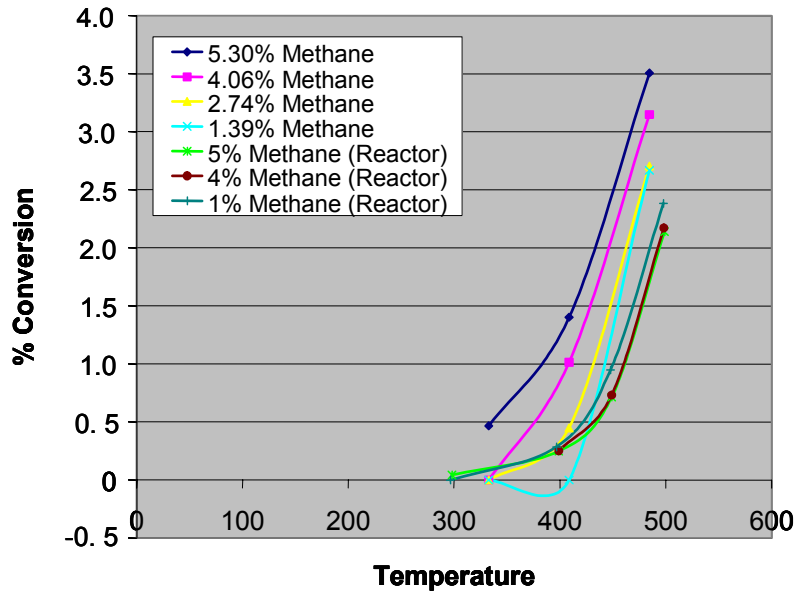


Figure 2-19. Comparison of u-tube and LHV sensor data.

Final Report

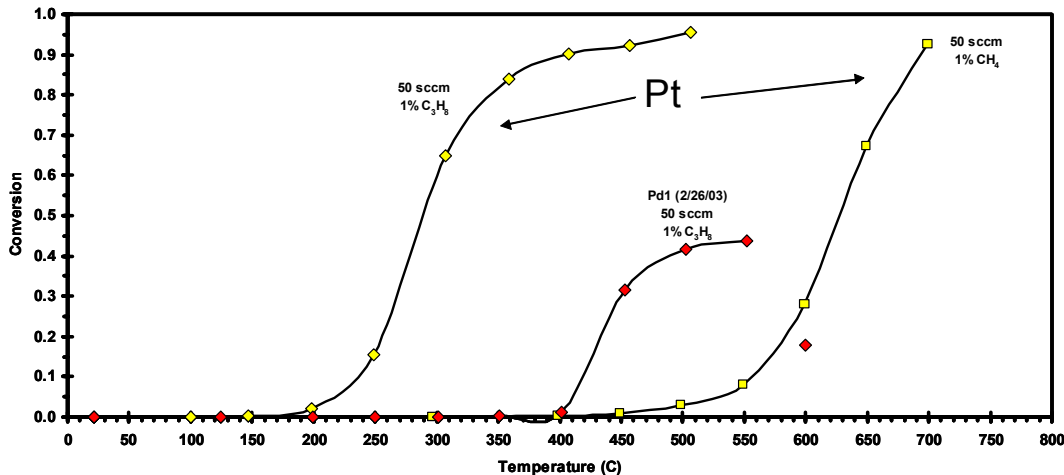


Figure 2-20. Pt and Pd catalyst comparison in u-tube.

An Agilent 3000 MicroGC was used to independently quantify the Btu content and species contained in the NG cylinder mixtures. This system contains a TCD and three columns, MolSieve, PlotQ, and OV1. The Btu and speciation analysis given in Table 2-5 compares the Agilent analysis to the analysis published by Supelco, the manufacturer. Figure 2-21 shows chromatograms taken with the PlotQ and OV1. In addition to providing an independent standard for qualifying the LHV sensor Btu response, this system should also be able to help analyze the exhaust of the LHV sensor.

Simulation of the combustion flame was undertaken, but was inconclusive. MPSalsa simulations predict ignition temperatures vastly different from those observed experimentally and, once ignition occurs, it rapidly quenches. Thus, results to date cannot provide any insight into operation of the LHV sensor. The reaction pathway used here for hydrogen/oxygen combustion successfully predicts ignition and steady state reaction rates when used with the Chemkin[®] codes SPIN and Aurora (Zerkle et al. 2000), but not with the MPSalsa code used in this task. (Unfortunately, SPIN and Aurora cannot simulate the 2-D problem desired here.) It may be that MPSalsa is simply not the right tool for the job. MPSalsa was designed to model chemically reacting flows; however, the most successful applications have not involved highly exothermic reactions or ignition phenomena. Other groups have used commercial codes Fluent and CFDRC to model such situations successfully. Since device lifetime and experimental reliability have improved, a decision was made to delay modeling in favor of experiment, unless necessary. CFD Research Corporation, which produces the CFDRC code, has been contacted and a contract can be arranged quickly for this work if it is deemed necessary.

Final Report

Table 2-5. GC Analysis of Natural Gas Standard

	Supelco 303102 High Ethane		Our Analysis	
	mol %	Theoretical BTU	mol %	Theoretical BTU
nitrogen	9	0	8.79	0
CO2	0.5	0	0.51	0
methane	64	645.10	64.43	649.47
ethane	12.5	220.73	12.51	220.82
propane	7	175.91	7.08	177.88
butane	3	97.76	3.05	99.54
i-butane	3	97.52	3.05	99.03
pentane	0.5	20.01	0.51	20.56
i-pentane	0.5	19.97	0.51	20.56
Total	100	1277.00	100.45	1287.84
Supelco BTU value:		1282.2		1282.2
%		99.59%		100.46%

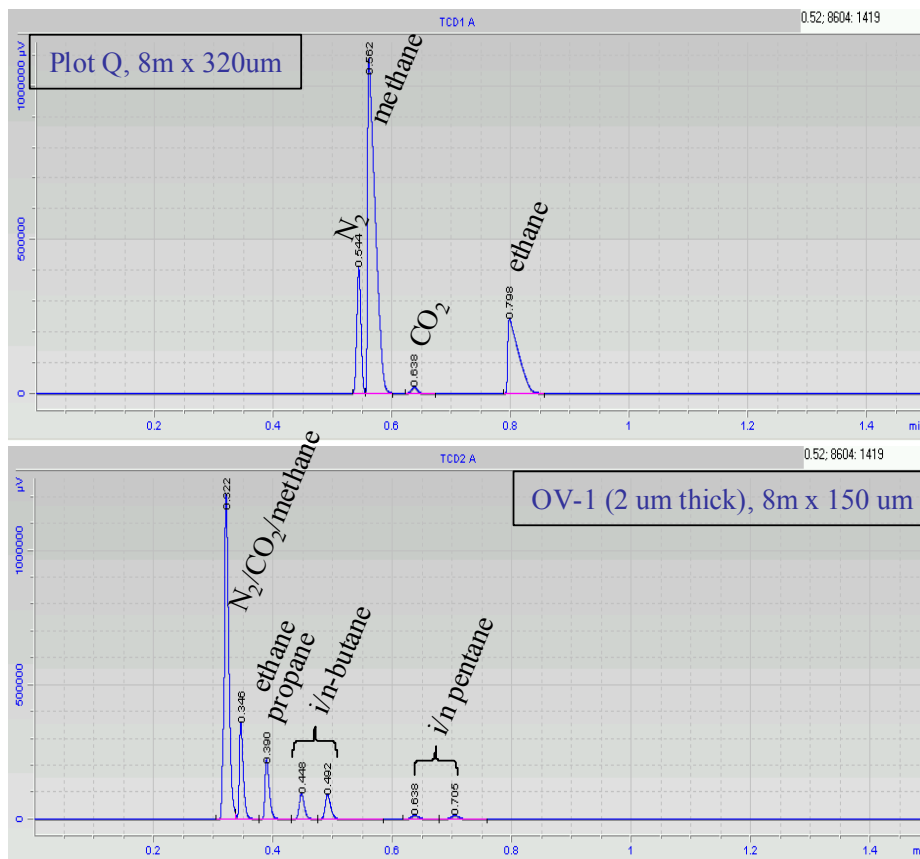


Figure 2-21. Chromatogram of natural gas.

2.5 CONCLUSION

The work reported here has shown that the LHV sensor, consisting of a catalyst film deposited on a microhotplate, is capable of performing near real-time calorimetry on combustion fuels. The

Final Report

rapid thermal response and sensitivity of this platform make it well suited to this task. Catalytic combustion on the LHV sensor exhibits a broad range of behavior, from reaction-rate-limited surface combustion to mass-transfer-limited surface combustion and gas-phase catalytically-stabilized flames. This behavior has been independently confirmed using a conventional u-tube microreactor outfitted with a gas chromatograph. This diversity of behavior will allow the sensor to operate in various useful modes and may make measurements other than calorimetric possible. Catalytic expansion of the limits of flammability is promising for operation with real fuels, where the fuel content and species concentrations vary drastically; expanded LOF will better assure more complete combustion of all components of a fuel mixture and, therefore, a more accurate Btu measurement. The concept needs to be further evaluated in future work by examining the exhaust of the LHV sensor with a gas chromatography system. It is already understood that a smaller volume combustion fixture is needed to assure more complete combustion with the LHV sensor, and a small volume fixture design will also be implemented in the near future.

Importantly, the LHV sensor appears to be capable of both heating value measurements and—if an array of LHV sensors is used—determination of some fuel mixture components. Speciation, using an array of LHV sensors, while not as important for natural gas fuels because of their relative similarity, will be very important in future work when, for example, “syn-gas” or biomass fuels are used, where there is a great diversity in both fuel Btu and species content. For a limited set of species in a mixture, the sensor array concept may work adequately. But for larger mixtures, a gas chromatograph may be needed in front of the sensor array. Sandia National Laboratories has developed a silicon-based “microGC” that will allow for rapid separation of fuels of interest. Future work will couple the microGC with the LHV sensor to evaluate this method. It should be noted that the LHV sensor, unlike a TCD, provides a true measure of the Btu content of fuels since the fuels are actually catalytically-combusted on the LHV sensor. Nonetheless, the LHV sensor, because of its thermal sensitivity, can be operated in a TCD mode as well, thereby allowing two simultaneous measurements of the heating value of combustion fuels. This is a very promising capability and will be exploited in the future.

It is clear from this work that catalysts and catalyst deposition methods are critical to the proper functioning of the LHV sensor. To some extent, the composition, the amount, and the deposition method all determine the performance of the sensor. Several methods of catalyst deposition have been evaluated in this task. Thus far, micropen has been the most successful in terms of the tolerance of deposited film dimensions. Use of this method in a research environment, however, is restricted because the micropen system’s plumbing clogs during low-volume usage; in higher volume production, this system may again be the method of choice. Other, proprietary methods currently under evaluation show promise of applicability in both research and manufacturing volume production. An investigation of these proprietary methods will be the focus of future work on catalyst deposition methods for the LHV sensor.

2.6 REFERENCES

Briand, D., S. Heimgartner, M. Leboeuf, M. Dadras, and N.F. de Rooij, “Processing influence on the reliability of platinum thin films for MEMS applications,” *MRS Symposium Proceedings*, 2002, vol. 729, pp. 63-68.

Dibbern, U., “A substrate for thin-film gas sensors in microelectronic technology,” *Sensors Actuators B*, 1990, vol. 2, pp. 63–70.

Final Report

Firebaugh, S.L., K.F. Jensen, and M.A. Schmidt, "Investigation of high-temperature degradation of platinum films with an in situ resistance measurement apparatus," *Journal Of Microelectromechanical Systems*, 1998, vol. 7, pp.128-135.

Ménil, F., C. Lucat, and H. Debéda, "The thick-film route to selective gas sensors," *Sensors and Actuators B*, 1995, vol. 25, pp. 415-20.

Neda, T., K. Nakamura, and T. Takumi, "A polysilicon flow sensor for gas flow meter," *Sensors Actuators A*, 1996, vol. 54, pp. 626-631.

Zanini, M., J.H.Visser, L. Rimai, R.E. Soltis, A. Kovalchuk, D.W. Hoffmann, E.M. Logothetis, U. Bonne, L. Brewer, O.W. Byrnum, and M.A. Richard, "Fabrication and properties of a Si-based high sensitivity microcalorimetric gas sensor," *Tech. Digest 1994 Sol.-State Sensor and Actuator Workshop*, Cleveland, 1994, pp. 176-179.

Zerkle, D.K., M.D. Allendorf, M. Wolf, and O. Deutschmann, "Understanding Homogeneous and Heterogeneous Contributions to the Platinum-Catalyzed Partial Oxidation of Ethane in a Short-Contact-Time Reactor," *J. Catal.*, 2000, vol. 196, pp. 18-39.

Final Report

3 COATING LIFE ODOMETER

3.1 INTRODUCTION

3.1.1 Condition-Based Maintenance

Overhaul and repair of gas turbines has traditionally followed a schedule-based maintenance regimen (Hoefl et al. 2003). After the recommended interval of fired hours and starts, the gas turbine is shut down for inspection and replacement of the combustor and high-pressure turbine components. The duration of maintenance outages can extend from about a week for combustion hardware to 5-6 weeks for the full high-pressure turbine rotor. For optimal turbine operation, the cost of lost power generation availability during the outage must be balanced against the maintenance costs. Repair costs increase with increasing extent of wear and damage to the parts and increase abruptly with damage severe enough to warrant parts replacement.

Of necessity, schedule-based maintenance intervals and recommended operating conditions are determined conservatively to insure a high likelihood of component survival at each inspection. They are based on a set of standard assumptions about operating conditions. Because variability in (1) expected operating environment, (2) parts geometry, and (3) material properties must be factored in, schedule-based maintenance ensures that most turbines have a substantial margin in operating conditions and time-between-outages within which they can be operated without significantly increasing maintenance costs.

A shift to condition-based maintenance (CBM), in which repair outages are determined from the measured condition of individual turbines, offers significant benefits. It allows the gas turbine owner to optimize the cost of electricity by more precisely balancing turbine efficiency and availability against maintenance cost. In a dynamic electricity generation market, it allows power producers to schedule maintenance outages based on evaluation of the price of power versus the incremental maintenance costs. It provides the necessary feedback for the optimization of operation parameters for individual turbines. The benefits to the nation are increased power availability, increased efficiency, and lower costs of electricity.

Several technical innovations are needed before full-scale implementation of condition-based maintenance is a reality:

- Measurement of the actual thermo-mechanical conditions for each part, such as temperature and strain
- Precise predictive models of the parts life, including a range of failure modes
- On-line sensing of parts degradation, such as crack initiation and growth, creep, coating oxidation, and coating erosion and spallation

This report describes a demonstration of the use of a coating life odometer as a specific element in a suite of sensors in a Smart Power Turbine that together provide the information needed for condition-based maintenance. The coating odometer is a smart thermal barrier coating (TBC) system that enables on-line sensing of coating degradation and in-situ location of TBC spalls.

The highest value components are in the hot-gas-path section of a turbine, including the first-stage stationary airfoils (nozzles) and rotating airfoils (buckets). TBCs are often used on those

Final Report

components to reduce the metal temperatures and to offer the designer an opportunity to increase efficiency, increase parts life, or reduce emissions (Nelson and Orenstein 1997). Most TBCs for industrial gas turbines are ceramic coatings made of 8 wt% yttria-stabilized-zirconia (8YSZ) deposited using an air plasma spray (APS) process. While TBCs have been used commonly to extend the life of combustion hardware for decades, only recently have TBCs been applied to the first-stage airfoils in GE's commercial gas turbines, with the introduction of the 7FA+e machine in 1999 (Gebhardt 2000).

On-line and in-situ determination of TBC health is essential for condition-based maintenance. TBC loss due to spallation, erosion, or foreign-object damage (FOD) increases local metal temperatures and decreases the service life of the airfoil. Because there is limited predictability of most TBC failure mechanisms, it is particularly important that TBC damage be detected in real time in order for condition-based maintenance to be effective.

3.1.2 Coating Odometer Design

A schematic image of the cross section of a smart TBC system using a taggant layer is shown in Figure 3-1. A tagged TBC layer (represented by the orange-colored layer) is adjacent to the bondcoat and is buried under a standard TBC layer. The tagged layer is composed of 8YSZ that has been doped with a rare earth element not normally found in the TBC or the gas turbine. The tagged layer can perform two functions: exhaust spall detection and in-situ spall location.

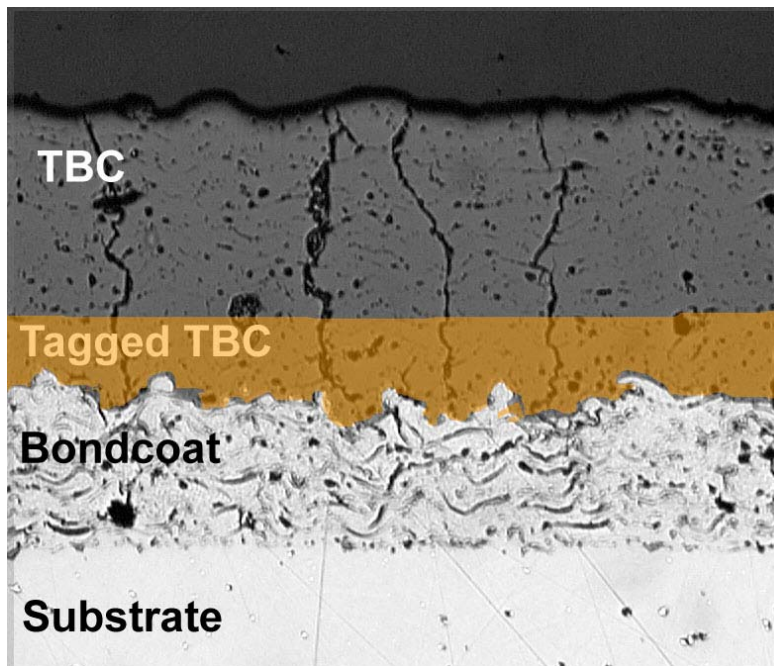


Figure 3-1. Schematic cross section of the smart TBC concept. The TBC is made of 2 layers. The outer layer is the standard TBC composition. The inner layer (colored orange in the image) has a rare earth taggant element incorporated in the TBC.

The exhaust spall detection concept is shown in the schematic drawing in Figure 3-2. In a gas turbine, the TBC comes in contact with the hot gases that expand through the high-pressure turbine to the exhaust. When the TBC spalls or erodes, TBC material is released into the exhaust stream. It would seem that a system that samples the particulate content of the exhaust stream

Final Report

should be able to detect the presence of the TBC materials— Y_2O_3 and ZrO_2 —to indicate that a spall occurred. However, TBCs are present on a great many turbine components, including the combustion liner, first-stage shrouds, first-stage rotating airfoils, first-stage stationary airfoils, second-stage rotating airfoils, and second-stage stationary airfoils. During operation, it is common for some quantity of TBC to spall or erode from some of the components. Detection of Y_2O_3 or ZrO_2 in the exhaust stream is not sufficient by itself to determine that a spall is severe enough to warrant action. However, a smart TBC system with a tagged layer near the bondcoat allows the precise nature of the damage to be inferred from the presence of taggant in the exhaust stream. Its detection confirms that a full coating breach has occurred and that bare metal is exposed to the exhaust gases. Furthermore, if each turbine component is tagged with a different taggant, the spallation can be localized and the severity of the spall can be evaluated component by component.

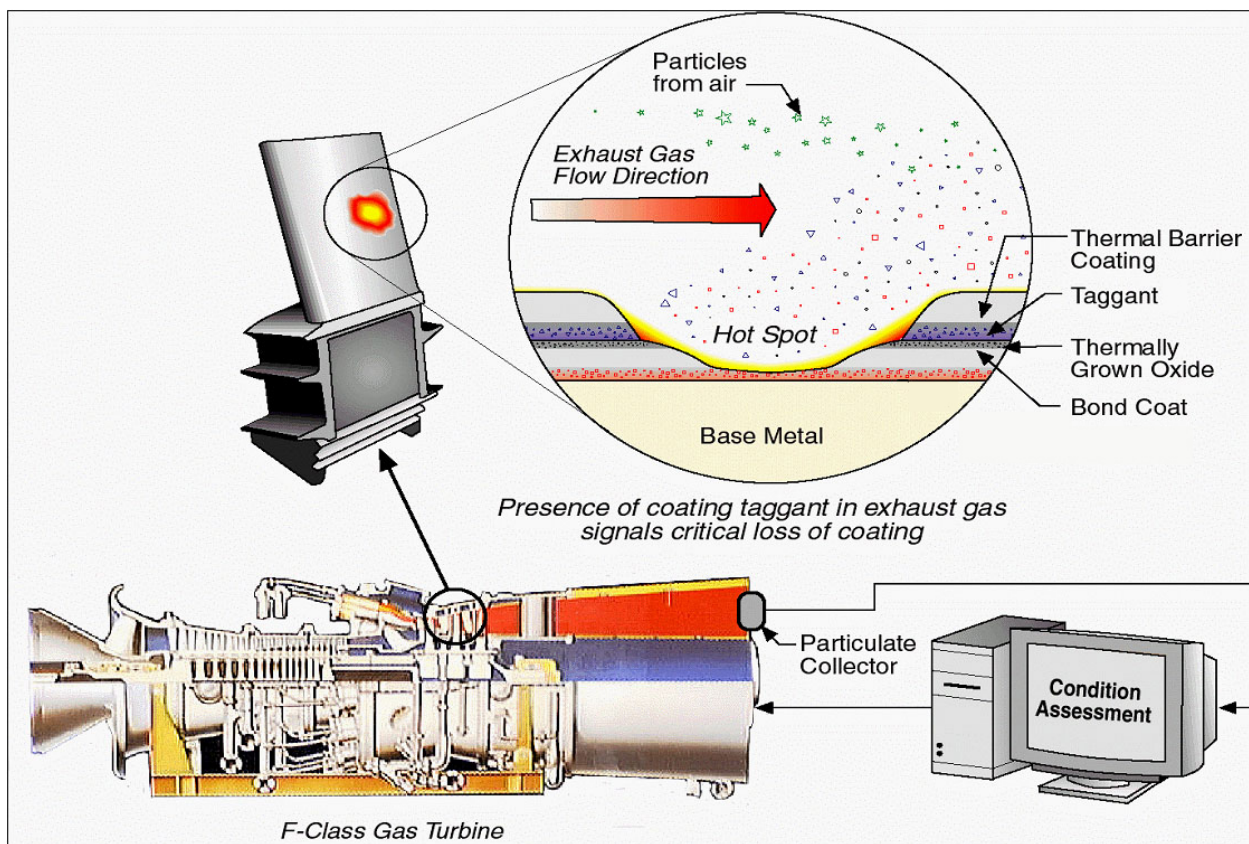


Figure 3-2. Schematic drawing of the exhaust taggant detection concept. The taggant element in the layer of TBC near the bondcoat is liberated into the exhaust stream by a failure of the TBC. Detection of the taggant in the particulate collector gives an on-line indication of coating loss.

The exhaust taggant can be used for on-line detection of a spall. However, additional information must be obtained for a condition-based maintenance decision. Turbine hardware often reaches a prescribed maintenance interval with spalls of a subcritical size or in non-critical locations on the part. The location of the spall is itself a critical piece of information. Currently, in-situ inspections of the condition of the TBC are made while the components are in the turbine and the

Final Report

turbine is shut down. These visual inspections are made through a boroscope, an optical device that has a narrow field of view and poor illumination. It is desirable for the TBC to be modified to enhance the productivity and accuracy of the in-situ inspections. The choice of a taggant element that causes the TBC to fluoresce in the presence of ultraviolet light makes it possible to determine the location of spall events or spalls more easily and precisely (Siemers and Solomon 1982). Figure 3-3 shows an image of a coupon with a fluorescent TBC layer under a standard TBC layer. Coating had been removed from the edge of the specimen and in the center of the specimen to reveal the fluorescent layer, which is orange under ultraviolet illumination.



Figure 3-3. Smart TBC coupon with fluorescent TBC layer under a standard TBC layer.

Figure 3-4 shows images of two TBC-coated coupons, one under white light illumination (Figure 3-4a) and the other under ultraviolet illumination (Figure 3-4b). The top coating was in the as-fabricated condition; the bottom coating had two large areas in which the surface layer had been removed to expose the underlying tagged layer. The exposed area is more clearly visible under ultraviolet illumination.

The conceptual design of a smart TBC system includes an indicator layer buried under a standard TBC layer. The indicator layer (1) provides a taggant element that can be detected in the exhaust stream in the event of a severe spall and (2) causes the TBC to fluoresce to allow precise location and measurement of the extent of spallation. The utility of this design was validated in two tests to determine the detection limits of the smart TBC. The risk of introducing a new TBC composition was evaluated by performing an extensive set of TBC properties tests to determine the composition range over which the taggant had no adverse effect on the TBC.

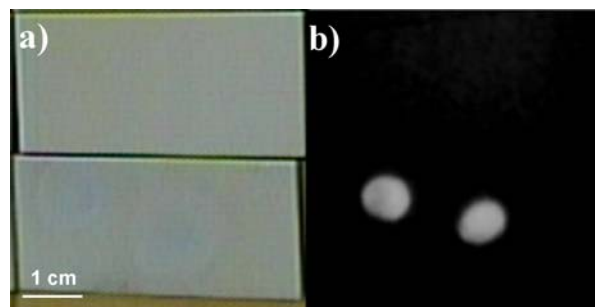


Figure 3-4. Two coupons with smart TBCs, illuminated by a) white light and b) ultraviolet light. The upper coupon is as-fabricated and the lower coupon has 2 areas with the taggant layer exposed through erosion.

Final Report

3.2 EXPERIMENTAL

Two classes of measurement systems were used to evaluate the effectiveness of the smart TBCs in both of their intended functions as coating health indicators and as thermal barriers. The coating health indicator measurements included the combustion rig exhaust detection test and the fluorescent spall detection test. Eight tests were used to evaluate the thermal and mechanical properties of the tagged TBCs: light microscopy, tensile adhesion, elastic modulus, furnace cycle test (FCT), X-ray diffraction phase analysis, Jet Engine Thermal Simulation (JETS) thermal cycle test, erosion resistance, and laser flash thermal diffusivity.

3.2.1 Coating Health Monitoring

3.2.1.1 Exhaust Detection Test

The feasibility of detecting particles in a combustion exhaust stream was determined using the combustion rig test shown in Figure 3-5. Powder samples with various amounts of a particulate taggant were injected through a powder inlet into a combustion flame running at combustion conditions simulating those in gas turbines. The exhaust stream was sampled and run through a filter. The filters were collected and the concentration of taggant element was measured using inductively-coupled-plasma mass spectrometry (ICP-MS). The minimum detectable taggant amount was determined from a comparison of the detected amount relative to filter blanks that were exposed to the exhaust stream in the absence of particle release.

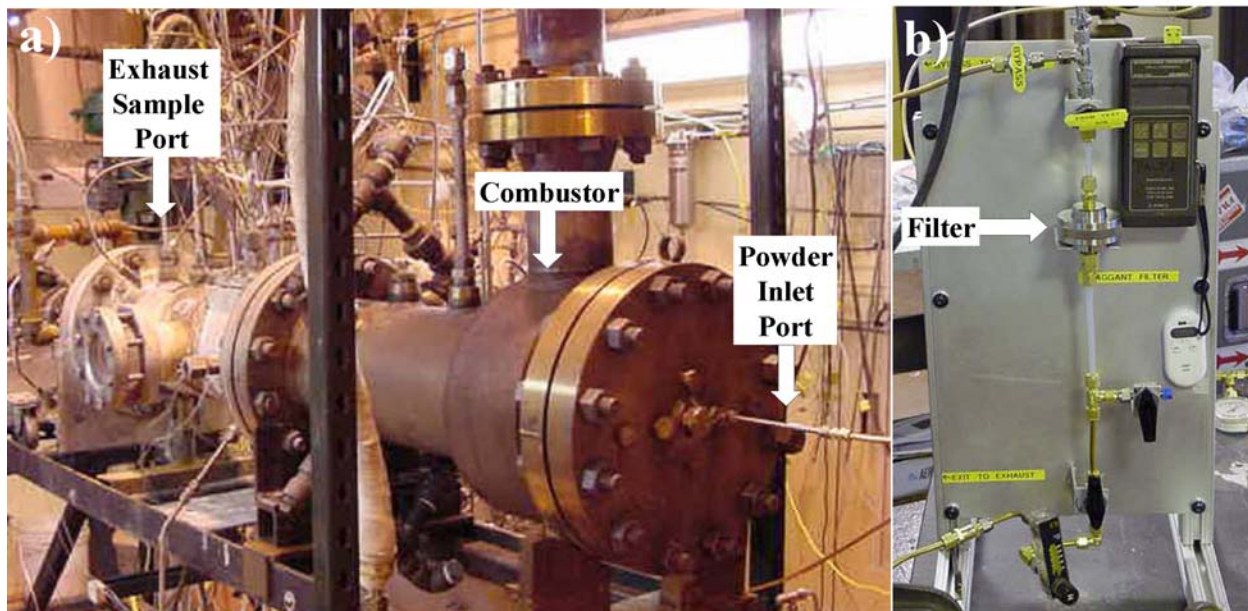


Figure 3-5. Combustion rig test for exhaust taggant detection feasibility with a combustor section in which powder was introduced into a combustion flame through the powder inlet and the exhaust was sampled into the filter apparatus through a port downstream.

Two types of ceramic powders were used in the rig test. The tagged TBC was simulated using 5 wt% Taggant-A in 8YSZ (average particle size of about 30 μm (0.0012 in) with 80% of the powder volume between 10-45 μm (0.00039-0.0018 in)), and a Taggant-B powder (average particle size of about 12 μm (0.00047 in) with 80% of the powder volume between 1.5-45 μm

Final Report

(0.000059-0.0018 in)) was used as a reference material. Copper tubes were filled with the taggant powders with loads of 0, 0.01, 0.033, 0.1, 0.333, 1, 3.3 and 10 grams (0 , 2.2×10^{-5} , 7.28×10^{-5} , 2.2×10^{-4} , 7.28×10^{-4} , 2.2×10^{-3} , 7.28×10^{-3} , 2.2×10^{-2} lb) each of Taggant-A and Taggant-B. For the powder loads below 0.333 gram (7.28×10^{-4} lb), undoped 8YSZ powder was used as a carrier powder to bring the fill weight up to at least 3 grams (6.61×10^{-3} lb) to minimize the relative loss of taggant powder along the sides of the tubes.

A nitrogen carrier gas was used to inject the powder load into the combustion flame. Presence of the powder in the flame was detected from a camera image of the flame by an increase in the radiance of the flame due to the heating of the powder. The exhaust stream was sampled through a filter. Heated lines were used to avoid water condensation at the filter. The filters were 47 mm (1.85 in) diameter, 0.2 μm (7.9 microinch) Teflon™ filters in stainless steel housings. The filters and housings were re-used between runs. Five housings were cleaned and re-used between experiments. The filters were individually bagged and labeled.

The filters were ashed in Pt dishes in a muffle furnace. The Pt dishes were pre-cleaned with boiling 20% HCl, then boiling 50% HNO₃, then rinsed with 18 M Ω water before use. Two mL of HF were added and the samples heated almost to dryness. Two mL (0.12 in³) of 50% H₂SO₄ were added and the samples heated until the solid was digested. The samples were quantitatively transferred to 50-mL (3.05 in³) centrifuge tubes and brought to 20 grams (0.044 lb) with 18 M Ω water. Several blanks were carried through the procedure. The samples were diluted for analysis by ICP-MS, which was performed using solution nebulization on a Sciex Elan 6000 instrument. The analyte concentrations were calculated by comparison with a known series of matrix-matched external calibration standards, prepared weight/weight, containing 20 parts per billion In as internal standards. Blank filters were evaluated for Taggant-A element and Taggant B element and were consistently below the detection limits of 5 ng (0.011×10^{-9} lb) and 10 ng (0.022×10^{-9} lb), respectively.

The plot of the amount of Taggant-A and Taggant-B detected as a function of the amount released is shown in Figure 3-6. For amounts below 0.333 g (7.28×10^{-4} lb) released, most of the filters did not have detectable amounts of the taggants. In two control runs in which a filter was exposed to the exhaust stream but no powder was released, detectable amounts of Taggant-A (33 ng (0.0728×10^{-9} lb)) and Taggant-B (86 ng (0.190×10^{-9} lb)) were observed. One of the control runs was the second blank run of the test. It is possible that small amounts of Taggant-A and Taggant-B were present in the materials of the test rig or in some samples of the filters. It is unlikely that the second run was affected by cross-contamination of either the rig or the filter housings since no taggant had been released before that run. For taggant amounts of 1g (0.0022 lb) and above, measurable amounts of taggant were detected in the filter for both Taggant-A and Taggant-B. The fraction of Taggant-B detected per amount released was consistently higher than the fraction for Taggant-A. It is likely that the finer particle size distribution of the Taggant-B accounted for an increase in the collection efficiency of the exhaust sampling.

Final Report

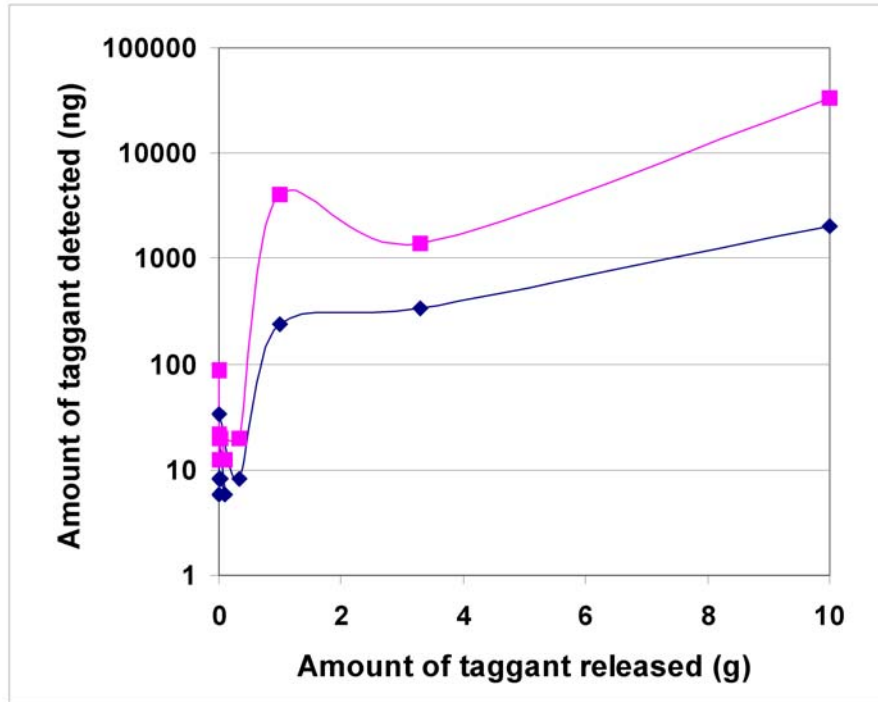


Figure 3-6. Plot of amount of taggant detected in the exhaust filter versus the amount of taggant powder released into the combustor for 2 taggant compounds, Taggant-A (blue diamonds) and Taggant-B (red squares).

A detection limit of 0.5 g (0.0011 lb) can be deduced from the data. The detection limit was used to optimize the structure and composition of the smart TBC system for detecting spalls. See Section 3.3.4, Composition Optimization.

3.2.1.2 Fluorescent Spall Test

A qualitative determination was made of the brightness of the fluorescent TBC under ultraviolet illumination similar to that which could be obtained in an in-situ inspection. A set of TBC coupons with various Taggant-A compositions was prepared. The UV light source was a compact pen light source with a 254-nm (1.0×10^{-5} in) filter that was small enough to be inserted into the turbine through an inspection port. The camera was a Pulnix model DN-007 intensified camera with a 610 nm (2.4×10^{-5} in) filter. The fluorescent images of the TBCs are given in Figure 3-7. The brightest specimens were those with 2.5 to 10 wt% Taggant-A. The dimmest specimen was the 0.5 wt% Taggant-A TBC. The 1 wt% Taggant-A-doped TBC was easily detected.

Final Report

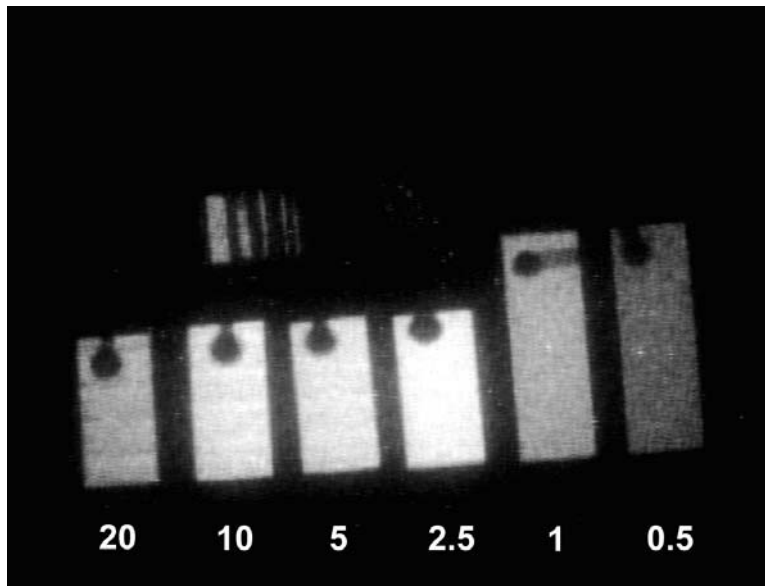


Figure 3-7. Image of fluorescence intensity of TBC coupons with a compositional range of Taggant-A in 8YSZ of between 20 wt% to 0.5 wt%, as indicated in the image below each coupon.

3.2.2 TBC Properties

The thermal and mechanical properties of the tagged TBC were evaluated to determine the composition limits over which the inclusion of the taggant did not diminish the performance of the TBC. Eight test methods were employed.

3.2.2.1 Light Microscopy

TBC microstructures were examined in cross section. Samples were vacuum-impregnated in epoxy and sectioned along the diameter. One-half of the specimen was mounted again in epoxy and abrasively polished with 180 grit SiC paper to remove the area affected by the saw cut. The specimens were polished with progressively finer sizes of diamond grit down to 1 micron (39.4 microinch).

3.2.2.2 Tensile Adhesion Strength

Tensile adhesion strength was measured for 3 samples of each type according to ASTM C-633-79. Pullrods were attached to the surfaces of the TBC and the substrate using FM1000 epoxy. Tensile load was applied at a crosshead rate of 1.0 mm/min (0.039 in/min) until the coating delaminated from the substrate. The tensile adhesion strength was determined from the size of the failed area and the maximum load at failure.

3.2.2.3 In-Plane Elastic Modulus

Free-standing TBC coupons were fabricated from sprayed plates by water-jet cutting a coupon 0.635 cm x 2.54 cm (0.25 in x 1.0 in). The TBC was released from the bondcoat by dissolving the bondcoat in a mixture of 1:1:1 HNO₃:HCl:H₂O at 70°C (158 °F). The free-standing TBC was loaded in 3-point bending at a constant displacement rate until TBC failure. The stress-strain curve was calculated from the load-deflection curve. The tangential slope of the stress-strain curve at 50% of the failure stress was calculated as the “in-plane elastic modulus.”

Final Report

3.2.2.4 FCT Life

The substrates were round buttons of René N5 that were 0.372-cm (0.146 in) thick and had a 2.54-cm (1 in) diameter. A grit-blast process was used to clean the substrate surface before coating. A Ni-22Cr-10Al-1Y bondcoat was applied by an APS process. The bondcoats were nominally 200 microns thick. TBC specimens were subjected to a cyclic, thermal treatment in the FCT. During each cycle, the specimens were inserted into a bottom-loading air furnace, and the furnace elements were ramped up to 1093°C (2000 °F) for 9 minutes. Specimens were held at 1093°C (2000 °F) for 45 minutes. The specimens were withdrawn from the furnace and forced-air-cooled for 10 minutes prior to the start of the next cycle.

3.2.2.5 Phase Stability

Phase stability of TBCs was evaluated using X-ray diffraction measurements of phase content after heat treatments of between 100-1000 hours at temperatures between 1100°C -1400°C (2012°F – 2552 °F). Specimens were 1.27 cm x 1.27 cm (0.5 in x 0.5 in) samples of free-standing TBCs. Heat treatments were performed in two types of furnaces. Heat treatments of 100 or 250 hours were performed in a bottom-loading furnace. The temperature was within 5°C (10 °F) of the set point. Samples were forced-air-cooled. Heat treatments of 500 or 1000 hours were performed in a tube furnace. Specimens were withdrawn from the furnace and cooled in ambient air.

The relative fractions of tetragonal, cubic, and monoclinic phases were determined from a Rietveld analysis of X-ray diffraction patterns measured using a synchrotron X-ray source at the National Synchrotron Light Source at Brookhaven National Laboratory. Incident radiation of 0.0185 or 0.0247 nm (0.000728 or 0.000972 microinch) was used in transmission mode through the thickness of the specimen. Unlike Cu K-alpha radiation, which is used in typical measurements, the short-radiation wavelengths allowed precise measurement of the cubic phase fraction from the spectra.

3.2.2.6 JETS Testing

Specimens evaluated using the Jet Engine Thermal Simulation (JETS) test were 2.54-cm (1 in) diameter coupons with 0.318-cm (0.125 in) thick IN718 substrates, 200- μ m (0.0079 in) thick APS NiCrAlY bondcoat and approximately 400-500 μ m (0.0157-0.0200 in) thick TBC. The samples were exposed to 20-second cycles with alternating heating and cooling. During the heating hold, a natural gas flame was directed on the TBC surface of the coupon at a preset condition designed for a 1400°C (2552 °F) surface temperature as measured using a 10-13- μ m (0.00039 – 0.00051 in) optical pyrometer. Cooling was achieved using forced air impingement on the TBC and substrate surfaces. The test was run for 2000 cycles and the TBC was examined for cracking at the perimeter of the sample or spallation within the center portion of the sample. Two specimens of each type were run.

3.2.2.7 Erosion Testing

Erosion testing was performed at room temperature on 2.54-cm (1 in) diameter TBC buttons on IN718 substrates; 50- μ m (0.002 in) alumina grit was directed at the TBC surface at 200 kPa (30 psi) pressure and 5 g/min (0.011 lb/min) feed rate through a 0.67-mm (0.0026 in) diameter orifice at a standoff distance of 7.2 mm (0.28 in) for 20 seconds. The differences in weight of the specimens before and after erosion were measured and the weight loss per minute of erosion was calculated.

Final Report

3.2.2.8 Thermal Conductivity

Thermal conductivity was measured using the laser flash method (Mogro-Campero et al. 1997). Specimens were 1.27-cm (0.5 in) diameter, free-standing TBCs nominally 15-20 μm (590-787 microinch) thick. A 2- μm (79 microinch) thick W layer was sputtered onto both surfaces of the specimens. Thermal diffusivity was measured under conditions of vacuum ($<0.1 \text{ Pa}$ (10^{-6} atm)) and nitrogen (0.10 MPa (1 atm)) at temperatures of 18°C (64°F) and 890°C (1634°F). Thermal conductivity was calculated as the product of the thermal diffusivity, density, and specific heat. Typically each conductivity measurement consisted of the average of three diffusivity measurements, and typically two specimens of each type were measured.

3.3 RESULTS

3.3.1 Taggant Identification

Three taggant elements (Taggants A, C, & D) were selected for screening because they do not appear in relative abundance in the gas turbine environment, their oxide is stable at turbine operating temperatures, they can be used safely, and they induce fluorescence in 8YSZ. The oxides were doped in 8YSZ at 0.37 mol% level (equivalent to 1 wt% for Taggant-A). Powders were synthesized in-house by a solid state diffusion method in which 99.99% Taggant-A (Stanford Materials Corp.), 99.9% Taggant-C (Aesar) and 99.9% Taggant-D (Aesar) were individually added to lots of Norton AG1 8YSZ thermal spray powder and dry mixed on a paint shaker. The powder was heated at 1550°C (2882°F) for 5 hours in an alumina crucible to diffuse the rare earth oxide into the 8YSZ. The powder agglomerates were broken up, but not ground, in a mortar and pestle, and were sieved to $-200/+325$ mesh before spraying. Coatings were deposited on IN718 substrates with a bondcoating of $200 \times 300 \text{ mm}$ ($0.0079 - 0.012 \text{ in}$) of APS NiCrAlY. For each coating composition one $10 \text{ cm} \times 10 \text{ cm} \times 0.3 \text{ cm}$ ($3.94 \text{ in} \times 3.94 \text{ in} \times 0.118 \text{ in}$) plate and four $2.54 \text{ cm} \times 0.3 \text{ cm}$ ($1.0 \text{ in} \times 0.118 \text{ in}$) buttons were sprayed. The TBC deposition conditions were held constant for all coatings and were selected to produce the dense-vertically-cracked (DVC) microstructure. TBCs sprayed with Norton AG1 8YSZ powder with no rare earth additions were fabricated at the same time for a baseline comparison.

Images of the standard 8YSZ TBC and TBCs doped with the rare earth elements under ultraviolet illumination are given in Figure 3-8. The Taggant-D dopant produced a faint yellow fluorescence. The Taggant-A fluorescence was the brightest with an orange color and the Taggant-C fluorescence was an intermediate-intensity green. Three TBC properties were evaluated in a screening mode to determine whether the taggant additions caused a detrimental effect on the TBC. The microstructure was examined, and all TBCs had a dense-vertically-cracked microstructure. Analyses of variance (ANOVAs) for the tensile adhesion strength and furnace cycle life, as shown in Figure 3-9 and Figure 3-10, respectively, indicated that the tagged TBCs had properties similar to the baseline TBC. Taggant-A, Taggant-C, and Taggant-D were determined to be promising candidates for TBC tagging.

Final Report

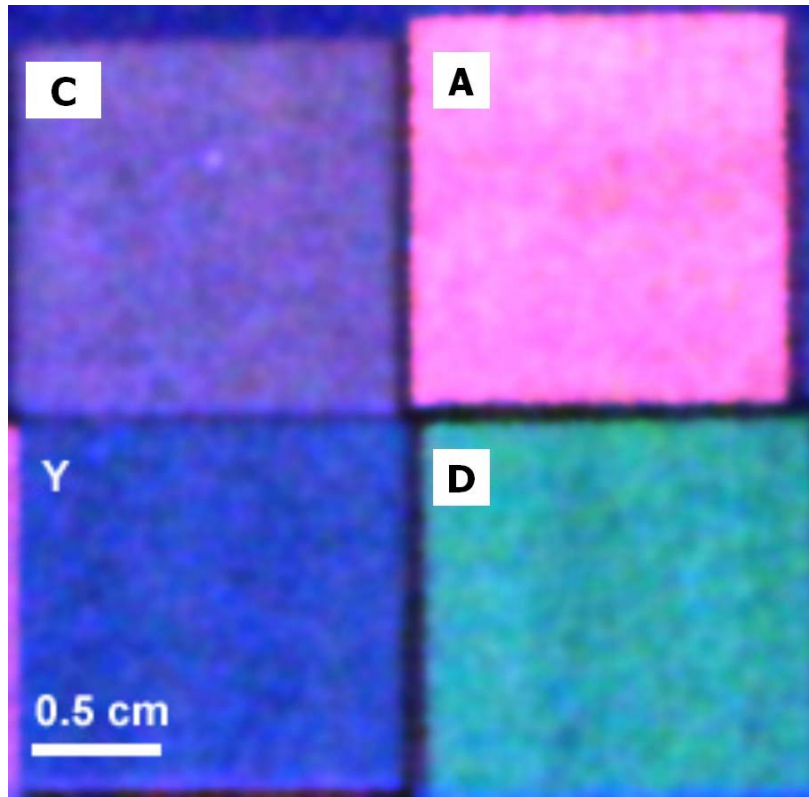


Figure 3-8. Images of standard 8YSZ TBC (Y) and 8YSZ TBCs doped with rare earth elements (Taggant-A, Taggant-C, Taggant-D) under illumination using 254 nm (1.0x10⁻⁵ in) ultraviolet light.

Analysis of Variance for Tensile Adhesion Strength (psi)					
Source	DF	SS	MS	F	P
Taggant2	3	26039	8680	0.02	0.995
Error	8	2908853	363607		
Total	11	2934893			

Individual 95% CIs For Mean Based on Pooled StDev			
Level	N	Mean	StDev
8YSZ-None	3	4136.7	1057.3
Taggant-A	3	4015.0	223.2
Taggant-C	3	4035.7	441.7
Taggant-D	3	4046.0	302.9

Pooled StDev = 603.0

Figure 3-9. ANOVA of tensile adhesion strengths of 8YSZ TBCs doped with 3 different rare earth elements compared with the baseline TBC with no taggants. Baseline data was taken for samples fabricated during the same coating campaign.

Final Report

Analysis of Variance for FCT Life (Cycles)

Source	DF	SS	MS	F	P
Taggant	3	120686	40229	0.56	0.654
Error	10	720000	72000		
Total	13	840686			

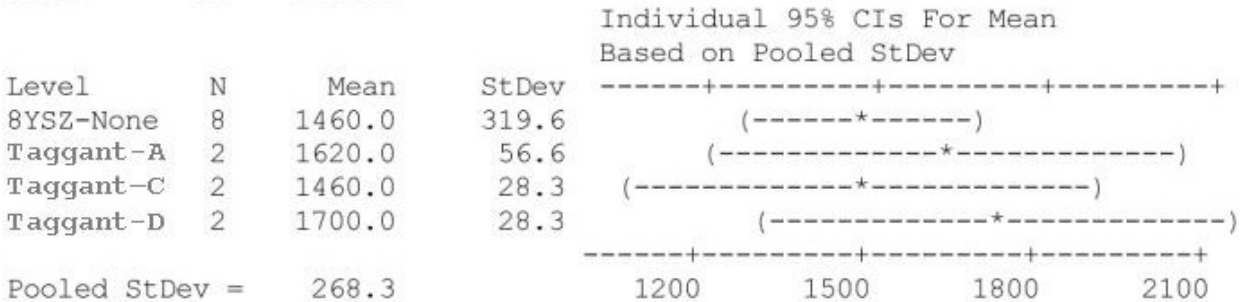


Figure 3-10. ANOVA for FCT cycles to failure for TBCs with 3 different taggant materials compared with baseline 8YSZ.

In summary, all three taggants produced measurable fluorescence, were suitable for exhaust detection, and passed the TBC properties screening. Taggant-A, with the brightest fluorescence, was selected for further optimization including detailed TBC properties testing.

3.3.2 Composition Optimization

The objective of TBC optimization was to determine the composition range over which Taggant-A could be added to 8YSZ without substantially reducing the TBC properties. Powders were obtained by two methods: solid-state diffusion (produced in-house), and fusing and crushing (supplied by the vendor Treibacher Auermet, Austria). Coatings were produced by an air plasma spray process at a common set of spray conditions for DVC TBC. Coating properties were measured including: microstructure, tensile adhesion strength, in-plane elastic modulus, FCT life, phase stability, thermal shock testing (JETS), erosion resistance, and thermal conductivity. There were three rounds of coatings that were fabricated and characterized as described in Table 3-1 as the Feasibility, Composition Screening, and Optimization coating runs.

The first set of coatings (Feasibility) was fabricated to demonstrate the feasibility of creating a Taggant-A-doped TBC. The 8YSZ thermal spray powder was pre-reacted with Taggant-A and deposited as described above. TBCs sprayed with Norton AG1 powder with no Taggant-A additions were fabricated at the same time for a baseline comparison.

Final Report

Table 3-1. Description of the 4 Taggant-A-doped 8YSZ Coating Sets Evaluated and the Methods of Powder Synthesis

Experimental Coating Set	Taggant-A dopant level(s) in 8YSZ	Powder synthesis method (vendor)	Baseline 8YSZ powder
Feasibility	5 wt%	Solid state diffusion of Taggant-A in Norton AG1 (In house)	Norton AG1
Composition Screening	0.5, 1, 2.5, 5, 10, 20 wt%	Solid state diffusion of Taggant-A in Norton AG1 (In house)	Norton AG1
Powder Synthesis Optimization	1, 5 wt%	Fused and crushed (Treibacher)	Norton AG1, Muscle Shoals

The purpose of the second set of coatings (Composition Screening) was to screen a wide range of composition of Taggant-A in 8YSZ between 0.5 wt% to 20 wt%. Powders were synthesized in house by the same solid state diffusion method as was used in the Feasibility powder set. Coatings were sprayed onto similar substrates and under similar deposition conditions. TBCs sprayed with Norton AG1 powder were fabricated at the same time for a baseline comparison.

The third set of coatings allowed a comparison of powders with two compositions similar to earlier compositions but prepared by a vendor (Treibacher, Austria) using a fusing and crushing method. ZrO₂, Y₂O₃ and Taggant-A starting powders were melted, fused, crushed, milled, and sieved to produce Taggant-A-doped 8YSZ powder with a prescribed powder size distribution. Plates and buttons were sprayed with DVC conditions as described above. TBCs sprayed with Norton AG1 powder and with Muscle Shoals powder with no Taggant-A additions were fabricated at the same time for a baseline comparison.

3.3.2.1 Microstructure

All TBCs had a DVC microstructure. Examples of the microstructures from the Optimization coating runs are given in Figure 3-11 for the Norton AG1 and Muscle Shoals 8YSZ powders and the Treibacher 1 wt% Taggant-A-8YSZ and 5 wt% Taggant-A-8YSZ powders. Using the fixed DVC plasma spray parameters, DVC microstructures were obtained for Taggant-A= compositions between 0.5–20 wt%.

Final Report

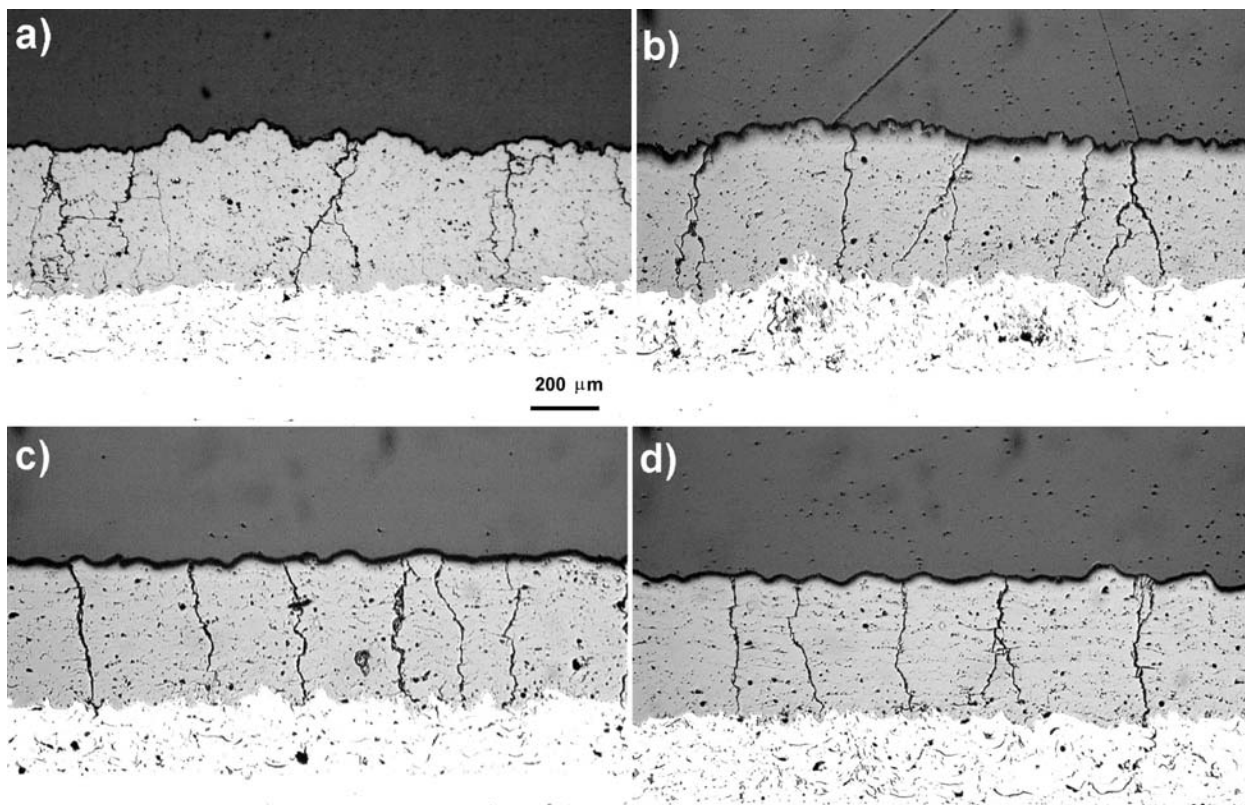


Figure 3-11. Cross-sectional microstructures of TBCs sprayed with: a) Norton AG1 8YSZ, b) Muscle Shoals 8YSZ, c) Treibacher 1.0 Taggant-A-8YSZ, and d) Treibacher 5.0 Taggant-A-8YSZ powders.

3.3.2.2 Tensile Adhesion Strength

A plot of tensile adhesion strength versus Taggant-A content is given in Figure 3-12. For the two baseline 8YSZ powders, individual measurements ranged between 29 and 44 MPa (3440 and 7320 psi), depending on the powder lot and the spray run. Within the scatter of the data, there was not a strong effect of Taggant-A content on tensile adhesion strength. TBCs with 10% or greater Taggant-A content had a statistically lower tensile adhesion strength than the baseline TBCs. However, TBCs with 5% or less Taggant-A were not statistically different from the Norton AG1 baseline TBCs as shown in the ANOVA in Figure 3-13. Values were pooled from all three coating runs. For Taggant-A contents between 0.5–5.0 wt%, there was no statistically significant effect on the tensile adhesion strength.

Final Report

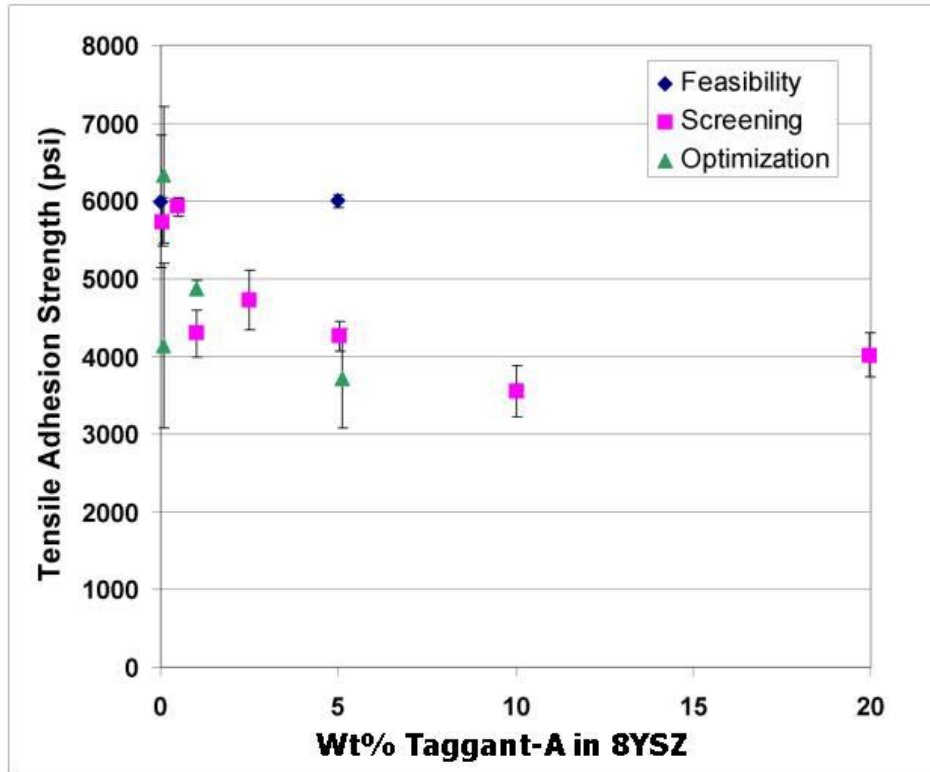


Figure 3-12. Tensile adhesion strength versus wt% of Taggant-A in 8YSZ for 3 powder coating runs.

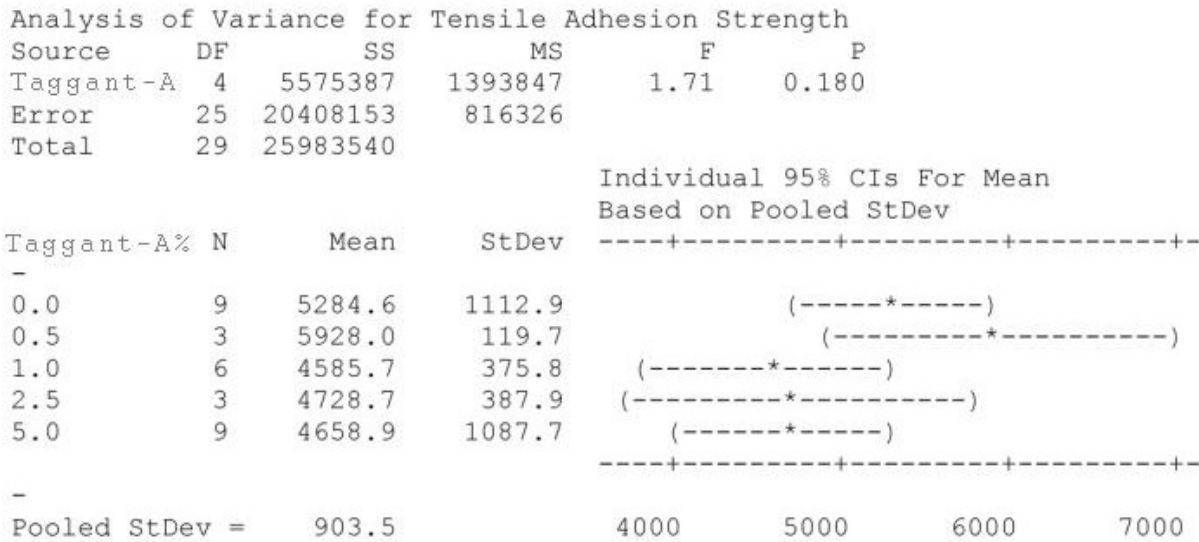


Figure 3-13. One-way ANOVA for tensile adhesion strength as a function of wt% of Taggant-A in 8YSZ. No statistically significant difference was observed.

Final Report

3.3.2.3 In-Plane Elastic Modulus

In-plane elastic modulus was measured using the 3-point bend test on free-standing TBCs. A plot of elastic modulus versus Taggant-A content is given in Figure 3-14. Although the moduli of the TBCs with 1% and 2.5% Taggant-A were statistically higher than those for the other coatings, the increase was not large enough to affect the coating quality. TBCs with all Taggant-A contents measured had acceptable elastic moduli.

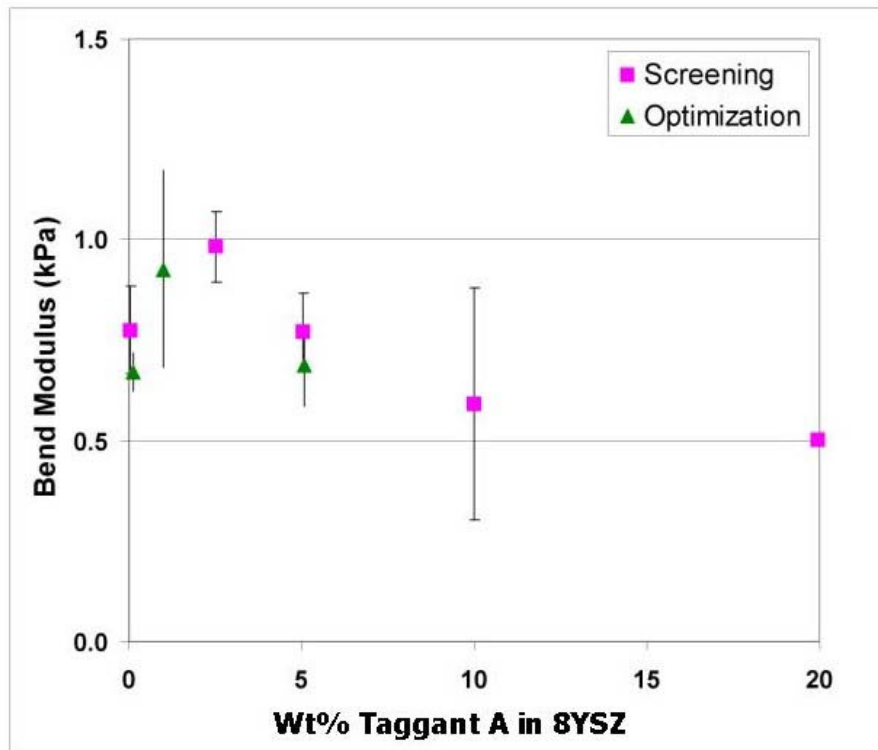


Figure 3-14. Bend modulus versus wt% Taggant-A for 2 powder coating runs. All samples had a low modulus with no effect of Taggant-A composition.

3.3.2.4 FCT Life

Furnace cycle life was measured for coatings in each of the three coating sets, and a plot of life furnace cycle versus Taggant-A composition is given in Figure 3-15. It is apparent that there is considerable scatter in the lives of the baseline 8YSZ samples both between runs and within runs. No statistically significant effect of Taggant-A composition on FCT life was observed for up to 10wt% Taggant-A-TBC.

3.3.2.5 Phase Stability

The most common material for thermal barrier coatings is partially stabilized zirconia with 7-8wt% yttria as the stabilizer. The partially stabilized zirconia is deposited as a predominantly metastable tetragonal phase. Fully stabilized zirconia of about 20wt% yttria is predominantly cubic. The partially stabilized zirconia has been shown to have better performance in burner rig cyclic exposure tests (Stecura 1978; Schulz et al. 1996). With time at temperature, the metastable tetragonal phase transforms first to the cubic phase and then ultimately to a mixture of cubic and monoclinic phase in thermodynamic equilibrium.

Final Report

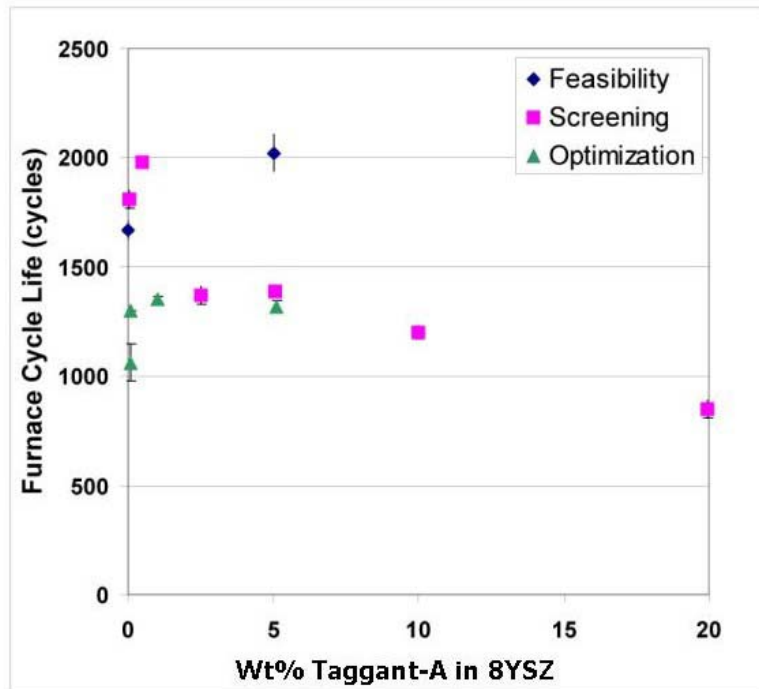


Figure 3-15. Furnace cycle life versus wt% Taggant-A for 3 powder coating runs. Given the scatter in lives of the baseline 8YSZ, there is no effect of Taggant-A between 0.5-10 wt%.

APS TBCs usually consist of almost 100% t-prime phase, that is, a high Y_2O_3 concentration tetragonal phase (>3.5 mol% $YO_{1.5}$), the “non-transformable” tetragonal phase that does not convert to monoclinic phase upon cooling. According to Scott’s phase diagram (1975), the equilibrium phase of 8 mol% $YO_{1.5}$ - ZrO_2 at $1400^\circ C$ is 50% 3.5 mol% $YO_{1.5}$ tetragonal phase and 50% 14 mol% $YO_{1.5}$ cubic phase. The low Y_2O_3 concentration tetragonal phase is transformable to monoclinic phase upon cooling. There are two reactions that occur in the production of monoclinic phase from non-transformable tetragonal phase. T-prime \rightarrow tetragonal + cubic. Tetragonal \rightarrow monoclinic. The first reaction is a diffusional transformation (Heuer and Ruhle 1984) and the second is a diffusionless, martensitic reaction (Ruhle and Heuer 1984)

Conversion of the high $YO_{1.5}$ tetragonal phase to low $YO_{1.5}$ tetragonal phase involves the loss of yttria both through the nucleation and the growth of the high $YO_{1.5}$ cubic phase and the increase in $YO_{1.5}$ content of the cubic phase (Ilavsky et al. 2001).

The addition of the taggant to the YSZ carries risks related to phase stability. There is a thermodynamic risk that the elemental addition moves the stable end product into a different distribution of phases, which can have reduced thermomechanical properties from 8YSZ.

TBCs from the Composition Screening set of specimens were aged at 1000 hours at $1400^\circ C$ ($2552^\circ F$), where complete conversion of the tetragonal to monoclinic and cubic phases was observed, suggesting that thermodynamic equilibrium had been reached. A plot of the phase fraction of cubic and monoclinic phases as a function of Taggant-A percentage is given in Figure 3-16. With increasing amounts of Taggant-A, the fraction of cubic phase increased up to

Final Report

95% for 20% Taggant-A. That increase shows that the phase field of cubic and tetragonal is quite wide for Taggant-A additions in yttria-stabilized zirconia. There is evidence that fully stabilized yttria-stabilized zirconia TBCs have less spall resistance in thermal shock testing (Stecura 1978; Schulz 2000). Yttria compositions of 11.5wt% had reduced thermal cycle life (Stecura 1978). High levels of Taggant-A additions could have a similar effect. However, no change in the phase content was observed for up to 1 wt% Taggant-A additions. Additions of 2.5wt,% Taggant-A increased the cubic phase content up to 68%, which is greater than the cubic phase for 8YSZ. There is no clear upper limit on the amount of cubic phase allowable.

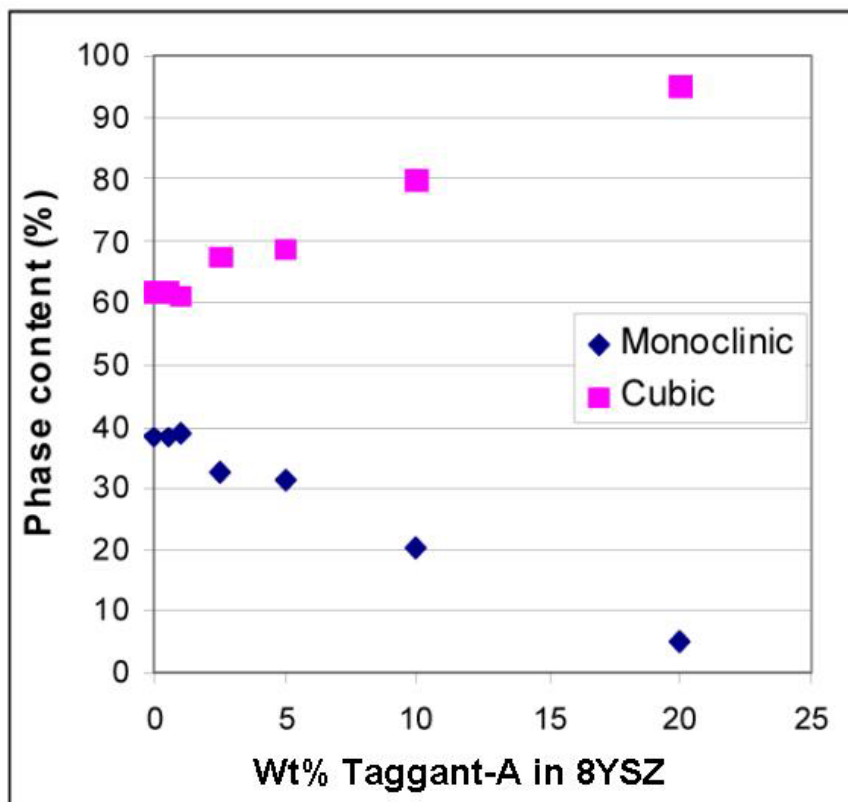


Figure 3-16. Monoclinic and cubic phase contents of TBCs as a function of % Taggant-A after a heat treatment of 1000 hours at 1400°C (2552 °F).

3.3.2.6 JETS testing

Two samples of each of the four TBCs in the Optimization spray run were tested under standard JETS conditions to evaluate thermal shock resistance. None of the eight specimens exhibited visible degradation during the JETS testing. All TBCs with Taggant-A content between 1 and 5 wt% passed the JETS test.

3.3.2.7 Erosion testing

The relative erosion resistance of the four TBCs fabricated during the optimization spray run was measured after the JETS testing, and the mass loss per unit time of erosion is given in Figure 3-17. The two undoped TBCs had similar erosion resistance, but there appeared to be a trend of increasing mass loss rate with increasing Taggant-A content. At 1% Taggant-A level, the erosion resistance was 50% less than that of the baseline TBC.

Final Report

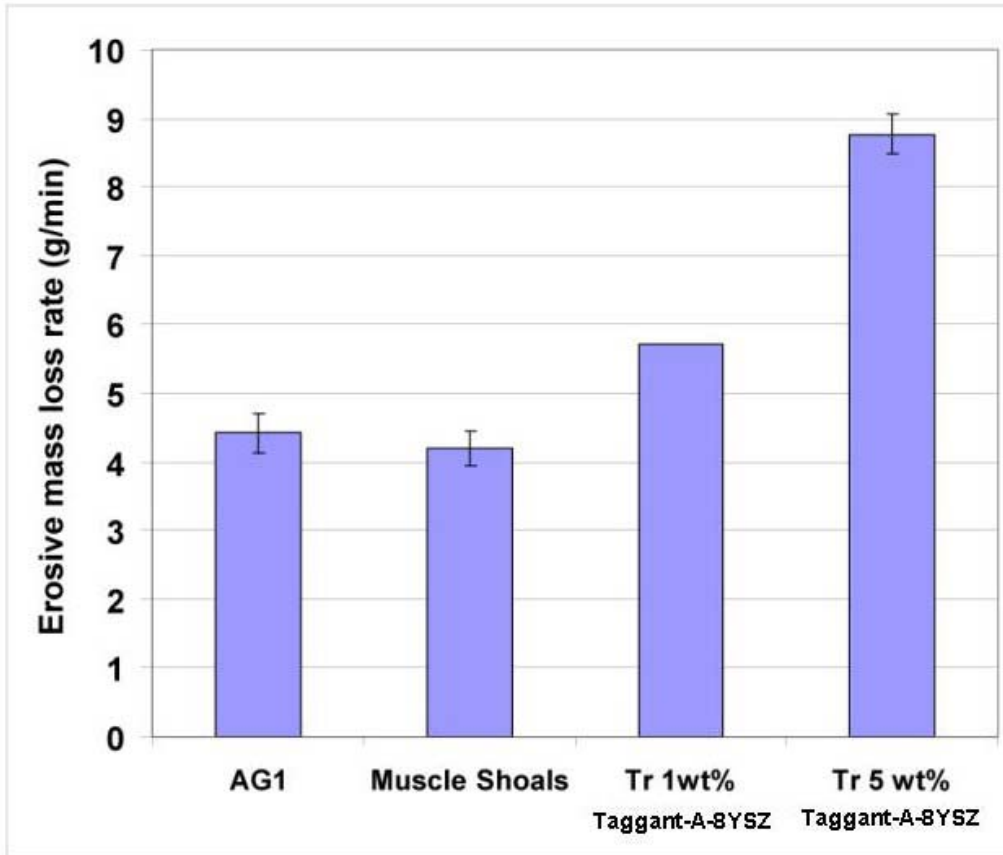


Figure 3-17. Mass loss rate during erosion test for the 4 optimization TBCs after JETS test exposure. TBCs with Taggant-A had a higher mass loss rate and lower erosion resistance than the 8YSZ TBCs.

3.3.2.8 Thermal conductivity

Thermal conductivity was measured for the four TBCs from the optimization spray run; the results are given in Table 3-2. Most of the samples showed similar trends with the measurement conditions. The thermal conductivity in nitrogen was lower at 890°C (1634°F) than at 18°C (64°F), and the thermal conductivity in vacuum was the same at both temperatures. The lower thermal conductivity at elevated temperature in nitrogen is due to the reduced thermal conductivity of nitrogen at elevated temperature in the narrow interlamellar cracks in the TBC microstructure (McPherson, 1984). The similar thermal conductivity in vacuum indicates that the thermal conductivity of the solid phase is relatively temperature independent. The 5% Taggant-A-8YSZ TBC specimen showed trends opposite those of the other three samples, but it also had the largest scatter in the measurement.

It is apparent from the wide spread in the values of the thermal conductivity between specimens that there is no statistically significant effect of the dopant level on the thermal conductivity. The bulk density values of the four specimens were similar. The conductivity is likely dominated by microstructural features such as horizontal crack density.

Final Report

Table 3-2. Density and Thermal Conductivity of 2 Baseline 8YSZ TBCs and 2 Taggant-A-doped 8YSZ TBCs. Thermal conductivity measured at 2 temperatures and under 2 gas atmospheres.

	Density (g/cm ³) (lb/in ³)	Thermal conductivity (W/m-K) (Btu/h-ft-°F) in Nitrogen		Thermal conductivity (W/m-K) (Btu/h-ft-°F) in Vacuum	
		18°C (64 °F)	890°C (1634 °F)	18°C (64 °F)	890°C (1634 °F)
8YSZ	5.56 ± 0.10 (0.201 ± 0.004)	1.63 ± 0.01 (0.942 ± 0.006)	1.50 ± 0.02 (0.867 ± 0.012)	1.46 ± 0.04 (0.844 ± 0.023)	1.43 ± 0.01 (0.826 ± 0.006)
Muscle Shoals 8YSZ	5.76 ± 0.05 (0.208 ± 0.002)	1.80 ± 0.04 (1.04 ± 0.02)	1.73 ± 0.00 (1.00 ± 0.00)	1.68 ± 0.01 (0.970 ± 0.006)	1.70 ± 0.04 (0.982 ± 0.023)
Treibacher 1% AAA-8YSZ	5.66 ± 0.10 (0.204 ± 0.004)	1.86 ± 0.01 (1.07 ± 0.01)	1.79 ± 0.02 (1.03 ± 0.01)	1.73 ± 0.04 (1.00 ± 0.02)	1.76 ± 0.02 (1.02 ± 0.01)
Treibacher 5% AAA-8YSZ	5.56 ± 0.06 (0.201 ± 0.002)	1.48 ± 0.05 (0.855 ± 0.03)	1.53 ± 0.04 (0.884 ± 0.02)	1.49 ± 0.06 (0.861 ± 0.03)	1.38 ± 0.05 (0.797 ± 0.03)

3.3.3 TBC Performance

In conclusion, TBCs with compositions between 0.5 and 5.0 wt% Taggant-A in 8YSZ showed similar properties to undoped TBCs, with two exceptions. The erosion resistance appeared to be lower for Taggant-A-doped TBCs at 1 and 5 wt% compositions, and the fraction of cubic phase in fully equilibrated TBCs was higher for Taggant-A-doped TBCs with greater than 2.5 wt% composition.

3.4 DISCUSSION

Three design constraints were identified for the smart TBC system from the testing:

- 1) Exhaust rig test: Detection limit of 0.5 gram (0.0011 lb) of taggant
- 2) Fluorescent spall detection: Detection limit of 0.5wt% taggant in 8YSZ
- 3) TBC properties: Acceptable composition range between 0.5 and 5 wt% taggant in 8YSZ

The smart TBC system should be designed to detect the smallest spall area. The relationship between spalled area, A_{spall} , and the smart TBC system is given by the following equation:

Final Report

$$A_{spall} = \frac{m_{Taggant\ detected}}{t_{Tagged\ layer}\rho_{Tagged\ layer}X_{Taggant}}$$

where m is the mass of taggant in the filter, t is the thickness of the tagged layer, ρ is the density, and $X_{Taggant}$ is the weight fraction of taggant in the 8YSZ TBC. To scale up the combustion rig results to a full-scale turbine, we use an airflow scaling factor for the gas turbine that is 100 times greater than the one produced in the rig test. In a turbine system configuration in which there are 10 filter sampling tubes in the exhaust, the scale-up factor is 10x, giving a minimum detectable taggant mass of 5 grams (0.011 lb) in the turbine. The optimal configuration for maximizing the detectable spall area is a 5 wt% tagged TBC layer that is 2/3 the thickness of the entire TBC, which gives the ability to detect a 2.54 cm (1 in) diameter spall on each first-stage bucket. Improved precision can be obtained in scale-up by careful design of the exhaust sampling system and by precise determination of the baseline taggant concentrations in the turbine exhaust.

3.5 CONCLUSIONS

A smart TBC system containing a layer of tagged TBC is feasible for on-line detection of coating spallation. Three taggant elements were identified that enable accurate location and severity assessment of TBC spalls through fluorescent enhanced inspection. There is a relatively wide composition range over which the taggant can be incorporated within the TBC without significantly affecting its thermal and mechanical properties. The optimal composition is ready for transition to a test of coating performance on a pilot-scale set of turbine airfoils in an operating turbine to verify the long-term durability of the coating.

3.6 REFERENCES

ASTM Standard C-633-79, American Society for Testing and Materials, West Conshohocken, PA.

Gebhardt, E., "The F Technology Experience Story," GER3950c, GE Power Systems, Atlanta, GA, 2000.

Heuer, A.H., and M. Ruhle, "Phase transformations in ZrO₂-containing ceramics: 1, The instability of c-ZrO₂ and the resulting diffusion controlled reactions," *Advances in Ceramics*, 1984, vol. 12, pp. 1-13.

Hoefl, R., J. Janawitz, and R. Keck, "Heavy-Duty Gas Turbine Operating and Maintenance Considerations," GER-3620J, GE Energy Services, Atlanta, GA, 2003.

Ilavsky, J., J. Wallace, and J.K. Stalick, "Thermal-spray yttria-stabilized zirconia phase changes during annealing," *J. Thermal Spray Technology*, 2001, vol. 10, pp. 1185-1189.

McPherson, R. "A model for the thermal conductivity of plasma-sprayed ceramic coatings," *Thin Solid Films*, 1984, vol. 112, p.89..

Mogro-Campero, A., C.A. Johnson, P.J. Bednarczyk, R.B. Dinwiddie, and H. Wang, "Effect of gas pressure on thermal conductivity of zirconia thermal barrier coatings," *Surf. Coat. Technol.*, 1997, vols. 94-95, pp. 102-105.

Final Report

Nelson, W.A., and R. M. Orenstein, "TBC experience in land-based gas turbines," *J. Thermal Spray Technol.*, 1997, vol. 6, p. 176.

Ruhle, M., and A.H. Heuer, "Phase transformations in ZrO₂-containing ceramics: II, The martensitic reaction in t-ZrO₂," *Advances in Ceramics*, 1984, vol. 12, pp. 14-32.

Schulz, U., K. Fritscher, and M. Peters, "Thermocyclic behavior of variously stabilized EB-PVD thermal barrier coatings," Proceedings of the 1996 International Gas Turbine and Aeroengine Congress & Exhibition, 1996, 96-GT-488.

Schulz, U., "Phase Transformation in EB-PVD Yttria partially stabilized zirconia Thermal barrier coatings during annealing," *J. Am. Ceram. Soc.*, 2000, vol. 83, pp. 904-10.

Scott, H.G., "Phase relationships in the zirconia-yttria system," *J. Mater. Sci.*, 1975, vol. 10, p. 1527.

Shannon, R.D., "Revised effective ionic radii and systematic studies of interatomic distances in halides and chalcogenides," *Acta Cryst.*, 1976, vol. A32, pp. 751-767.

Siemers, P.A., and H.D. Solomon, "Method for coating a metal substrate," 1982, US4327120.

Stecura, S., "Effects of Compositional Changes on the Performance of a Thermal Barrier Coating System," 1978, NASA TM-78976.

Final Report

4 ADAPTIVE CONTROL SYSTEM

4.1 INTRODUCTION

Competition in the electricity generation market drives the optimal operation of power utility companies while meeting fluctuations in electricity prices and fuel cost. As in any kind of optimization, optimal operation of gas turbines depends on the objective under consideration. Although there are a large number of operational degrees of freedom for profit maximization of complex power generation plants, maintenance costs and availability are two of the most important factors to the gas turbine owner. For this reason, a great deal of attention is being focused on understanding the various operational modes of gas turbines and their maintenance requirements. Gas turbines parts life models have been developed by manufacturers (e.g., GE proprietary GER 3620J and GE COSMOS parts life models) for maintenance scheduling and operation suggestions. While these models are mostly empirical but nonlinear, they originate with the laws of physics and they supply operational guidelines. In such models, major factors that affect maintenance intervals and equipment life have been determined to be firing temperature, fuel type, and steam/water injection for power augmentation. For example, if a firing temperature higher than the base-load operation temperature is used for the operation of a gas turbine, higher levels of production are achieved. They are achieved, however, at the expense of the life of the equipment. For example, parts-life model GE Power Systems GER 3620J (Hoeft et al. 2003) states that for an MS 70001EA turbine each hour of operation at peak-load firing temperature (+100°F/56°C from base-load) is the same with respect to bucket parts life as six hours of operation at base-load.

In order to understand the underlying concepts and the main hurdles encountered in this task, the following specific optimization problem should be considered. It is similar to the general class of problems dealt with here. If it is known that a gas turbine has a one-year parts life remaining and it can be taken off-line for maintenance either at the end of two months or at the end of two years—depending on the way the gas turbine is operated (i.e., with base-load or peak-load or part-loading)—where does the optimum trade-off between equipment life and power production lie for generating maximum profit? Profit is obtained through the sales of electricity minus operating costs of fuel and parts life. At the end of a maintenance interval, turbine parts that completed their lives are replaced with new ones, which adds to the cost of maintenance. Thus the optimum trade-off will lie between, for example, expending the 1-year parts life of the gas turbine in 2 months by peak firing or extending the life of the turbine over a year by part-loading. The answer depends on the price of electricity as well as fuel, maintenance, and other costs during the period in question. The essential point for the formulation of the optimization problem is that a meaningful optimum for such a trade-off can only be found by considering the operation profile for future periods (a future horizon of months, years, etc.). In order to maximize the profit obtained until maintenance time, it is necessary to evaluate not only the effect of today's peak-load profile on gas turbine maintenance and revenue obtained from sales, but also the effect of future load profiles on these variables. This choice of future horizons for finding a real optimum creates a dilemma for the solution of the problem. As longer horizons are chosen for the optimization solution, better optimal solutions will be found; however increasing the horizon increases the computation burden of the optimization increases. Note that when a decision is made on the load profile (e.g., for 1 year), a decision also needs to be made about how often the load levels can be changed. If decisions are to be made every 6 hours, then the number of

Final Report

decisions (independent variables) necessary is 1 year divided into 6-hour intervals. As the horizon under consideration increases, the number of independent variables in the optimization increases. In the previous example, the independent variables would be the gas turbine load profile in each period under consideration, that is, the number of hourly load profile decisions in 1 year or 2 years, etc. As in many non-linear optimization problems, finding the optimal load profile for a future horizon is not the only challenge for an optimizer. The models (performance, cycle, parts life) provide non-linear relations between the independent variables and dependent variables. The operational constraints such as emission constraints are also nonlinear functions of independent variables. This causes a nonlinear non-convex optimization problem. That means that generally the solution of the problem will provide local optima, not a global optimum, which may not be the best answer for the user.

For solving such an optimization problem for real-time application in a power generation plant, the following main milestones were set:

1. Use of parts-life models already developed or under development, as well as cycle and performance models, to formulate the trade-off between equipment life and power production in a modular way
2. Development of an innovative algorithm to solve the formulated optimization problem with respect to firing temperature (load profile) decisions in near real-time for the real-time application
3. Analysis and demonstration of the robustness of the Adaptive Control System to uncertainties. During the program phase, the technical team concluded that the task title Supervisory/Optimizing Control System was more appropriate for this task, and that title is used interchangeably with Adaptive Control System.

The first milestone provided modular formulation of the simulation environment. All the challenges offered by this problem were met by the development of an innovative algorithm that changed the structure of the problem into a convex problem. Once the original problem has been translated into a linear optimization problem, the novel algorithm computation time only increases linearly with an increase in the number of independent variables, both for increases in the length of the horizon and for increases in the number of periods considered in the horizon. Increasing the horizon from 1 year with 6-hour decision intervals to 2 years with 6-hour intervals doubles the number of decision variables. Keeping the horizon at 1 year but reducing the decision interval from 6 hours to 3 hours also doubles the number of decision variables. However by the merit of the new formulation, the computation time for optimization will only increase linearly in both these cases. With the third milestone, sensitivity analysis of the optimization is investigated and a robust design is achieved.

4.2 MODEL AND PROBLEM FORMULATION

4.2.1 Gas Turbine Models

Models that provide MW production, emission levels, and parts life of the gas turbine are needed for the optimal calculation of trade-off between parts life and MW production in the maximization of profit subject to operational constraints. Static cycle models that provide MW production and emission levels (e.g., NO_x and CO), given ambient conditions and operating regime, are currently in use. Cycle-deck is a GE proprietary gas turbine model that provides gas

Final Report

turbine outputs such as MW production, emissions, and required fuel flow when given necessary inputs such as firing temperature and ambient temperature. Since the optimization intervals are on the order of hours, a static performance model is sufficient for the problem solution. However, if the decision intervals become seconds, then a dynamic performance model should be used because of the importance of dynamic effects.

This static performance model, a model derived from GE proprietary maintenance guidelines (Hoeft et al. 2003) and a performance degradation model that gives the degradation of the performance of the gas turbine as a function of time are combined in a Matlab platform, a widely used computational platform, for the optimization problem. A key independent variable—firing temperature at a particular time in the horizon—can be fed into models that give the level of MW production, emissions, and consumed part life. This information is then fed into the optimization algorithm to determine the optimum firing temperature profile for the next future time horizon.

4.2.2 Problem Formulation

The optimization formulation shown here can be applied to a power generation plant that operates gas turbines for producing electricity. Although the focus here is on the optimal operation of a single gas turbine running as a simple cycle application, the formulation can be extended to multiple gas turbines running simple cycle applications. The formulation can also be extended to combined cycle applications. A preliminary analysis is presented in Section 4.4.1, Optimization Formulations Applied to Combined Cycle Power Plant Operation

The following notation scheme is used in Section 4.2.2.1, Natural Formulation of the Optimization Problem:

N = Future time horizon, Number of long time periods before next inspection (weeks, months, years),

τ = time period (decision interval: resolution of future horizon, e.g., 1 hour, then we will consider future horizon N with this resolution)

T = Total number of shorter time periods before next inspection (hours, days)=*function*(N, τ) (e.g., if $N=52$ weeks, and $\tau=6$ hours, $T=52*7*24/\tau=1456$)

i = index on time periods

t_i = Firing temperature in period i

m_i = Maintenance factor in period i

$f_i = m_i \tau$ = Factored hours spent in period i

q_i = Megawatt hours (MWh) produced in period i

ω_i = NO_x produced in period i

F = Total number of factored hours left before next inspection

C^m = Maintenance cost per factored hour

C^f = Fuel cost per lb of fuel used

Final Report

F_{flow} = Fuel spent in period i

C_i^o = Other operating costs incurred in time period i

Ω_i = Limit on NO_x produced in period i

P_i = Price per MWh in period i

Prf = Profit obtained from sales revenue of electricity produced minus operational costs (fuel cost and maintenance cost for the operation of gas turbines) and fixed costs

4.2.2.1 Natural Formulation of the Optimization Problem

4.2.2.1.1 Formulation-1 : For a user-specified maintenance interval

$$\text{Maximize } Prf = \sum_{i=1}^T (P_i q_i(t_i) - C^f F_{flow}(t_i) - C^m f_i(t_i) - C_i^o)$$

With respect to t_i

Subject to

$$\sum_{i=1}^T f_i(t_i) = F$$

$$\omega_i(t_i) \leq \Omega_i \quad i = 1, \dots, T$$

Formulation-1 describes the objective function of the problem as the revenue obtained from sales of produced electricity reduced by the fuel cost of the operation and the maintenance cost of the machine in N time periods. Maintenance cost of the machine—mainly the repair or replacement cost of parts—is considered fixed. However, this maintenance cost will be realized in N time periods. N is either specified by the user or determined by the optimizer. If N is specified by the user, then the objective is to maximize profit in that time interval; if N is not specified by the user, the objective is then to find both firing temperature and a value of N that maximizes average profit obtained per interval (\$/weeks, months) as in Formulation-2

While the first constraint in Formulation-1 is a nonlinear equality constraint, specifying the limit on the factored hours that can be spent in future time horizon N , the second constraint is a nonlinear inequality constraint for the NO_x emission levels. In order to simplify the formulation notation, the factored hour constraint is taken for the limiting parts; however, additional factored hour constraints for different parts of the equipment can also be used.

4.2.2.1.2 Formulation-2 : For determining the optimal maintenance interval

$$\text{Maximize } Prf = \sum_{i=1}^T (P_i q_i(t_i) - C^f F_{flow}(t_i) - C^m f_i(t_i) - C_i^o) / N$$

With respect to t_i, N

Subject to

Final Report

$$\sum_{i=1}^T f_i(t_i) = F$$

$$\omega_i(t_i) \leq \Omega_i \quad i = 1, \dots, T$$

It should be noted that once Formulation-1 can be solved in a reasonable time, this solution can be done iteratively for different N values in Formulation-2 to find the optimum maintenance time. For that reason, the solution for Formulation 1 is explored in detail

4.2.2.2 Application of Real-Time Optimization for Process Control

Formulation-1, with independent variables chosen as firing temperature in the horizon, is a nonlinear non-convex optimization problem, which is an open field of research for efficient methodologies to solve the problem of finding a global optimum. In this task, besides the challenges of non-convex optimization, all the challenges described in Section 4.1, Introduction, also remain. To find the firing temperature profile for $N=30$ days with the assumption that the firing temperature is kept constant for $\tau=12$ -hour period, results in $T=60$ variables to be solved. A commercial nonlinear optimizer, when run on a Pentium III processor, was able to come up with a local optimum solution after approximately two days. Two-day run times are not acceptable for real-time applications. This optimization must be repeated every time new information—changes either in ambient conditions or in electricity prices in the market—arrives. The changes in the power market, electricity price forecasts, and changing ambient conditions dictate that this time period be a few hours rather than a few days. Hence, because of the computation burden, the optimization problem for maximizing the profit of a power generation plant by operating a single gas turbine (described in Section 4.2.1) cannot be solved with general nonlinear solvers on the market in a time frame of a few hours.

For optimal operation of the power generation plant, a real-time optimizer for gas turbine operation should send the optimal profiles to a controller that will achieve the desired targets or to an operator who will evaluate and implement the decisions manually. Both cases are in the framework of the Model Predictive Control paradigm, described in Section 4.2.2.3.

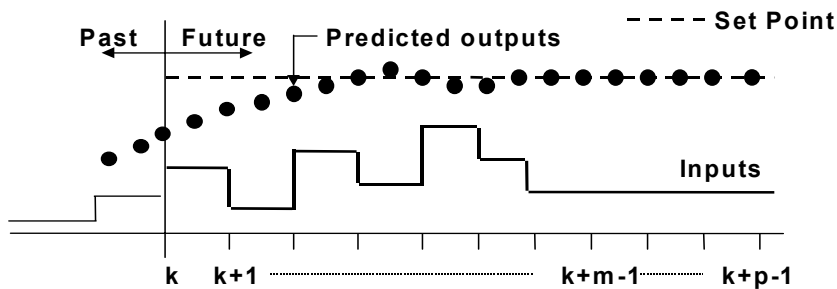
4.2.2.3 Model Predictive Control

Model Predictive Control (MPC) is a class of control algorithms that use process models to compute a sequence of manipulated variables by on-line optimization of future process behavior. The model is used to predict how the process will evolve in time, and the prediction is used to find optimal control moves that will steer the process to the desired steady state. This on-line optimization is solved at each sampling time, using the current state of the process as the initial state. Only the first control move of the optimal sequence is applied to the process. The same procedure is repeated at each sampling time. On-line optimization at each sampling time is the main difference from conventional control, which uses a pre-computed control law.

Originally developed to meet the specialized control needs of power plants and petroleum refineries, MPC technology—a new methodology for industrial process modeling and control—is now used in a wide variety of application areas including chemicals, food processing, automotive, aerospace, metallurgy, and pulp and paper. There are at present more than two thousand applications in the United States alone.

Final Report

Although the origin of MPC can be traced to the 1960s (Propoi 1963; Lee and Marcus 1967), the first applications emerged in the late 1970s in the process industry (Richalet et al. 1978; Cutler and Ramaker 1979), initiated undoubtedly because of economic incentives. It is well known that the economic operating point of a typical process unit lies at the intersection of constraints (Prett and Gillette 1980). A successful industrial controller therefore must maintain the system as close as possible to the constraints without violating them. In addition, process units are complex, nonlinear, constrained multivariable systems whose dynamic behavior changes with time as a result of changes in operating condition, catalyst aging, etc. This incentive led to the model-based control methodology in which the dynamic optimization problem is solved on-line at each control execution as shown in Figure 4-1. Process input and output constraints are included directly in the problem formulation so that future constraint violations are anticipated and prevented. In addition new process identification technology was developed to allow quick estimation of empirical linear dynamic models from test data, substantially reducing the cost of model development. An overview of industrial model predictive control technology and a history of three generations of MPC can be found in an excellent survey by Qin and Badgwell (1997, 232ff.).



At each sampling time k

1. Obtain measurements from plant
2. Using a process model, predict the process output over a horizon
3. Solve an optimization problem on-line to compute $u(k+i)$, $i=0, \dots, m$
4. Implement the first computed move $u(k)$
5. $k = k+1$

Figure 4-1. Schematic of Model Predictive Control methodology

The idea of an optimization layer on the control structure of processes is widely applied in US process industries with great success. However because of fast time constants in the power generation industry, that computation-expensive paradigm has not been used. Because of the high computation burden, the idea of combining maintenance considerations versus performance or parts life versus performance optimization was not achieved under MPC framework until the work reported here. The proposed formulation enables the upper layer optimization to be applicable in real-time, providing robustness to uncertainties and optimality for real plant conditions.

Final Report

4.3 ANALYSIS

4.3.1 The Optimizing Algorithm

The detailed description of the transformation of the optimization problem (Formulations 1 and 2) and the novel algorithm that is used to solve the problem are given in Appendix Section 4A.

4.3.1.1 Input-Output Relationship of the Algorithm

The input output relationship of the proposed optimizer is shown in Figure 4-2.

The optimizer uses performance, emission, and reliability models that can be updated either by user or sensor information. Assuming appropriate models (currently, GE proprietary models) linked to the optimizer, the user has to input

- Remaining part life for the gas turbine, F
- Future time horizon, N ,
- Limit on minimum MW production constraint and limit on NO_x emission constraint, Ω ,
- Electricity price forecast for future time horizon
- Fuel price forecast for future time horizon
- Weather forecast for future time horizon

Additional constraints for user-specific problems can be accommodated in the same framework.

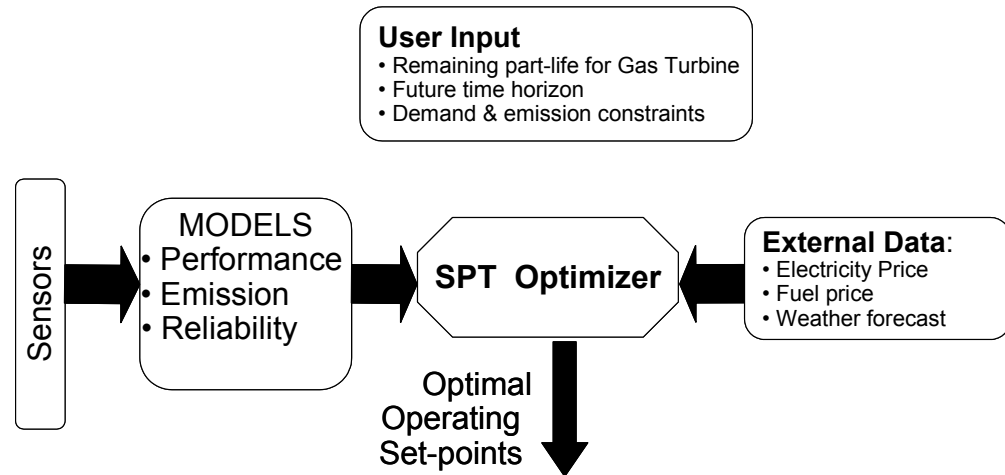


Figure 4-2. Input-output relationship of the proposed optimizer

4.3.2 Robustness Analysis

As described in Section 4.3.1, the optimizer requires some inputs from the user. N , Future horizon, C^m , Maintenance cost per factored hour, C^f , Fuel cost per lb of fuel used in each period, C_i^o , and other fixed operating costs incurred in time period i . P_i , sale Price per MWh in period I , are necessary information for the optimization. Since the optimization results depend on these inputs, the optimality of the optimization results depends on these inputs as well as the

Final Report

fidelity of the models used such as Cycle-deck and parts life models. Since the future sale prices of electricity in the spot market are not predictable for long time horizons with high fidelity, performing optimization and updating the models and forecasts at every time step would bring robustness to these uncertainties, provided that the electricity price forecasts and other changes in the system (e.g., ambient temperature and gas turbine performance) are updated with more reliable information, thus eliminating the near-term uncertainties (e.g., electricity prices and ambient temperature forecasts in the following week have more reliability than a forecast for a year ahead). For the desired robust scheme, the MPC paradigm, described in Section 4.2.2.3, is an ideal fit, because the optimization is re-applied at every time step, with up-to-date models and information used in the computation. In that way uncertainties in the information such as electricity price forecasts can be circumvented or diminished.

This approach was demonstrated in a sensitivity analysis of the optimizer by Monte-Carlo simulations on P_i , sale Price per MWh in periods i for all periods. Since the objective of the sensitivity analysis is to investigate the effect of changes in electricity prices on the optimization results—especially on changes in total profit obtained from electricity sales occurring after a load profile decision is made—Monte Carlo simulations were designed to demonstrate the effect of changes in electricity prices on total profit. To conduct Monte Carlo simulations, however, the electricity prices must be changed randomly from the electricity price forecasts, with the assumption that while electricity forecasts are able to capture the average values in the market, they are unable to predict random changes departing from those average values. That is why it was necessary to find a distribution of electricity prices in order to analyze such changes in electricity price forecasts. Two sources—a literature search on the energy derivatives pricing (Clewlow and Strickland 2000) and analysis of best fit for distributions on historical data—both show that lognormal distribution can be used for explaining electricity prices. Figure 4-3 shows the results of a distribution fit study on historical electricity price data from 1997 through 1999. Lognormal distribution is found to be the best fit for the data analyzed during this period by various methods, including a Chi-Square test and Kolmogorov-Smirnov and Anderson Darling tests. The fact that the Indicated p value is greater than 0.05 for the chosen significance level of 95% demonstrates that the hypothesis that the analyzed data comes from this distribution can be accepted with statistical certainty. The main point, however, is not to find the “real” distribution of electricity prices for all times as a general rule. That would be a very difficult task involving the many factors affecting the electricity market, and it is not within the scope of this task. The main goal was to find a statistically realistic distribution that can be used for Monte Carlo simulation in this sensitivity analysis.

Final Report

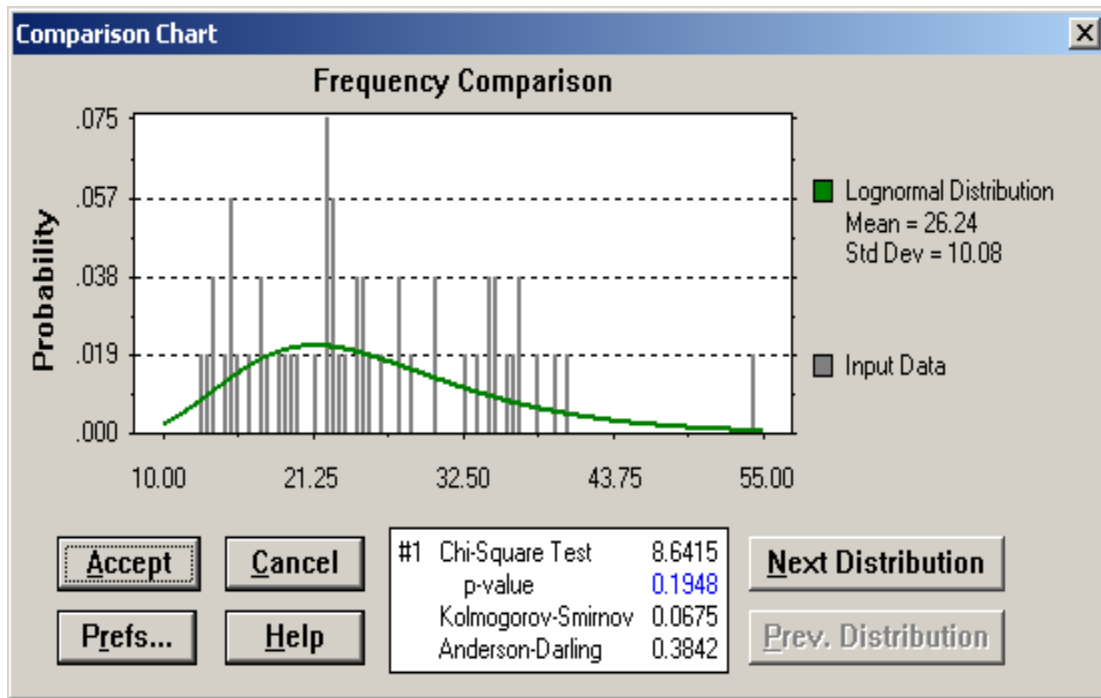


Figure 4-3. Best distribution fit to historical electricity prices during 1997-1999

Total profit obtained by electricity price sales as a function of the load profile from the current time to the maintenance time has already been formulated (Formulations 3 and 4 in Appendix Section 4A). The question of interest is, after an optimal load profile is found by the optimizer, how will the changes in electricity prices affect the total profit? This effect was investigated by Monte Carlo simulations. P_i , sale Price per MWh in periods i for all periods, are changed simultaneously according to lognormal distribution, and the total profit is evaluated with the same optimal profiles for changes in prices for all indices I , from the current time to the end of the prediction horizon of 2000 trials, resulting in a total profit distribution that will be obtained if the optimal load profile is implemented without any other optimization until the end.

Figure 4-4 demonstrates how the uncertainty of prices in the latter part of the forecast window is implemented in the Monte Carlo simulations. While keeping the average values unchanged, the standard deviation for uncertainty is implemented as a linearly increasing uncertainty with time.

Final Report

Electricity Price Forecast (\$/MWh)

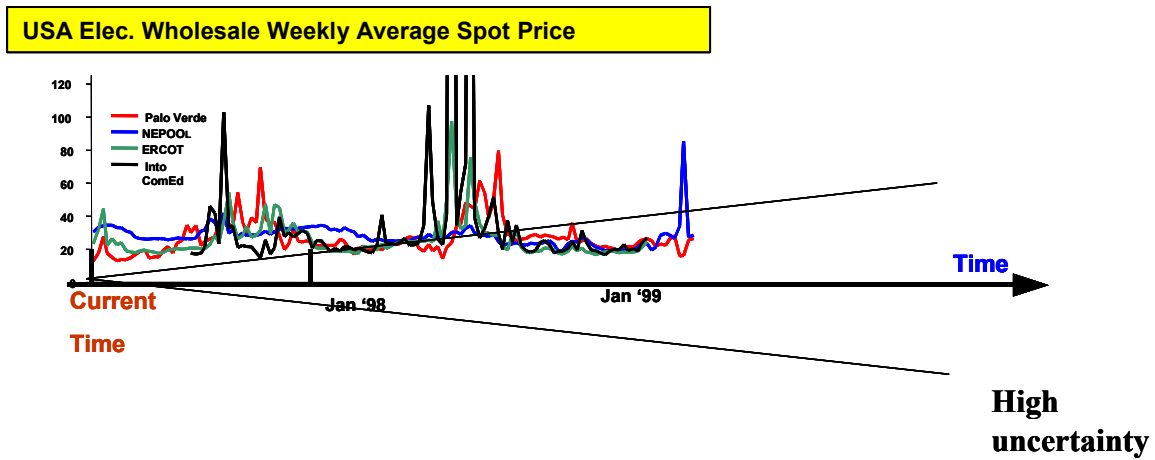


Figure 4-4. Application of growing uncertainty in electricity prices in Monte Carlo simulations.

Figure 4-5 shows the base-load profile for the firing temperature (proprietary numbers are not shown), MW, and parts-life consumption of a 7FA gas turbine that operates continuously for 1 year with decision intervals of 6-hours (at every decision interval, the gas turbine load can be changed to a desired level of operation). These values are obtained through Cycle-deck and parts-life models (Hoeft et al. 2003J).

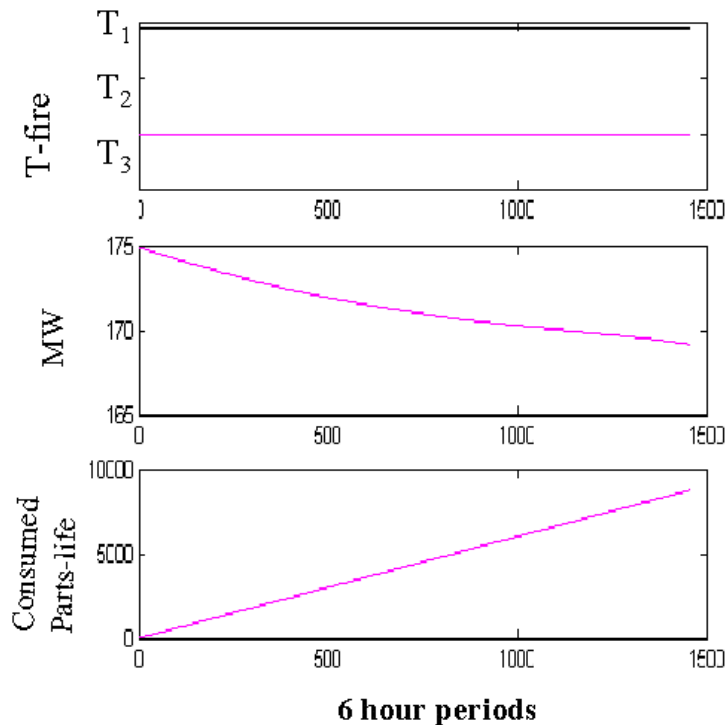


Figure 4-5. Base-load profiles.

Final Report

The corresponding total profit distribution in Figure 4-6 is obtained by evaluating the total profit formula in Monte Carlo simulations by changing electricity prices in 2000 trials. Mean profit is obtained as \$7,215,000 while the observed standard deviation, \$550,000, is the square root of the sum of individual period electricity price variances. The standard deviation, i.e., uncertainty in electricity prices, increases linearly in the simulations shown in Figure 4-4. While the standard deviation for electricity prices for the current time is kept at \$1, a \$0.5/week increase in the standard deviation is applied, resulting in the final sections of the electricity forecasts being realistically uncertain for the simulations. For a prediction horizon of 1 year, the final weeks of the horizon will see a standard deviation in electricity prices of values similar to average values of electricity price forecasts.

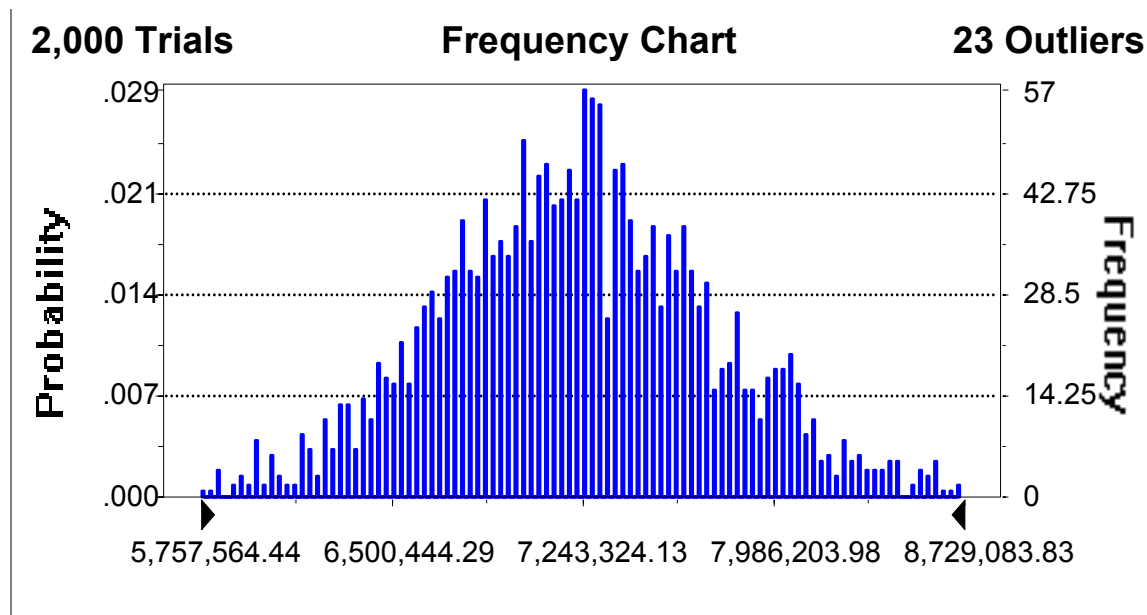


Figure 4-6. Profit distribution with base-load profile.

Obtaining a distribution of the total profit, as shown in Figure 4-6, makes it possible to evaluate the certainty of making the desired profit under an assumed electricity price uncertainty within a statistical framework. From another perspective, the same framework can be applied to see the statistical difference between the optimized profile and a base-load profile under fluctuating electricity prices.

To demonstrate robustness, however, it is necessary to demonstrate that the optimal load profiles implemented by the optimizer would bring statistically similar profit figures compared to optimal profiles obtained from a hypothetical situation where electricity prices were known with 100% certainty.

This robustness analysis is performed through simulations. Throughout the simulations, diminishing returns on the achieved robustness to changes in electricity prices are observed with respect to frequency of updates in the electricity forecasts. Although this decision about frequency of updates in the forecasts depends on the magnitude of the discrepancy of the forecasts and observed values, a realistic assumption of having accurate forecasts in the current

Final Report

week and deteriorating forecasts for the end of the horizon (as uncertainty dominates further into the future) is simulated here.

Table 4-1 summarizes the key results obtained through numerous simulations.

Table 4-1. Robustness Analysis Results

	Mean Profit	σ	Saved parts-life cost	Z (Electricity sales)	Z (Electricity sales+saved cost)
	\$	\$	\$		
Base-load	7,215,298	551,672	0		
Optimization with life equality constraint	1-)7,545,989	1-)558,882	0	0.6	0.6
	2-)7,534,095	2-)548,970	0	0.6	0.6
Optimization with life inequality constraint	1-)8,607,171	1-)523,251	1-)1,747,700	1-) 2.7	1-) 6
	2-)8,604,770	2-)539,142	2-)1,749,900	2-) 2.51	2-) 5.9

In Table 4-1, 1) denotes the total profit obtained through implementation of optimal profiles by updating the models at 6-hour decision intervals while updating the electricity price forecasts every week; 2) denotes the total profit that can be obtained if the unknown electricity prices were known and the optimizer uses that information to find the optimal solution. Rows of the table include the base-load profile profit, no optimization (as in Figure 4-5) and optimization with a life equality constraint (Formulation-3 in Appendix Section 4A.) and optimization with a life inequality constraint (Formulation-4 in Appendix Section 4A.).

As the data in Table 4-1 clearly indicates, results with optimization done every 6 hours with weekly updates in electricity price forecasts give statistically the same answer as the hypothetical case where the prices were known. The discrepancy between the total profit figures is very small and insignificant both statistically and economically. The load profiles obtained by simulations 1) and 2) in Table 4-1 are almost identical. These results demonstrate that robustness to uncertainty in electricity prices can be obtained by updating the forecasts with information that has more fidelity for the near future frequently and re-optimizing with updated models and information, as in the MPC paradigm.

Table 4-1 can also be used to observe the improvement of optimization with respect to base-load profile profit. Depending on the applied optimization constraint, optimization with life equality constraint (Formulation-3 in Appendix Section 4A) or optimization with life inequality constraint (Formulation-4 in Appendix Section 4A), different optimization improvements are obtained with respect to base-load operation. Since the numbers are totally dependent on the electricity prices, fuel prices, and maintenance cost figures used, a normalized improvement can be observed from Z values, where Z is defined as the normalized difference from the mean profit value with respect to standard deviation of total profit as in the following equation.

Final Report

$$Z \equiv \frac{x - \mu}{\sigma}$$

It should be noted that the observed improvement is greater for the optimization scheme with the life inequality constraint. However this improvement is totally dependent on the relative magnitudes of fuel cost and maintenance cost compared to electricity prices. For the data used in the simulations, fuel cost was considerably higher than electricity prices; thus operating the gas turbine at higher loads, which consumes more fuel, causes loss rather than profit. That is the reason the optimizer with a life inequality constraint (Formulation-4 in Appendix Section 4A) suggests less MWh production than the optimizer with a life inequality constraint that is acceptable within the applied minimum production constraints. Saved part life cost depends on the maintenance cost given to the optimizer. For this study a figure of \$2.5 M is used for the cost of gas turbine parts for a 1-year period. Different estimates can be used to see the effect of maintenance cost on gas turbine operation.

4.3.3 Computational Studies

Computational results are presented in Appendix Section 4B.

4.4 ANALYSIS

4.4.1 Optimization Formulations Applied to Combined Cycle Power Plant Operation

The optimization of profitability of a power generation facility that operates a single gas turbine can be extended to (1) optimization of multiple gas turbines running in simple cycle applications with a heat recovery steam generator and a steam turbine and (2) optimization of multiple gas turbines running in combined cycle applications with a heat recovery steam generator and a steam turbine. A combined cycle application of one gas turbine with a heat recovery steam generator and a steam turbine is depicted in Figure 4-8.

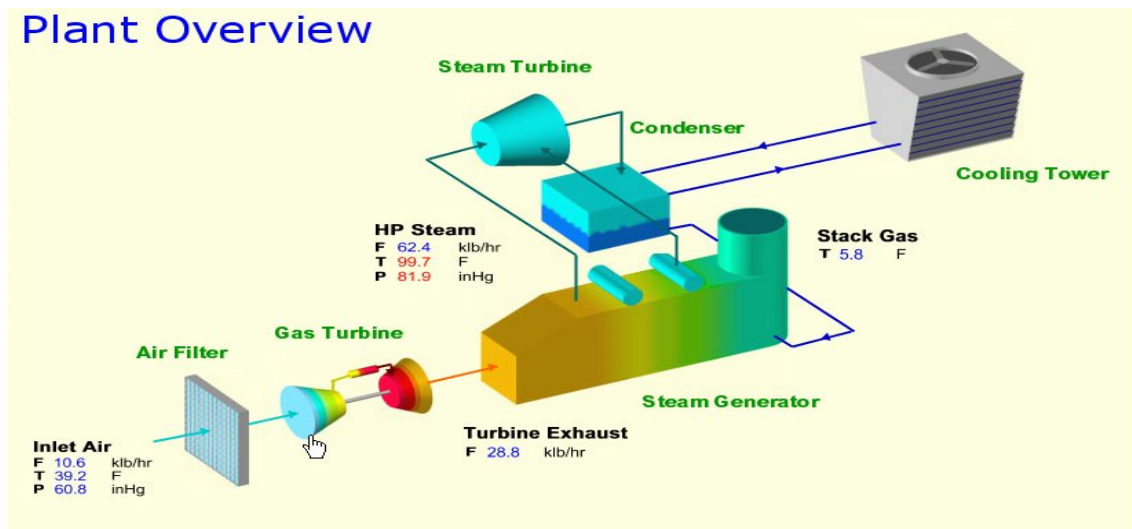


Figure 4-7. Overview of a Combined Cycle plant with one gas turbine, a steam turbine, and a heat recovery steam generator.

Final Report

For a preliminary study of the extension of the optimization formulations explained in Appendix Section 4A for applications with multiple gas turbines and steam turbine, a gas turbine cycle model and steam cycle model were used in combination to generate the performance information of a power generation facility running two gas turbines and a HRSG with a steam turbine. All information flow described in Section 4.3.1 remains the same for the extended problem. The formulations in Section 4.2 and in Appendix Section 4A also remain the same except for the following changes. The electricity production of the power facility is now the sum of two gas turbines and the steam turbine power production. The same concept applies to the fuel consumption and parts-life consumption for the two gas turbines. Steam turbine life and fuel cost are not taken into consideration because of their lower relative importance compared to the gas turbines.

4.4.1.1 Case Studies

The following case studies are analyzed for extending this optimization concept to the broad area of power generation modes. In power generation plants gas turbines can be operated in simple cycle mode or combined cycle mode with one underlying difference: In simple cycles, gas turbine firing temperature is manipulated for changing the MW output at a constant inlet guidance vane (IGV) angle between the load % of 60% to 100% (because of emission limits, gas turbines generally operate within 60% to 100% load in part-load) as shown in Figure 4-8.

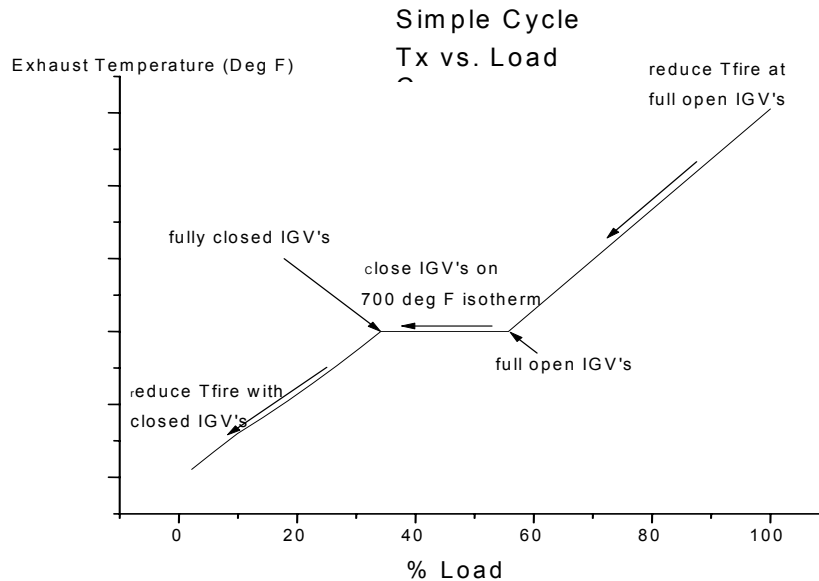


Figure 4-8. Simple Cycle operation principle

In combined cycle mode, however, IGVs are modulated in order to maintain the higher exhaust temperatures of gas turbines to supply as much heat as possible for the HRSG between 80% load and base-load (100 % load). For load levels less than 80%, the firing temperature is manipulated as shown in Figure 4-9.

Final Report

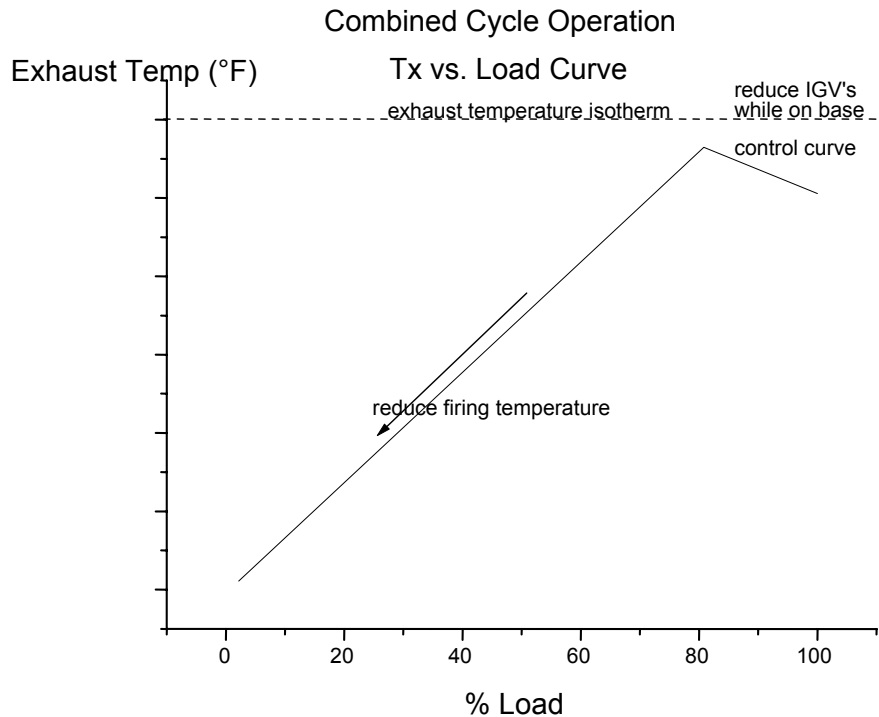


Figure 4-9. Combined Cycle operation principle

Optimization case studies on each of these operating modes are described in Appendix Section 4C.

4.5 CONCLUSIONS

The objective of the Smart Power Turbine Supervisory Control and Optimizer task was to investigate the feasibility of an advanced robust optimization and control application that met the following criteria:

- Suitability for closed-loop optimization
- Ability to find the optimal trade off between gas turbine maintenance and electricity production costs
- Ability to perform optimization using a robust algorithm

These criteria were met with the proposed formulations and simulation studies tested on a Pentium III 833 MHz desktop. The proposed algorithm decides on the optimal firing temperature that sets the optimal load profile for a selected future horizon.

This advanced controls and optimization formulation incorporates the existing sensor information as well as information from the new sensors. They are used to continuously update the models for matching model predictions with current power plant output

Once the new sensor designs are completed and corresponding models for diagnostic purposes are established, they can be easily incorporated with the proposed concept for Condition Based Maintenance.

Final Report

Although the focus here is on a single gas turbine operation with firing temperature as the key variable, other variables such as steam augmentation and inlet chilling can be incorporated into the same framework. Preliminary analysis of the applicability of these ideas to combined cycle applications indicates that while a simple extension of the algorithms is possible for multiple gas turbines operating in simple cycle mode or combined cycle mode, other variables such as inlet chilling or steam augmentation would necessitate mixed integer programming techniques to be incorporated with existing algorithms. Yet because of the scope of this project, the extension of the algorithms to mixed integer programming was not considered.

4.6 REFERENCES

Clelow, L., and C. Strickland, *Energy Derivatives Pricing and Risk Management*. London, England: Lacima Publications, 2000.

Cutler, C., and B.L. Ramaker, "Dynamic Matrix Control - A computer control algorithm," Paper No 51B, presented at the AIChE National Meeting, Houston, TX, 1997.

Hoefl, R., J. Janowitz, and R. Keck, "Heavy-duty gas turbine operating and maintenance considerations," GER-3620J, GE Energy Services, Atlanta, GA, 2003.

Lee, E. B., and L. Marcus, *Foundations of Optimal Control Theory*. New York: John Wiley & Sons, 1967.

Prett, D. M., and R.D. Gillette, "Optimization and constrained multivariable control of a catalytic cracking unit," *Proceedings of Joint Automatic Control Conference*, WP5-c, 1980.

Propoi, A.I., "Use of linear programming methods for synthesizing sampled-data automatic systems," Autumn 1963, *Remote Control*, vol. 24, no. 7, pp. 837-844.

Qin, S.J, and T.A. Badgwell, "An overview of industrial model predictive control technology," Fifth Int. Conf. on Chem. Process Control, AIChE Symp. Series, 1997, vol. 316, no. 93, pp. 232ff.

Richalet, J., A. Rault, and J.L.I. Testud, "Applications to industrial processes," *Automatica*, 1978, vol. 14, pp. 413-428.

Final Report

GENERAL CONCLUSIONS AND FUTURE PLANS

All of the Smart Power Turbine Program tasks—Flame Temperature Sensor (FTS), Coating Life Odometer, Fuel Quality Sensor, and Supervisory Control/Optimizer (Adaptive Control System)—have completed laboratory testing prior to field-testing in a gas turbine. Because these technologies are all at different levels of maturity, they are also at different stages of readiness for field-testing. Prior to initiation of field testing in a GE gas turbine, the technology must be approved by the GE Power Systems Chief Engineer’s Office and permission must be granted by the power plant customer. GE Power Systems has programs in place that will enable us to perform the required tests for each of the Smart Power Turbine sensors.

The Supervisory Control/Optimizer task addresses the problem of optimally running a gas turbine to maximize the operational performance (profit generated) for a power utility faced with fluctuating energy prices and changing operating conditions. Adjusting the firing temperature of a gas turbine varies its power output and fuel consumption. The firing temperature also affects the extent of wear and tear on the turbine parts, thereby dictating the length of maintenance intervals. Preliminary models were acquired and assembled onto a common platform in a modular fashion. Since the optimizer provides an optimum operating set point (firing temperature profile throughout the horizon, months, years, etc.), the team used electricity forecasts to investigate the robustness of the algorithm to uncertainties in electricity prices and tested the algorithm with simulations. The algorithm has been incorporated into a proprietary software application used by GE Energy Services. At present this algorithm does not require new sensor inputs; input from a number of sensors, including the Flame Temperature Sensor (FTS), Coating Life Odometer, and Fuel Quality Sensor, will be incorporated into the algorithm after field validation has been completed and as desired by GE Energy Services.

The Flame Temperature Sensor uses the optical emission intensity of the flame as an indication of flame temperature. Although optical emission of the flame is not a direct measurement of flame temperature, it has been used to derive a relationship between emission intensity and temperature. Tests conducted in a single gas turbine nozzle combustor at atmospheric conditions have shown conclusively that the relationship derived from optical intensity in a pre-mixed gas turbine flame is linearly dependent on average flame temperature. Sensor acceptance tests are being conducted on a full-scale heavy-duty gas turbine combustor at GE Power Systems. Field testing in a gas turbine will be performed once all acceptance criteria have been met.

Technical feasibility has been demonstrated for producing a “smart” thermal barrier coating (TBC) that indicates its service condition during turbine operation. The smart TBC was chemically “tagged” by doping the coating with small amounts of a rare earth element. The taggant was an element not commonly found in materials used in the construction of gas turbines, and it was an element that caused the TBC to fluoresce under illumination with ultraviolet light. Those two properties allow two levels of coating health monitoring:

- Exhaust spall detection: The presence of the taggant material in the turbine exhaust enables on-line detection of a coating spall during turbine operation.
- Fluorescent spall location: The enhanced contrast of the fluorescent TBC produces high definition of spall locations on turbine components during in-situ inspection without part removal.

Final Report

The smart thermal barrier coating will be tested in a heavy-duty gas turbine containing a partial set of coated buckets in what is sometimes referred to as a “rainbow” test. The buckets are being prepared by GE Power Systems this year, and will be installed in a gas turbine in 2004.

The Fuel Quality Sensor is being developed under a sub-contract with Sandia National Laboratory. Preliminary tests were completed, which showed the capability to measure the lower heating value of fuel using the Micro-Electro-Mechanical Systems (MEMS) based micro-calorimeter concept at Sandia. A working prototype was transferred and tested at the GE Global Research Center. An advanced version of this prototype will be tested on a gas-fired reciprocating engine in late 2003, and possibly on a small integrated gasification combined cycle (IGCC) gas turbine at the DOE Power System Development Facility operated by Southern Company. Testing on a heavy-duty IGCC gas turbine will occur in 2005.

Final Report

ACKNOWLEDGMENTS

This project and report is a joint effort of staff members at GE Global Research Center and Sandia National Laboratory. Contributions from the following are acknowledged.

Flame Temperature Sensor: P. M. Sandvik, D. M. Brown, J. B. Fedison, J. R. Hibshman, W. Kretchmer, L. Lombardo, and K. S. Matocha.

Fuel Quality Sensor System: R P. Manginell and M.W. Moorman

Coating Life Odometer: J.A. Ruud, A. Srivastava, and Y. Gao.

Adaptive Control System: S. Alper Eker

Final Report

ACRONYMS AND ABBREVIATIONS

ANOVA	analysis of variance	ICP-MS	inductively-coupled-plasma mass spectrometry
ANSYS	a finite element modeling software package	IGBT	insulated gate bipolar transistor
APS	air plasma spray	IGCC	integrated gasification combined cycle
ASTM	American Society for Testing and Materials	IGV	inlet guidance vane
CBM	condition-based maintenance	JETS	Jet engine thermal simulation
CCD	charge coupled device	LHV	lower heating value
COBRA	laser profilometer	LoF	limits of flammability
CVR	current viewing resistor	MEMS	micro-electro-mechanical system
DFSS	design for six sigma	MFC	mass flow controller
DIPs	dual inline packages	MOSFET	metal oxide semiconductor field effect transistor
DLN	dry low NO _x	MPC	Model Predictive Control
DVC	dense-vertically-cracked	MTL	Mass-transfer limited
FCT	furnace cycle test	MUX	multiplexer
FD	flame detector	NETL	National Energy Technology Laboratory
FFT	fast fourier transfer	NG	natural gas
FOD	foreign-object damage	NPN	negative-positive-negative
FTS	flame temperature sensor	PD	photodiode
FTS	first generation flame temperature sensor device	RRL	reaction-rate limited
GC	gas chromatograph	ST	steam turbine
GEAE	GE Aircraft Engine	TBC	thermal barrier coating
GEGRC	GE Global Research Center	TCD	thermal conductivity detector
GT	gas turbine	TCR	temperature coefficient of resistance
HRSG	heat recovery steam generator	TEC	Thermo Electron Corporation